

# From microscopics to hydrodynamics

A Thesis

Submitted to the

Tata Institute of Fundamental Research, Mumbai

Subject Board of Physics

for the degree of Doctor of Philosophy

by

Sahil Kumar Singh

International Centre for Theoretical Sciences

Tata Institute of Fundamental Research

Bengaluru, India-560089

April, 2025

[Final Version Submitted in September, 2025]

# DECLARATION

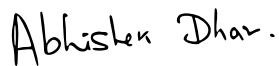
This thesis is a presentation of my original research work. Wherever contributions of others are involved, every effort is made to indicate this clearly, with due reference to the literature, and acknowledgment of collaborative research and discussions.

The work was done under the guidance of Professor Abhishek Dhar, at the International Centre for Theoretical Sciences, Tata Institute of Fundamental Research (ICTS-TIFR), Bengaluru.



Sahil Kumar Singh

In my capacity as supervisor of the candidate's thesis, I certify that the above statements are true to the best of my knowledge.



Professor Abhishek Dhar

Date: *September 3, 2025*

# Preface

This thesis is based on publications [1] and [2]. The background in Chapter 1 is a review of the standard procedure of going from classical Hamiltonian dynamics to hydrodynamics via the Boltzmann transport equation.

Chapter 2 is a slightly rewritten version of [1], written by the author in collaboration with Subhadip Chakraborti, Abhishek Dhar and P. L. Krapivsky.

Chapter 3 is a slightly rewritten version of [2], written by the author in collaboration with Abhishek Dhar, Herbert Spohn and Anupam Kundu.

# List of Publications

## Thesis Publications

1. Sahil Kumar Singh, Subhadip Chakraborti, Abhishek Dhar, and P. L. Krapivsky. Blast waves in the zero temperature hard sphere gas: Double scaling structure. *Journal of Statistical Physics*, 190(7):118, Jul 2023.
2. Sahil Kumar Singh, Abhishek Dhar, Herbert Spohn, and Anupam Kundu. Thermalization and hydrodynamics in an interacting integrable system: The case of hard rods. *Journal of Statistical Physics*, 191(6):66, May 2024.

# Abstract

*"To understand the world, one must not be limited to what is seen but seek to reveal the hidden."*

– Aristotle

The macroscopic properties of many-particle systems are usually governed by phenomenological laws, such as thermodynamics and hydrodynamics, which differ notably from their underlying microscopic dynamics. These macroscopic laws are usually not rigorously derived from first principles. In this thesis, we investigate whether predictions from these phenomenological laws can be validated through microscopic simulations in both non-integrable and integrable systems.

The thesis consists of two parts. The first part [1] focuses on non-integrable systems, specifically examining a hard-sphere gas in one and two dimensions. In one dimension, the system is composed of alternating-mass hard rods, while in two dimensions, it is a hard-disc gas. We compare the predictions of molecular dynamics with those of hydrodynamics for a blast wave initial condition (in which a shock or discontinuity forms). We thus test hydrodynamic predictions under conditions that challenge its assumptions of slow field variation. Our findings reveal two distinct regions: one where dissipation plays a major role and another dominated by Euler terms. Each region exhibits unique space-time scaling behaviors in the hydrodynamic fields, which we explain using dimensional analysis. We also show that these two different scaling regions are connected by the rules of asymptotic matching.

The second part [2] explores an interacting integrable system: an equal-mass hard-rod gas in one dimension. Because it is an interacting system, its hydrodynamic equations exhibit non-zero dissipation, which tends to drive the system toward a Generalized Gibbs Ensemble (GGE). Interestingly, we identify certain initial conditions that do not go to GGE, while other conditions do. For both cases, we find good agreement between hydrodynamic predictions and molecular dynamics simulations, demonstrating the applicability of hydrodynamic theory in these integrable settings.

# Acknowledgments

I am deeply grateful to my supervisor, Prof. Abhishek Dhar, for his unwavering guidance and support throughout my PhD journey. It has been an invaluable learning experience working with him, not only in terms of scientific insights but also in understanding the art of research.

In addition, I am deeply grateful to my collaborators, Subhadip Chakraborti, Paul Krapivsky, Herbert Spohn, and Anupam Kundu, with whom I worked during my PhD. I thank Jitendra Kethepalli, Isaac Perez Castillo, Massimiliano Esposito, Benjamin Doyon, and Herbert Spohn for various useful discussions that helped me gain deeper insights into statistical physics. Discussions with Santhosh Ganapa helped me understand the art of solving partial differential equations on a computer. I would also like to thank ICTS, ICTP, Yukawa Institute for Theoretical physics and ENS de Lyon for organizing great schools and workshops and for funding my visits.

I would also like to thank Amit Dutta, whose classes on the renormalization group in statistical physics during my final year at IIT Kanpur were intellectually very rewarding.

I thank Sriram Ramaswamy for asking important and insightful questions during my thesis committee meetings.

I would also like to thank Ankush Chaubey, Harshit Joshi, Sparsh Gupta, and others from NCBS and inStem for keeping me physically active by encouraging me to play badminton.

Finally, I would like to thank the unique environment of ICTS and the very helpful staff of the Academic Office and the Establishment, which made it easy for me to deal with administrative matters.

# Contents

<b>Preface</b>	<b>2</b>
<b>List of Publications</b>	<b>3</b>
<b>Contents</b>	<b>6</b>
<b>1 Introduction</b>	<b>10</b>
1.1 Background . . . . .	11
1.1.1 From Hamiltonian to Boltzmann . . . . .	12
1.1.2 From Boltzmann to hydrodynamics . . . . .	13
1.1.3 Integrable systems . . . . .	14
<b>2 Blast waves in a hard sphere gas</b>	<b>18</b>
2.1 Models, observables and initial conditions . . . . .	20
2.2 Results . . . . .	22
2.3 Blast in the 2D hard-disc gas . . . . .	22
2.3.1 TvNS solution . . . . .	23
2.3.2 Effect of dissipation on scaling in the blast core . . . . .	25
2.3.3 Numerical results . . . . .	28
2.4 Blast in 2D ideal gas . . . . .	33

2.4.1	TvNS solution	35
2.4.2	Core scaling solution	36
2.4.3	Numerical results	36
2.5	Blast in the hard-rod gas	37
2.5.1	TvNS solution	38
2.5.2	Core scaling solution	39
2.5.3	Numerical results	41
2.6	Hard point gas in $d$ -dimensions: Inner and outer solutions	42
2.6.1	Outer solution	42
2.6.2	Inner solution	46
2.7	Discussion	48
<b>3</b>	<b>Interacting Integrable system</b>	<b>50</b>
3.1	Model, observables and initial conditions	52
3.2	Results	54
3.3	Hydrodynamic equations for hard rods and solution of the Euler equation	55
3.4	Results from numerical simulations for the three initial conditions	57
3.4.1	Initial condition A	57
3.4.2	Initial condition B	64
3.4.3	Euler vs MD for initial condition C	67
3.5	Conclusion	70
<b>4</b>	<b>Summary and outlook</b>	<b>73</b>
4.1	Synthesis of Key Findings	73
4.1.1	Insights from Non-integrable Systems	73



4.1.2	Insights from Integrable Systems	74
4.2	Connecting Hydrodynamics with the Renormalization Group and Effective	
	Field Theory	75
4.2.1	Effective Field Theory (EFT) and Multiscale Coupling	76
4.3	Limitations	76
A	$\sqrt{t}$ Behaviour of the Shock for Initial Condition (A)	77
	Bibliography	79

*"We have to remember that what we observe is not nature itself, but nature exposed to our method of questioning."*

– **Werner Heisenberg**

# Chapter 1

## Introduction

*"The more one approaches the truth, the more one finds that it is universal."*

**-Nikola Tesla**

When describing the large-scale behavior of many-particle systems, microscopic details usually become irrelevant, and universal laws depending only on the symmetries emerge. Thermodynamics is one such example of a universal theory. Considering that most of the phenomena around us involve many-particle systems, one would think that only macroscopic theories are relevant and useful. However, in many cases, there is a huge time scale after which these macroscopic theories start to become valid, and the behavior of the system during this time scale depends on the microscopic details. For example, while thermodynamics predicts that entropy always increases with time, if one looks at the plot of entropy vs time on a very short time scale, one would observe fluctuations in the entropy curve if the system is finite. These fluctuations are of great importance in fields such as quantum computation and biology, as they enable the harnessing of quantum mechanics' power in the former and the emergence of life in the latter. Another example is that we as life forms rely on microscopic processes to stay alive and not reach equilibrium. Thus, the physics at the intermediate scales is very important to study.

Thermodynamics tells us that all systems tend to a maximum entropy state on large time scales, and this maximum entropy state is the equilibrium state, which is well described by the rules of statistical mechanics. However, there is no general theory like statistical mechanics for physics at the intermediate time scale, i.e., when the system is in a non-equilibrium state. Hydrodynamics is one of the attempts to describe the physics near local equilibrium. To first order, it assumes local equilibrium to get the Euler equation, and to the next order, it treats deviations from local equilibrium in a first-order approximation to get the Navier-Stokes equation. However, in some cases, the

deviations from local equilibrium can be large, e.g., when shocks are formed, and we have verified the prediction of hydrodynamics with simulations of Newtonian dynamics for this case in [1].

Since equilibrium thermodynamics is a universal theory to some extent, it is expected that near equilibrium theories like hydrodynamics are also universal, with the microscopic details entering only in a few quantities, like the transport coefficients and the equation of state. Integrable systems are expected to have a different structure of hydrodynamics from non-integrable ones, since they have more conservation laws and symmetries. Moreover, they also serve as minimal models to formulate theories for non-integrable systems; e.g., Landau's theory of Fermi liquid was inspired by studying non-interacting electrons. Thus, it is important to study dynamics of integrable systems from the point of view of classifying universality classes of many-body phenomena and also to understand phenomena in other non-integrable systems. We studied integrable models in [2], where we compared predictions of Newtonian dynamics with those of hydrodynamics, and we found good agreement. Moreover, we found certain classes of initial conditions which do not reach the Generalised Gibbs Ensemble (GGE).

## 1.1 Background

This thesis is concerned with classical Hamiltonian many-particle systems in  $d$ -dimensions:

$$H = \sum_{i=1}^N \frac{p_i^2}{2m} + \sum_{i<j} V(|\mathbf{r}_i - \mathbf{r}_j|). \quad (1.1)$$

We set  $m = 1$ , thus the velocity of each particle  $\mathbf{u}_i$  equals the momentum  $\mathbf{p}_i$ . For a generic form of the interaction potential  $V(r)$ , the equations of motion are usually intractable to solve for macroscopic values of  $N$ . Because one cannot track the time evolution of the system in phase space, one talks about the time evolution of the probability distribution of points in phase space  $\varrho(\mathbf{r}_1, \mathbf{p}_1, \mathbf{r}_2, \mathbf{p}_2, \dots, \mathbf{r}_N, \mathbf{p}_N, t)$  through the Liouville equation:

$$\frac{\partial \varrho}{\partial t} = \{H, \varrho\} = \sum_{i=1}^N \left( \frac{\partial H}{\partial \mathbf{r}_i} \cdot \frac{\partial \varrho}{\partial \mathbf{p}_i} - \frac{\partial H}{\partial \mathbf{p}_i} \cdot \frac{\partial \varrho}{\partial \mathbf{r}_i} \right), \quad (1.2)$$

where  $\{, \}$  is the Poisson bracket and  $\cdot$  is the dot product. Another reason to deal with probability distributions is because when one is talking about coarse-grained macroscopic

properties, the exact microscopic initial condition is irrelevant because of the apparent equivalence between coarse-graining and ensemble averaging. In other words, the Liouville equation acts as a bridge between the microscopic scale and the macroscopic scale.

Upon using the form of Hamiltonian (Eq. [1.1](#)) in the Liouville equation (Eq. [1.2](#)), we have:

$$\frac{\partial \varrho}{\partial t} = \sum_{i=1}^N \left( \frac{\partial \varrho}{\partial \mathbf{p}_i} \cdot \sum_{j,j \neq i} \frac{\partial V_{ij}}{\partial \mathbf{r}_i} - \mathbf{u}_i \cdot \frac{\partial \varrho}{\partial \mathbf{r}_i} \right), \quad (1.3)$$

where  $V_{ij} = V(|\mathbf{r}_i - \mathbf{r}_j|)$ .

### 1.1.1 From Hamiltonian to Boltzmann

We introduce a shorthand notation  $\tau_i = (\mathbf{r}_i, \mathbf{p}_i)$  and integrate Eq. [1.3](#) over  $d\tau_2 d\tau_3 \dots d\tau_N$  and assuming that  $\varrho$  vanishes when either  $\mathbf{r}_i$  or  $\mathbf{p}_i$  are on the infinite surface in  $\mathbf{r}$ - or  $\mathbf{p}$ -space respectively, we have:

$$\frac{\partial f^{(1)}(\tau_1, t)}{\partial t} + \mathbf{u}_1 \cdot \frac{\partial f^{(1)}(\tau_1, t)}{\partial \mathbf{r}_1} = N \int \frac{\partial V_{12}}{\partial \mathbf{r}_1} \cdot \frac{\partial f^{(2)}(\tau_1, \tau_2, t)}{\partial \mathbf{p}_1} d\tau_2, \quad (1.4)$$

where  $f^{(1)}$  and  $f^{(2)}$  are respectively the one- and two-particle distribution functions:

$$f^{(1)}(\tau_1, t) = \int \varrho(\tau_1, \tau_2, \dots, \tau_N, t) d\tau_2 d\tau_3 \dots d\tau_N, \quad (1.5a)$$

$$f^{(2)}(\tau_1, \tau_2, t) = \int \varrho(\tau_1, \tau_2, \dots, \tau_N, t) d\tau_3 d\tau_4 \dots d\tau_N. \quad (1.5b)$$

Similarly, the equation of the two-particle distribution  $f^{(2)}(\tau_1, \tau_2, t)$  obtained from Eq. [1.3](#) is:

$$\frac{df^{(2)}(\tau_1, \tau_2, t)}{dt} = N \int \left( \frac{\partial f^{(3)}}{\partial \mathbf{p}_1} \cdot \frac{\partial V_{13}}{\partial \mathbf{r}_1} + \frac{\partial f^{(3)}}{\partial \mathbf{p}_2} \cdot \frac{\partial V_{23}}{\partial \mathbf{r}_2} \right) d\tau_3, \quad (1.6)$$

where  $\frac{df^{(2)}}{dt}$  is the total derivative in which  $\tau_1 = (\mathbf{r}_1, \mathbf{p}_1)$  and  $\tau_2 = (\mathbf{r}_2, \mathbf{p}_2)$  are treated as functions of time satisfying equations of motion corresponding to the two-particle Hamiltonian:

$$H = \frac{p_1^2}{2} + \frac{p_2^2}{2} + V(|\mathbf{r}_1 - \mathbf{r}_2|), \quad (1.7)$$

and  $f^{(3)}$  is the three-particle distribution function. Proceeding in this way gives us a series of equations relating  $f^{(n)}$  to  $f^{(n+1)}$ . This is the so-called BBGKY (Bogoliubov–Born–Green–Kirkwood–Yvon) hierarchy.

In the dilute limit, where the interparticle separation is much larger than the size

of the particles, the terms on the right side of Eq. [1.6](#) are negligible compared to those on left side, giving us  $\frac{df^{(2)}(\tau_1, \tau_2, t)}{dt} = 0$  [\[3\]](#), which breaks the BBGKY hierarchy. To solve  $\frac{df^{(2)}}{dt} = 0$ , a further assumption is needed, which is the statistical independence of two colliding particles, which is also called the molecular chaos assumption. If  $t_0$  is some instant much before the collision, then the molecular chaos assumption together with the total time derivative being zero gives us:

$$f^{(2)}(\tau_1, \tau_2, t) = f^{(1)}(\tau_{10}, t_0) f^{(1)}(\tau_{20}, t_0). \quad (1.8)$$

$\tau_{10}, \tau_{20}, t_0$  can be related to  $\tau_1, \tau_2, t$  by solving the two body collision problem [\[3\]](#) giving us the Boltzmann equation:

$$\frac{\partial f^{(1)}(\mathbf{r}, \mathbf{p}, t)}{\partial t} + \mathbf{u} \cdot \frac{\partial f^{(1)}(\mathbf{r}, \mathbf{p}, t)}{\partial \mathbf{r}} = C(f^{(1)}), \quad (1.9)$$

where  $C(f)$  is the collision integral:

$$C(f^{(1)}) = \int (f^{(1)}(\mathbf{r}, \mathbf{p}'', t) f(\mathbf{r}, \mathbf{p}''', t) - f^{(1)}(\mathbf{r}, \mathbf{p}, t) f(\mathbf{r}, \mathbf{p}', t)) |\mathbf{u} - \mathbf{u}'| d\sigma d^d p', \quad (1.10)$$

where  $d\sigma$  is the collision cross section and  $\mathbf{p}''$  and  $\mathbf{p}'''$  are determined from the conservation of momentum and energy of two colliding particles with momenta  $\mathbf{p}$  and  $\mathbf{p}'$ .

### 1.1.2 From Boltzmann to hydrodynamics

The hydrodynamic assumption is that the densities of the conserved quantities, which are the relevant fields, are slowly varying compared to the mean free path of collision and thus local equilibrium is achieved to zeroth order in a perturbation theory:

$$f^{(1)}(\mathbf{r}, \mathbf{p}, t) = \frac{\rho(\mathbf{r}, t)}{(2\pi T(\mathbf{r}, t))^{d/2}} \times e^{-\frac{|\mathbf{p} - \mathbf{v}(\mathbf{r}, t)|^2}{2T(\mathbf{r}, t)}} + \text{corrections giving rise to dissipative terms}, \quad (1.11)$$

where  $T(\mathbf{r}, t)$  is the temperature field,  $\mathbf{v}(\mathbf{r}, t)$  is the local velocity field,  $\rho(\mathbf{r}, t)$  is the mass density, and the Boltzmann constant is set to unity. We neglect the corrections which will give rise to the dissipative terms. For a full treatment of these corrections, the reader is referred to [\[3\]](#). Plugging the ansatz Eq. [1.11](#) in the collision integral  $C(f^{(1)})$  gives us  $C(f^{(1)}) = 0$ , as collisions do not alter the local equilibrium form. Thus we have the equation:

$$\partial_t f^{(1)}(\mathbf{r}, \mathbf{p}, t) + \partial_i (u_i f^{(1)}(\mathbf{r}, \mathbf{p}, t)) = 0, \quad (1.12)$$

where  $\partial_i$  denotes partial derivative with respect to  $i$ th component of  $\mathbf{r}$  and  $u_i$  is the  $i$ th component of  $\mathbf{u}$ . After multiplying this equation by 1,  $p_j$  or  $p^2/2$ , integrating over  $\mathbf{p}$

and using the local equilibrium form of  $f^{(1)}$ , we get respectively the following three Euler equations:

$$\partial_t \rho + \partial_i(\rho v_i) = 0, \quad (1.13a)$$

$$\partial_t(\rho v_i) + \partial_j(\rho v_i v_j) + \partial_i P = 0, \quad (1.13b)$$

$$\partial_t(\rho e) + \partial_i(\rho e v_i) + \partial_i(P v_i) = 0, \quad (1.13c)$$

where

$$\rho(\mathbf{r}, t) = \int f^{(1)}(\mathbf{r}, \mathbf{p}, t) d^d p, \quad (1.14a)$$

$$\rho(\mathbf{r}, t) \mathbf{v}(\mathbf{r}, t) = \int \mathbf{p} f^{(1)}(\mathbf{r}, \mathbf{p}, t) d^d p, \quad (1.14b)$$

$$e(\mathbf{r}, t) = \int \frac{p^2}{2} f^{(1)}(\mathbf{r}, \mathbf{p}, t) d^d p, \quad (1.14c)$$

and  $P(\mathbf{r}, t) = \rho(\mathbf{r}, t)T(\mathbf{r}, t)$  is the equation of state relating pressure field with the density- and temperature field,  $e$  is the energy per unit mass,  $e = v^2/2 + dT/2$ .

### 1.1.3 Integrable systems

In going from microscopics to hydrodynamics in the previous sections, a key assumption was the molecular chaos assumption. However, for one-dimensional integrable systems, this assumption is no longer valid because the many-particle scattering is factorized into two particle scattering [4], and when two equal mass particles collide in one-dimension, they exchange their asymptotic velocities and the particles thus have "memory" of previous collisions. A completely different method is needed to derive the hydrodynamics for these integrable systems. One of the first steps was taken by Percus and others [5, 6] for the particular case of equal mass hard rods in one-dimension in which they derived the hydrodynamics exactly from the microscopic dynamics without any phenomenological assumption such as the molecular chaos hypothesis, and later the derivation was made mathematically rigorous in [7, 8]. Later, a general form of hydrodynamics was written down for generic one-dimensional classical and quantum integrable systems using phenomenological arguments (such as the assumption that the system reaches local GGE). [9, 10].

In this thesis, we concern ourselves only with one-dimensional hard rods, and thus review here Percus's derivation of their hydrodynamics. The first step is the realization that the hard rod dynamics can be mapped to the point particle dynamics via the

following transformation:

$$x'_i = x_i - (i - 1/2)a, \quad v'_i = v_i \quad i = 1, 2, \dots, N, \quad (1.15)$$

where  $x_i, v_i$  are the position and velocity of the  $i$ th hard rod, and the  $x'_i, v'_i$  are the position and velocity of the  $i$ th point particle. One can verify that the hard rod constraint  $x_{i+1} - x_i \geq a$  transforms into the point particle constraint  $x'_{i+1} - x'_i \geq 0$ , thus this indeed maps the hard rod problem to the point particle problem.

Since the particles just exchange their velocities upon collision, the density of conserved quantity is nothing but the single particle phase space distribution  $f(x, v, t)$ , and thus the hydrodynamics is a partial differential equation involving it. If we exchange the labels of the two colliding particles after collision, and do this for every collision, then the new labels describe what are called quasiparticles, and they move at fixed velocities. The single particle phase space distribution  $f(x, v, t)$  is nothing but the density of quasiparticles with velocity  $v$ . From now onwards, we denote the  $x_i, v_i$  as position and velocities of the hard-rod quasiparticles and  $X_i, V_i$  as the quasiparticles in the mapped point particle problem. Then the single particle phase space distribution is given by:

$$f(x, v, t) = \sum_i \langle \delta(x - x_i) \delta(v - v_i) \rangle, \quad (1.16)$$

where  $\langle \dots \rangle$  denotes average over the many-particle phase space distribution. We look at the Fourier transform of  $f(x, v, t)$  with respect to  $x$ , i.e.,  $f_k(v, t)$  given by:

$$f_k(v, t) = \sum_l \langle e^{ikx_l} \delta(v - v_l) \rangle \quad (1.17)$$

The hard rod variables  $\{x_l, v_l\}$  can be written in terms of point particle variables  $\{X_l, V_l\}$  given by:

$$x_l = X_l + a \sum_{j \neq l} \Theta(X_l - X_j) \quad (1.18a)$$

$$v_l = V_l \quad (1.18b)$$

It is clear that the doublets  $\{X_l, V_l\}$  are independent and identically distributed doublets if the distribution of these variables at  $t = 0$  is independent and identically distributed,



because the point particle gas is effectively a non-interacting gas. Thus

$$f_k(v, t) = \sum_l \langle e^{ikX_l} e^{iak \sum_{j \neq l} \Theta(X_l - X_j)} \delta(v - V_l) \rangle \quad (1.19a)$$

$$= \int dz \sum_l \langle e^{ikz} e^{iak \sum_{j \neq l} \Theta(z - X_j)} \delta(z - X_l) \delta(v - V_l) \rangle \quad (1.19b)$$

$$= \int dz e^{ikz} \langle e^{iak \Theta(z - X_j)} \rangle_{X_j}^{N-1} \left\langle \sum_l \delta(z - X_l) \delta(v - V_l) \right\rangle_{X_l, V_l} \quad (1.19c)$$

$$= \int dz e^{ikz} \langle 1 + (e^{ika} - 1) \Theta(z - X_j) \rangle_{X_j}^{N-1} \left\langle \sum_l \delta(z - X_l) \delta(v - V_l) \right\rangle_{X_l, V_l} \quad (1.19d)$$

$$= \int dz e^{ikz} \left( 1 + (e^{ika} - 1) \frac{F^0(z, t)}{N} \right)^{N-1} f^0(z, v, t), \quad (1.19e)$$

where  $\langle \cdots \rangle_{X_j}$  denotes average with respect to the probability distribution of  $X_j$ ,  $\langle \cdots \rangle_{X_l, V_l}$  denotes average with respect to the joint probability distribution of  $\{X_l, V_l\}$ , and we have used that the phase space coordinates of the point particles  $\{X_l, V_l\}$  are independent doublets,  $F^0(z, t)$  is the cumulative density of point particles ( $F^0(z, t) = N \langle \Theta(z - X_j) \rangle_{X_j}$ ) and we have denoted the point particle phase space distribution by  $f^0(z, v, t)$ . In the  $N \rightarrow \infty$  limit, this gives us

$$f_k(v, t) = \int dz e^{ikz} e^{(e^{ika} - 1) F^0(z, t)} f^0(z, v, t) \quad (1.20)$$

If we assume hydrodynamic limit, i.e., only small  $k$  modes of  $f_k(v, t)$  are dominant, then we can write  $e^{(e^{ika} - 1) F^0(z, t)} \approx e^{ika F^0(z, t)}$ , where we have expanded  $e^{ika} - 1$  to first non-zero order. This will give us, upon inverse Fourier transforming  $f_k(v, t)$  in Eq. [1.20](#), a relation between  $f(x, v, t)$  and  $f^0(x', v, t)$  in the hydrodynamic limit:

$$f(x, v, t) = \frac{f^0(x', v, t)}{1 + a \rho^0(x', t)}, \quad (1.21)$$

where  $x = x' + a F^0(x', t)$ ,  $\rho^0(x', t) = \int f^0(x', v, t) dv$ . For the point particle gas, we know that  $\partial_t f^0(x', v, t) + \partial_{x'} f^0(x', v, t) = 0$ , which gives us, using Eq. [1.21](#), the hydrodynamics of the hard-rod gas:

$$\partial_t f(x, v, t) + \partial_x (v_{\text{eff}}(x, v, t) f(x, v, t)) = 0, \quad (1.22)$$

where

$$v_{\text{eff}}(x, v, t) = \frac{v - a \rho(x, t) u(x, t)}{1 - a \rho(x, t)}, \quad (1.23)$$

and

$$\rho(x, t) = \int f(x, v, t) dv, \quad (1.24a)$$

$$u(x, t) = \frac{1}{\rho} \int v f(x, v, t) dv. \quad (1.24b)$$

# Chapter 2

## Blast waves in a hard sphere gas

*"Nature uses only the longest threads to weave her patterns, so that each small piece of her fabric reveals the organization of the entire tapestry."*

**-Richard Feynman**

The non-equilibrium state of a fluid is usually described by hydrodynamics. However, on a microscopic level, the individual particles follow Newton's laws of motion. How does hydrodynamics emerge from microscopic Newtonian dynamics? A rigorous derivation of hydrodynamics starting from microscopic Newtonian dynamics is lacking. Phenomenological textbook derivations involve applying conservation of mass, momentum and energy to a parcel of fluid, and there are also derivations based on the Boltzmann equation [3]. The latter assume that the hydrodynamic limit is achieved. More precisely, the spatial variations of the coarse-grained variables are sufficiently slow, i.e., local equilibrium is achieved, and the deviations from local equilibrium are small. Thus to zeroth order, one assumes local equilibrium and gets the Euler equations which do not have dissipation. To next order, one includes deviations from local equilibrium to get Navier-Stokes equations which include dissipation as higher order derivative corrections to the Euler equations.

In some cases the hydrodynamic limit may not be achieved. For example, when there is shock formation, there is a sharp variation in the hydrodynamic fields, and one may expect hydrodynamics to break down. One situation where there can be shock formation is when the energy released from a blast is left to propagate freely in an otherwise cold gas. Also, the center of the blast is a low density region where collisions are rare and local equilibrium is difficult to reach. Thus the blast problem is a classic problem to test the validity of hydrodynamics. It was first studied in the context of atomic explosions and underlies the behavior of many astrophysical systems, see [11, 12, 13, 14, 15]. An exploding star sends a blast wave into the stellar medium and later into the interstellar

medium. The released energy is tremendous in astrophysical applications, and hence the assumption of a zero temperature, zero pressure ambient gas, in which the explosion propagates, is an excellent approximation.

One of the central problems is to determine how the shock wave advances and to compute the hydrodynamic fields behind the shock. The blast problem is traditionally studied in the framework of an *ideal* compressible gas neglecting the effect of dissipation. Dimensional analysis [16, 17] allows one to express the radius  $R(t)$  of the shock wave through the time  $t$  counted from the moment of explosion, the released energy  $E_0$  and the density  $\rho_\infty$  in front of the shock

$$R(t) = \left( \frac{E_0 t^2}{A_d \rho_\infty} \right)^{\frac{1}{d+2}}. \quad (2.1)$$

Here  $d$  is the spatial dimension. The amplitude  $A_d$  is a priori unknown, fixing it is a part of the solution. It was shown by Taylor, von Neumann, and Sedov [18, 19, 20, 21, 16] that at long times the hydrodynamic fields behind the shock front have a self-similar scaling form that can be obtained from a solution of the Euler equations. This solution will be referred to as the Taylor-von Neumann-Sedov (TvNS) solution. One of the main issues that we address in this work is the effect of dissipation on the TvNS predictions.

By writing the Navier-Stokes (NS) equations, one can easily see that dissipation in the flow behind the shock is indeed negligible, apart from the region near the center of the explosion where the temperature obtained from ideal hydrodynamics, i.e., Euler equations, diverges. This is physically impossible since the energy injected is finite. Dissipation is thus expected to affect the flow in the region surrounding the origin which we will refer to as the core region. Earlier studies of the influence of heat conduction [22, 23, 24, 25] and viscosity [26, 27, 28, 29] on the blast were performed in the realm of atomic explosions.

Recently, a comparison was made between the results of Newtonian dynamics from molecular dynamics (MD) simulations and that of hydrodynamics in the one-dimensional (1D) alternating mass hard particle (AHP) gas for a blast-like [30, 31] and splash [32] initial condition, and it was found that the TvNS solution describes, surprisingly accurately, the results of MD simulations except in the core of the blast. As expected, due to the effect of dissipation, the TvNS solution fails in the core. It was noted in [30, 31] that the core has size  $X(t) \sim t^{38/93}$  which, at large times, is much smaller than the size of the blast given from Eq. (2.1), for  $d = 1$ , by  $R(t) \sim t^{2/3}$ . The core region does not have a sharp boundary, unlike the shock wave front. An analysis of the hydrodynamic equations including dissipative terms yields a different scaling solution in the core which was compared with results from MD. While dissipation kills the unphysical divergences

of the Euler solution, the detailed agreement between simulations and dissipative hydrodynamics is not very good in the core region. One reason could be the presence of anomalous heat transport in  $d = 1$  [33, 34]. Fourier’s law in one dimension breaks down, and it is replaced by a non-local law [35, 36]. Thus, we expect hydrodynamics to break down in one dimension, and such a breakdown has indeed been observed in [37]. Thus, the near-perfect agreement found between the TvNS solution and molecular dynamics simulations in [30, 31] is quite surprising. It can only be speculated that since the dissipative region is small in the 1D blast problem, much of the perturbed region in the gas is described by dissipation-less Euler equations.

A natural question is to investigate the effect of dissipation in higher dimensions. The first study [38] comparing the predictions of molecular dynamics with those of Euler equations in two dimensions (2D) found a reasonable agreement between the two. Other studies in two and three-dimensional hard-sphere gases [39, 40, 41] found disagreement between the TvNS prediction and MD simulations (even away from the core region). It turns out [42] that the reason for the observed discrepancy in [39] arose from an incorrect estimation of the value of initial energy of the blast used in the simulation. We have verified this in our MD simulations where we find perfect agreement with TvNS in the outer region (see Fig. (2.4) ).

We summarize here the plan of this chapter. In Sec. (2.1), we describe the model, observables and initial condition we studied. In Sec. (2.2), we summarize our main results. In Sec. (2.3.1), we review the TvNS solution. In Sec. (2.3.2), we discuss the effect of dissipation and the new scaling solution that exists in the core. In Sec. (2.3.3), we present numerical results of the NS equations which verify the core scaling forms. We also show that MD simulations satisfy this scaling and point out the agreement between MD and NS. In Sec. (2.4), we present results on the 2D gas when virial corrections in the equation of state are ignored. In Sec. (2.5), we present results on hard rods. Sec. (2.6) contains a brief discussion on the form of the inner and outer solutions in arbitrary dimensions. We conclude in Sec. (2.7) with a discussion.

## 2.1 Models, observables and initial conditions

We consider hard-particle gases with particles that collide elastically. In 2D, it is impossible for a hard point particle gas to reach thermal equilibrium, since there are no collisions for almost all initial conditions and thus the dynamics is trivial. Thus, it is necessary to consider a gas where particles have a finite size. We consider the case where particles are disc-shaped having a non-zero diameter  $a$ , and the particles collide elastically. Thus the

Hamiltonian of such a system having  $N$  particles is given by:

$$H = \sum_{i=1}^N \frac{p_i^2}{2m_i} + \frac{1}{2} \sum_{i,j=1}^N U(|\mathbf{r}_i - \mathbf{r}_j|) \quad (2.2)$$

where the potential  $U$  is the hard core potential:

$$U(r) = \begin{cases} \infty, & \text{if } r < a \\ 0, & \text{otherwise} \end{cases} \quad (2.3)$$

The downside of considering such a hard-disc gas is that the equation of state is no longer given by the ideal gas equation of state, but is replaced by a virial expansion.

In 1D, this is just a hard-rod gas. In 2D we consider all masses to be equal  $m_i = m$ , whereas in 1D, we consider masses  $m_i$  which alternate between two values  $m$  and  $M$  (to ensure non-integrability).

In this work, we consider the evolution of density  $\rho(\mathbf{r}, t)$ , velocity field  $\mathbf{v}(\mathbf{r}, t)$ , and the energy density field  $e(\mathbf{r}, t)$ :

$$\rho(\mathbf{r}, t) = \sum_i \langle m_i \delta(\mathbf{r}_i(t) - \mathbf{r}) \rangle, \quad (2.4a)$$

$$\rho(\mathbf{r}, t) \mathbf{v}(\mathbf{r}, t) = \sum_i \langle m_i \mathbf{v}_i(t) \delta(\mathbf{r}_i(t) - \mathbf{r}) \rangle, \quad (2.4b)$$

$$\rho(\mathbf{r}, t) e(\mathbf{r}, t) = \frac{1}{2} \sum_i \langle m_i |\mathbf{v}_i(t)|^2 \delta(\mathbf{r}_i(t) - \mathbf{r}) \rangle. \quad (2.4c)$$

where  $\mathbf{r}_i(t), \mathbf{v}_i(t)$  are respectively the position and velocity of  $i$ th particle, and  $\langle \dots \rangle$  denotes an average over the ensemble of initial conditions having same values of total number of particles, total momentum (zero in our case), total energy and the same initial profiles of the macroscopic fields viz.  $\rho(\mathbf{r}, 0), \mathbf{v}(\mathbf{r}, 0)$  and  $e(\mathbf{r}, 0)$ . Since we study initial conditions where the blast remains radially symmetric throughout time,  $\rho(\mathbf{r}, t) = \rho(r, t)$ ,  $\mathbf{v}(\mathbf{r}, t) = v(r, t) \hat{r}$ ,  $e(\mathbf{r}, t) = e(r, t)$ .

For the initial condition, we took a blast wave initial condition where all the energy is localized in the central region. More specifically, the initial temperature profile was taken to be  $T(r, 0) = (T_0 / \sqrt{2\pi\sigma^2}) e^{-r^2/2\sigma^2}$  with  $T_0 = E_0 / (\sqrt{2\pi}\rho_\infty\sigma)$ , where  $E_0$  is the energy of the blast,  $\rho(r, 0) = \rho_\infty$  and  $v(r, 0) = 0$ .

In this work we first consider the blast in a 2D gas of hard discs and in a toy 2D gas of point particles. We also consider a 1D gas of hard rods with alternating masses (to

ensure non-integrability) to see if the finite rod size changes the remarkable agreement between MD results and hydrodynamics seen in [30, 31].

## 2.2 Results

Our main results are:

- For the 2D system, we show that, as in 1D, the dissipative terms in the NS equations introduce a new growing length scale which we denote by  $X(t)$ . We find a new self-similar solution in the core, different from the TvNS scaling solution. This core scaling solution is verified from the numerical solution of the NS equations. Thus there are two scaling regions: the bulk region described by TvNS scaling and the core region described by the dissipative scaling. We further show that the two regions are connected by the rules of asymptotic matching.
- We find that NS results agree perfectly with TvNS in the bulk region and also agree with the MD simulation results. The MD results satisfy TvNS scaling in the bulk region and also the core scaling in the central region. However, the scaling functions in the core region are different from the predictions of hydrodynamics.
- For the gas of hard rods in 1D we find an excellent agreement between TvNS, NS and MD simulations in the bulk region, including for the position of the shock front and for the scaling functions. In the blast core, the NS scaling is observed in the MD simulations, but the scaling functions do not agree with those obtained from NS.

## 2.3 Blast in the 2D hard-disc gas

We first consider a gas of hard discs of diameter  $a$ , and mass  $m$ , whose only interaction is via elastic collisions that conserve momentum and energy. Particles move with constant velocities between collisions. The finite size of the particles implies that the equation of state is no longer given by the ideal gas equation. This feature complicates the solution of the hydrodynamic equations. At a microscopic level, the blast initial condition consists of taking an infinite gas of discs that are distributed uniformly in the 2D plane with mass density,  $\rho_\infty$ , and all at rest. Particles inside a localized region are then excited such that their total energy is  $E_0$ , and the total momentum is zero. The excitation then evolves in a radially symmetric way and we are interested, in particular, in how the three conserved

fields of mass density,  $\rho(r)$ , momentum density,  $p(r)$ , and energy density,  $e(r)$ , evolve with time. We first review the TvNS solution as presented in [39], and then we discuss the effect of dissipation by considering the NS equations.

### 2.3.1 TvNS solution

The classic TvNS solution was first obtained for a 3D ideal gas using Euler equations and ignoring any virial corrections caused by the finite cross sectional area of the colliding molecules. A similar analysis was done in [39] for hard-disc gas, but by including the virial corrections in the equation of state.

The first step in finding TvNS solution is to find how the shock front  $R(t)$  grows as a function of time. As discussed above this can be found from purely dimensional analysis. The only variables that the shock front can depend on at large times are time  $t$ , energy injected  $E_0$ , and the ambient density  $\rho_\infty$ . Applying dimensional analysis, we get  $R(t) = [E_0 t^2 / (A_d \rho_\infty)]^{\frac{1}{d+2}}$ , where  $A_d$  is an unknown dimensionless constant, that only depends on the volume fraction  $(\rho_\infty/m)V_d a^d$ , where  $V_d = 2^{-d} \pi^{d/2} / \Gamma(d/2+1)$  is the volume of a  $d$ -dimensional sphere of unit diameter. The Euler equations in any dimension are given by:

$$\partial_t \rho + \partial_i(\rho v_i) = 0, \quad (2.5a)$$

$$\partial_t(\rho v_i) + \partial_j(\rho v_i v_j) + \partial_i P = 0, \quad (2.5b)$$

$$\partial_t(\rho e) + \partial_i(\rho e v_i) + \partial_i(P v_i) = 0, \quad (2.5c)$$

where  $P$  is the pressure, which can be related to the other hydrodynamic fields via equation of state, and  $e$  is the energy per unit mass,  $e = v^2/2 + dT/2$ . Henceforth, in most of the discussions here we set  $a = k_B = m = 1$ , unless otherwise specified.

For the 2D hard-disc gas, the equation of state at low densities is given by the virial equation of state:

$$P = \rho T \left( 1 + \sum_{n=2}^{\infty} B_n \rho^{n-1} \right). \quad (2.6)$$

Following [39], we only take terms up to  $n = 10$ . The values of the constants  $B_n$  are given in [39]. According to TvNS, the blast wave initial condition evolves, at long times to a self-similar scaling form. We define the following scaling variable:

$$\xi = \frac{r}{R(t)}. \quad (2.7)$$

In terms of this dimensionless variable, one again uses dimensional analysis to make the



following ansatz for the long time solution of Eqs. (2.5) for the density, velocity and temperature fields:

$$\rho = \rho_\infty G(\xi), \quad (2.8a)$$

$$v = \frac{r}{t} V(\xi), \quad (2.8b)$$

$$T = \frac{r^2}{t^2} Z(\xi). \quad (2.8c)$$

Putting these scaling forms into the Euler equations, we get the following ODEs for the scaling functions:

$$\xi \left( V - \frac{1}{2} \right) G \frac{dV}{d\xi} + \xi \frac{d}{d\xi} [ZGB(G)] - GV + GV^2 + 2GZB(G) = 0, \quad (2.9a)$$

$$\xi \left( V - \frac{1}{2} \right) \frac{dG}{d\xi} + \xi G \frac{dV}{d\xi} + 2GV = 0, \quad (2.9b)$$

$$- \frac{\xi B(G)}{G} \frac{dG}{d\xi} + \frac{\xi}{Z} \frac{dZ}{d\xi} + 2 \frac{(V-1)}{(V-1/2)} = 0, \quad (2.9c)$$

where

$$B(G) = 1 + \sum_{n=2}^{\infty} B_n \rho_\infty^{n-1} G^{n-1}. \quad (2.10)$$

Under the dynamics of the Euler equations, energy is conserved, and this gives us the further constraint:

$$\int_0^{R(t)} dr \, 2\pi r \rho e = E_0, \quad (2.11)$$

which, in terms of the scaling functions becomes:

$$2\pi \int_0^1 d\xi \, \xi^3 G(\xi) \left( \frac{V^2(\xi)}{2} + Z(\xi) \right) = A_2. \quad (2.12)$$

The boundary conditions required to solve these ODEs are provided by the Rankine-Hugoniot conditions which specify the discontinuity of the fields across the shock:

$$\frac{\rho(R)v(R)}{\rho(R) - \rho_\infty} = \dot{R}, \quad (2.13a)$$

$$\frac{\rho(R)v^2(R) + P(R)}{\rho(R)v(R)} = \dot{R}, \quad (2.13b)$$

$$\frac{\rho(R)v(R)e(R) + P(R)v(R)}{\rho(R)e(R)} = \dot{R}. \quad (2.13c)$$

These, in terms of the scaling functions are given by:

$$\frac{1}{G(1)} \left( 1 + \frac{2}{B[G(1)]} \right) = 1, \quad (2.14a)$$

$$V(1) = \frac{1}{G(1) B[G(1)]}, \quad (2.14b)$$

$$Z(1) = \frac{1}{2} V^2(1). \quad (2.14c)$$

These equations can be solved numerically to find the values of the scaling functions at the shock front, which can be used as boundary values to solve the ODEs. The dimensionless constant  $A_2$  can be found using Eq. (2.12).

### 2.3.2 Effect of dissipation on scaling in the blast core

In the Euler framework, it is assumed that the hydrodynamic fields satisfy the Euler equations throughout the blast and that dissipative terms can be neglected. This assumption is valid only if the dissipative terms corresponding to the TvNS solution are small compared to the Euler terms. The TvNS solution predicts a divergence  $Z(\xi) \sim \xi^{-4}$  for small  $\xi$  which means that the temperature field will have a steep spatial variation. Since the spatial derivatives in the dissipative terms in the NS equations are of one order higher than the Euler terms, this signals that the dissipative terms corresponding to the TvNS solution are much larger than the Euler terms, thus suggesting that dissipation becomes important near the core. However, far from the core, the slopes of the various scaling functions are not steep, so dissipation is not important in those regions. Since dissipation terms far from the core are not important, we expect the ODEs to still hold in the bulk region.

We can estimate the size of the core where dissipation becomes important. The Navier-Stokes equations in  $d$ -dimensions are given by:

$$\partial_t \rho + \partial_i(\rho v_i) = 0, \quad (2.15a)$$

$$\partial_t(\rho v_i) + \partial_j(\rho v_i v_j) + \partial_j \sigma_{ij} = 0, \quad (2.15b)$$

$$\partial_t(\rho e) + \partial_i(\rho e v_i) + \partial_i(\sigma_{ij} v_j) + \partial_i(-\kappa \partial_i T) = 0, \quad (2.15c)$$

with the stress tensor  $\sigma$  given by:

$$\sigma_{ij} = P \delta_{ij} - \mu [\partial_i v_j + \partial_j v_i - \frac{2}{d} (\nabla \cdot \mathbf{v}) \delta_{ij}] - \zeta (\nabla \cdot \mathbf{v}) \delta_{ij}, \quad (2.16)$$

where  $\mu$  is the shear viscosity,  $\zeta$  is the bulk viscosity and  $\kappa$  is the heat conductivity.

Kinetic theory predicts that  $\mu = D_\mu \sqrt{T}$ ,  $\kappa = D_\kappa \sqrt{T}$  and  $\zeta = 0$  for a monoatomic gas in the low density limit [3, 43], where  $D_\kappa$  and  $D_\mu$  are some constants. However, we emphasize that these results are only first order terms in a virial expansion [3]. For a radially symmetric blast, all the hydrodynamic fields are radially symmetric. Using this fact, the NS equations become (for  $d = 2$ ):

$$\partial_t \rho + \frac{\rho v}{r} + \partial_r(\rho v) = 0, \quad (2.17a)$$

$$\rho(\partial_t v + v \partial_r v) + \partial_r P = \frac{1}{r^2} \partial_r [r^2 \mu (\partial_r v - r^{-1} v)], \quad (2.17b)$$

$$\rho(\partial_t e + v \partial_r e) + \frac{1}{r} \partial_r (r P v) = \mu (\partial_r v - \frac{v}{r})^2 + \frac{v}{r^2} \partial_r [r^2 \mu (\partial_r v - \frac{v}{r})] + \frac{1}{r} \partial_r (r \kappa \partial_r T). \quad (2.17c)$$

It is known [39], that the TvNS solution predicts (in 2D) that for small  $\xi$ ,  $G \sim \xi^2$ ,  $V - 1/4 \sim \xi^4$  and  $Z \sim \xi^{-4}$  [see also Sec. (3.4)]. Using this small  $\xi$  behaviour predicted by TvNS solution, we can estimate if the dissipation terms are indeed small, e.g., by looking at the ratio of the terms on the right and left hand sides of Eq. (2.17b). This shows that dissipation is small for  $r \gtrsim D_\mu^{1/5} E_0^{1/5} \rho_\infty^{-2/5} t^{2/5}$ , thus verifying the assumption leading to the TvNS solution. However, for  $r \lesssim D_\mu^{1/5} E_0^{1/5} \rho_\infty^{-2/5} t^{2/5}$ , dissipation terms are larger than Euler terms, and thus the assumption leading to TvNS solution breaks down. Hence, we expect TvNS solution not to be valid for  $r \lesssim D_\mu^{1/5} E_0^{1/5} \rho_\infty^{-2/5} t^{2/5}$ . This introduces a new length scale, which is an estimate of the size of the core,

$$X(t) = \frac{D_\mu^{1/5} E_0^{1/5}}{\rho_\infty^{2/5}} t^{2/5}, \quad (2.18)$$

and which grows with time as  $t^{2/5}$ . From this length scale, we can find an estimate for the density, velocity and temperature in the core, which we denote respectively by  $\rho^*$ ,  $v^*$  and  $T^*$ . This will give us new density, velocity and temperature scales (here  $\xi_* = X(t)/R(t)$  is the scaled size of the core):

$$\rho^* = \rho_\infty \xi_*^2 = b_\rho t^{-1/5}, \quad (2.19a)$$

$$v^* = \frac{X(t)}{t} = b_v t^{-3/5}, \quad (2.19b)$$

$$T^* = \frac{X^2(t)}{t^2} \xi_*^{-4} \sim b_T t^{-4/5}, \quad (2.19c)$$

where  $b_\rho = A^{1/2} D_\mu^{2/5} \rho_\infty^{7/10} E_0^{-1/10}$ ,  $b_v = D_\mu^{1/5} \rho_\infty^{-2/5} E_0^{1/5}$  and  $b_T = A^{-1} D_\mu^{-2/5} \rho_\infty^{-1/5} E_0^{3/5}$ . From

these scales, we can construct a new scaling form for the various hydrodynamic fields:

$$\rho = t^{-\frac{1}{5}} \tilde{G}(\eta), \quad (2.20a)$$

$$v = t^{-\frac{3}{5}} \tilde{V}(\eta), \quad (2.20b)$$

$$T = t^{-\frac{4}{5}} \tilde{Z}(\eta), \quad (2.20c)$$

where we have defined the new scaling variable

$$\eta = \frac{r}{t^{2/5}}, \quad (2.21)$$

and the constants have been absorbed into the scaling functions  $\tilde{G}$ ,  $\tilde{V}$  and  $\tilde{Z}$ .

To get the ODEs satisfied by the core scaling functions  $\tilde{G}(\eta)$ ,  $\tilde{V}(\eta)$  and  $\tilde{Z}(\eta)$ , we plug the scaling ansatz (Eqs. (2.20)) into the NS equations and take the long time limit. We get the following coupled ODEs:

$$-\frac{\tilde{G}}{5} - \frac{2\eta\tilde{G}'}{5} + \frac{(\eta\tilde{G}\tilde{V})'}{\eta} = 0, \quad (2.22a)$$

$$(\tilde{Z}\tilde{G})' = 0, \quad (2.22b)$$

$$-\frac{4}{5}\tilde{Z}\tilde{G} - \frac{2\eta\tilde{G}\tilde{Z}'}{5} + \tilde{G}\tilde{V}\tilde{Z}' + \frac{\tilde{Z}\tilde{G}\tilde{V}}{\eta} + (\tilde{G}\tilde{V}\tilde{Z})' = \frac{D_\kappa\tilde{Z}^{1/2}\tilde{Z}'}{\eta} + \frac{2}{3}(D_\kappa\tilde{Z}^{3/2})''. \quad (2.22c)$$

We note the following: (a) The virial corrections do not appear in these equations because they vanish in the long time limit; (b) only the thermal conductivity term makes an appearance [this is true also if we consider the form of transport coefficients in Eq. (2.32)]. These ODEs are first order in  $\tilde{G}$  and  $\tilde{V}$  and second order in  $\tilde{Z}$ . Thus, we need 4 boundary values: two for each  $\tilde{G}$  and  $\tilde{V}$ , and two for  $\tilde{Z}$ . Two of the boundary conditions can be determined using the radial symmetry of the problem. Because of radial symmetry, there is no flow velocity and heat flow in the origin. This gives  $\tilde{V}(\eta = 0) = 0$  and  $\tilde{Z}'(\eta = 0) = 0$ . The rest two boundary conditions can be determined from the asymptotic matching condition, which is given by:

$$h(\eta \rightarrow \infty) = h(\xi \rightarrow 0), \quad (2.23)$$

where  $h$  is some hydrodynamic field.

We call the solution obtained from the ODEs in Eqs. (2.9) for the TvNS scaling functions as the *outer solution*, and those obtained from the ODEs in Eqs. (2.22) for the core scaling functions as the *inner solution*. We have not succeeded in finding analytical expressions for the inner solution. However, approximate solutions can be found in the

small  $\eta$  region, as we now show. Since  $\tilde{V}(0) = 0$  and  $\tilde{Z}'(0) = 0$  we can take for small  $\eta$ :

$$\tilde{V}(\eta) \approx V_0 \eta^\alpha, \alpha > 0, \quad (2.24)$$

$$\tilde{Z}'(\eta) \approx F_0 \eta^\beta, \beta > 0. \quad (2.25)$$

Thus,

$$\tilde{Z}(\eta) = F_0 \frac{\eta^{1+\beta}}{1+\beta} + C_1, \text{ for small } \eta. \quad (2.26)$$

Using these and Eq. (2.22b), we have

$$\tilde{G} = \frac{C_2}{\tilde{Z}} \approx \frac{C_2}{C_1} \left( 1 - \frac{F_0 \eta^{1+\beta}}{C_1(1+\beta)} \right), \text{ for small } \eta. \quad (2.27)$$

Putting these into Eq. (2.22a) and comparing powers and taking small  $\eta$  limit, we get  $\alpha = 1$ ,  $V_0 = 1/10$ . Using these values for  $\alpha$  and  $V_0$  and Eq. (2.22c), we get:

$$\begin{aligned} & -\frac{3C_2}{5} - \frac{2\eta C_2 F_0}{5C_1} \left( \eta^\beta - \frac{F_0 \eta^{1+2\beta}}{C_1(1+\beta)} \right) + \frac{C_2 F_0}{10C_1} \left( \eta^{1+\beta} - \frac{F_0 \eta^{2+2\beta}}{C_1(1+\beta)} \right) \\ & - F_0 D_\kappa \sqrt{C_1} \left( \eta^{\beta-1} + \frac{F_0 \eta^{2\beta}}{2C_1(1+\beta)} \right) - D_\kappa \sqrt{C_1} F_0 \beta \eta^{\beta-1} = 0. \end{aligned} \quad (2.28)$$

Since  $\beta > 0$ , the equation above can only be satisfied when  $\beta = 1$  and

$$F_0 = -\frac{3C_2}{10D_\kappa \sqrt{C_1}}. \quad (2.29)$$

The only unknown constants are  $C_1$  and  $C_2$ , which can be fixed from boundary values determined from either asymptotic matching or the data from the numerical solution of the full NS Eqs. (2.17).

Thus to first non-zero order in  $\eta$ , we have:

$$\tilde{G}(\eta) = \frac{C_2}{C_1} \left( 1 + \frac{3C_2 \eta^2}{20D_\kappa C_1^{3/2}} + \dots \right), \quad (2.30a)$$

$$\tilde{V}(\eta) = \frac{\eta}{10} + \dots, \quad (2.30b)$$

$$\tilde{Z}(\eta) = C_1 - \frac{3C_2 \eta^2}{20D_\kappa \sqrt{C_1}} + \dots \quad (2.30c)$$

### 2.3.3 Numerical results

From the discussions in the previous two subsections, we expect two different scaling form for the hydrodynamic fields, namely the TvNS scaling form given by Eqs. (2.8) in the

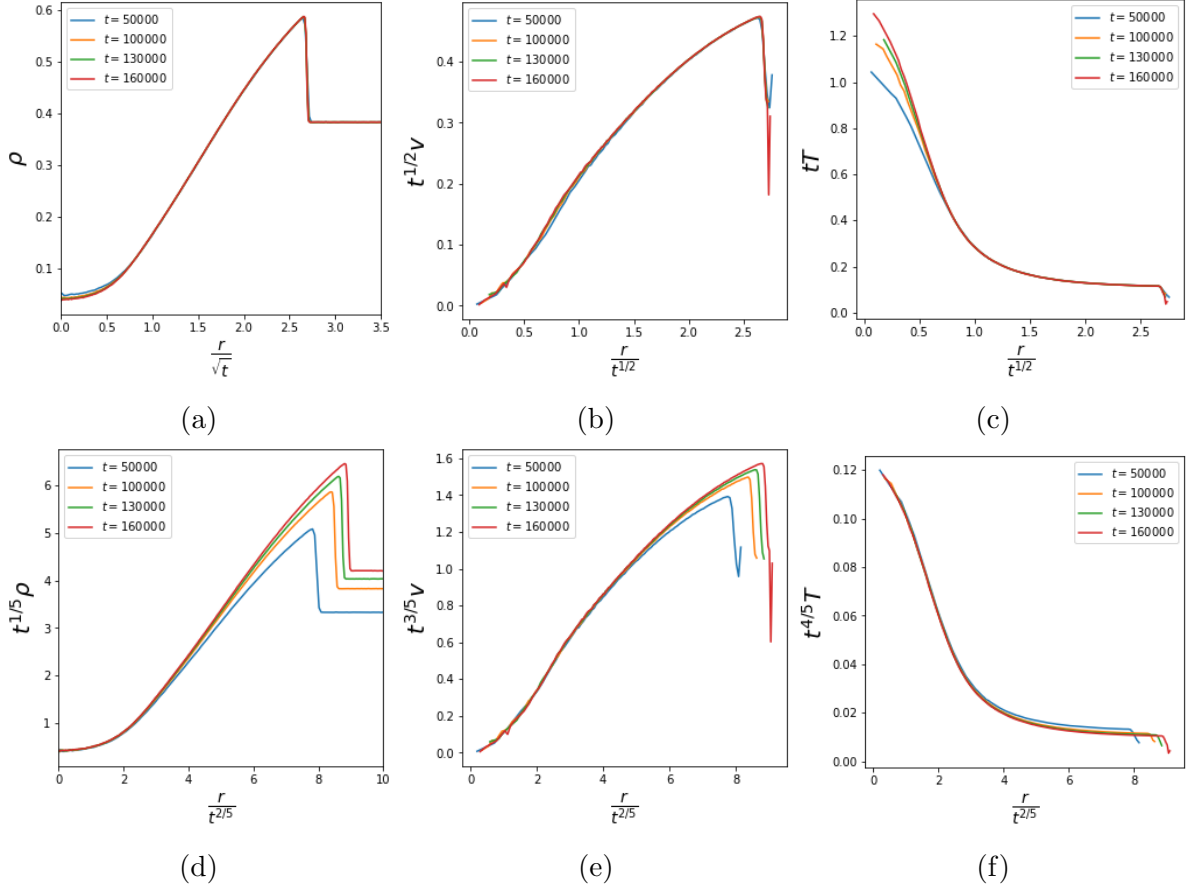


Figure 2.1: **MD simulations of hard discs:** The three hydrodynamic fields, obtained from MD simulation data of Ref. [39], plotted in (a,b,c) according to the expected TvNS scaling form [Eqs. (2.8)] and in (d,e,f) according to the expected core scaling form [Eqs. (2.20)]. We can see that in (a,b,c) there is a very good collapse of data everywhere except near the core, where the scaling is not very good, especially for the temperature field. On the other hand in (d,e,f) we see excellent data collapse near the core. Thus MD simulations exhibit the expected core and bulk scaling forms.

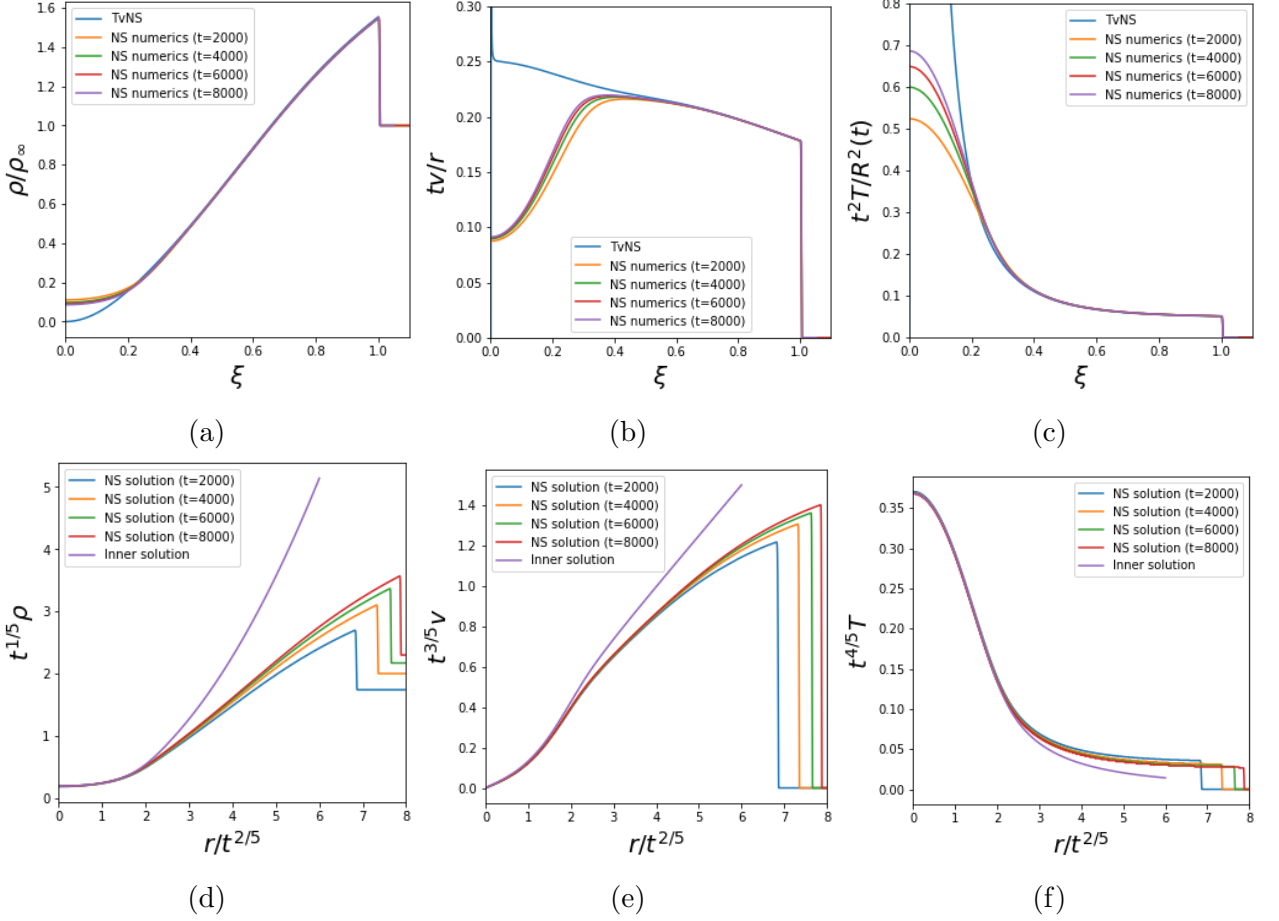


Figure 2.2: **NS solution for hard discs:** The three hydrodynamic fields, obtained from numerical solution of NS equations in Eq. (2.17), are plotted in (a,b,c) according to the expected TvNS scaling form [Eqs. (2.8)] and in (d,e,f) according to the expected core scaling form [Eqs. (2.20)]. We can see that in (a,b,c) there is a very good collapse of data everywhere except near the core. On the other hand in (d,e,f) we see excellent data collapse near the core. Thus the NS solutions exhibit the expected core and bulk scaling forms. In (a,b,c) we also see a good fit of the scaled data to the TvNS scaling functions,  $(G, V, Z)$ , also obtained from a numerical solution of Eqs. (2.9). In (d,e,f) we see a reasonable fit in the core region to the core scaling functions,  $(\tilde{G}, \tilde{V}, \tilde{Z})$ , obtained from a numerical solution of Eqs. (2.22) with boundary conditions obtained from the solution of the NS equations in Eqs. (2.17). The parameter values were taken as  $E_0 = 4.0$ ,  $\rho_\infty = 0.382$ , and the Henderson equation of state was used.

bulk region  $X(t) \lesssim r < R(t)$ , and the core scaling form given by Eqs. (2.20) in the region  $0 < r \lesssim X(t)$ . We now check if these predictions for the bulk and core scaling forms can be verified in data obtained from MD simulations and from numerical solutions of the NS equations.

We use the MD simulation results from Ref. [39]. They considered a gas of hard discs with diameter  $a = 1$ ,  $E_0 = 2.0$  and  $\rho_\infty = 0.382$ . The initial condition was chosen with a Gaussian temperature profile,  $v(\mathbf{r}, t = 0) = 0$  and  $\rho(\mathbf{r}, t = 0) = \rho_\infty$ . The parameters of the Gaussian temperature profile were chosen such that the initial total energy is  $E_0$ . We note here that the long-time scaling solution does not depend on the width of the Gaussian chosen as long as it corresponds to energy  $E_0$ . For the numerical solution of the NS equations in Eqs. (2.17), we considered initial conditions that correspond to the ones used in the MD simulations. In all our computations involving hard-disc gas, we use the Henderson equation of state (EOS) [44] instead of the truncated virial expansion for the ease of computation. The Henderson EOS is given by:

$$p = \rho T \frac{128 + \pi^2 \rho^2 a^4}{8(4 - \pi \rho a^2)^2}. \quad (2.31)$$

The MacCormack method [45] was used to solve the PDEs, with discretization given by  $dx = 0.05$ ,  $dt = 10^{-5}$ . The boundary conditions we have used are  $v(0, t) = 0$ ,  $\partial_r \rho(r, t)|_{r=0} = 0$ ,  $\partial_r T(r, t)|_{r=0} = 0$ . The initial temperature profile was taken to be a Gaussian:  $T(r, 0) = (T_0/\sqrt{2\pi\sigma^2})e^{-r^2/2\sigma^2}$ , with  $T_0 = E_0/(\sqrt{2\pi}\rho_\infty\sigma)$  and  $\sigma = 0.5$ . We note that the lowest order non-zero term of the Enskog expansion for the transport coefficients gives [46, 47, 43, 48]

$$\kappa = \frac{2}{a\pi^{1/2}} T^{1/2}, \quad \mu = \frac{1}{2a\pi^{1/2}} T^{1/2}, \quad \zeta = \frac{8\phi^2}{\pi^{3/2}} T^{1/2} = \frac{\pi^{1/2}a^3}{2} \rho^2 T^{1/2}, \quad (2.32)$$

where  $\phi = \pi a^2 \rho/4$  is the volume fraction. An important general property of monoatomic gases is the vanishing of the bulk viscosity in the dilute regime,  $\phi \rightarrow 0$ . This, together with relation  $\gamma = 1 + 2/d$ , is the crucial input coming from kinetic theory [3, 43, 48]; phenomenological hydrodynamics is compatible with arbitrary  $\gamma > 1$  and  $\zeta \geq 0$ . When  $\phi > 0$ , the bulk viscosity becomes positive, and Eq. (2.32) gives its leading asymptotic for small  $\phi$ . We note here that the  $\rho$ -dependence of the bulk viscosity will not change the core scaling, as the core is a low density region where bulk viscosity is negligible.

In our NS numerics we followed Ref. [41] and chose (with  $a = 1$ ) the values  $\kappa = \mu = (\sqrt{\pi}/8)\sqrt{T}$  and  $\zeta = 0$ , which are different from those in Eqs. (2.32). We have verified that our main conclusions remain unchanged on using Eqs. (2.32) for the transport coefficients.

**MD simulations:** In Fig. (2.1) we show the results of MD simulation data and check



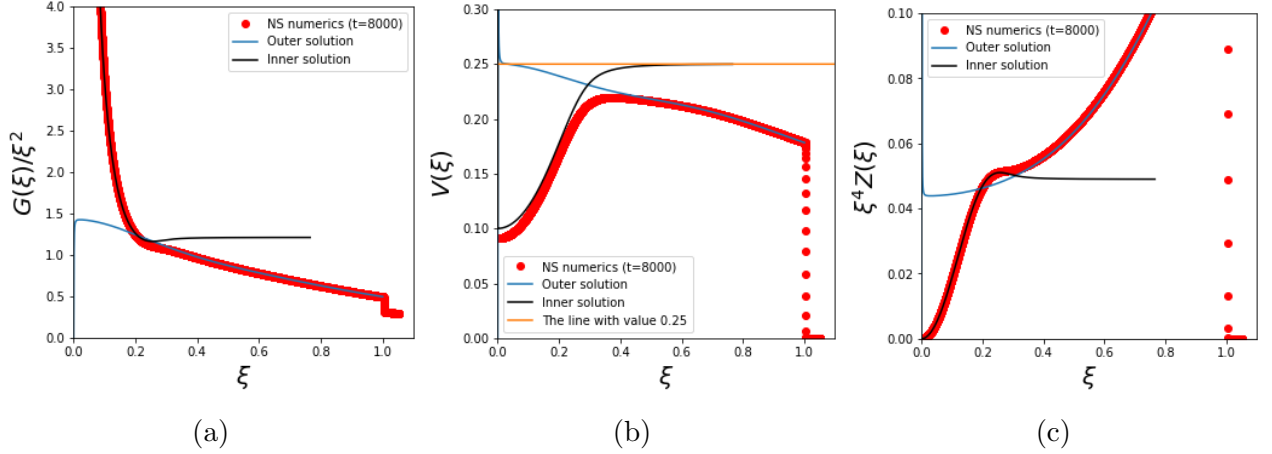


Figure 2.3: **Asymptotic matching in hard discs:** Figure comparing the inner solution and outer solution with the full solution of NS equations. The boundary values for finding the inner solution were taken from the full solution of the NS equations. Also shown in the middle plot is the line with height 0.25 which is the near core value of  $V(\xi)$  predicted by the TvNS solution. We see that the near core asymptotic of the outer solution matches with the far core asymptotic of the inner solution, which is nothing but the rule of asymptotic matching.

if they satisfy the predicted scaling. In Figs. (2.1a, 2.1b, 2.1c), following Eqs. (2.8), we plot the scaled fields  $(\rho, t^{1/2}v, tT)$  as a function of  $r/t^{1/2}$ , at different times, and find that this gives a very good data collapse in the region far from the core. However, as expected, the data collapse near the core is not quite good. In Figs. (2.1d, 2.1e, 2.1f), we follow Eqs. (2.20) and plot the scaled fields  $(t^{1/5}\rho, t^{3/5}v, t^{4/5}T)$  as a function of  $r/t^{2/5}$  and see that this scaling gives a much better data collapse in this region. This establishes that there are two different regions with different scaling.

**NS equations:** We now discuss the results obtained from the numerical solution of NS equations. In Fig. (2.2), we plot the hydrodynamic fields obtained from the numerical solution of the NS equations. In Figs. (2.2a, 2.2b, 2.2c) we verify that these satisfy the TvNS scaling form in the bulk region and agree very well with the TvNS scaling functions. However, in the core we see a clear departure from TvNS scaling. In Figs. (2.2d, 2.2e, 2.2f) we see that the core scaling form is satisfied in the core region. We also plot the solution of Eqs. (2.22) and we see that they agree with the numerical solution of NS equations in the core region.

**Asymptotic matching:** In Fig. (2.3), we verify the rules of asymptotic matching by using the inner and outer solutions. Once we have the inner solution  $\tilde{G}$ ,  $\tilde{V}$  and  $\tilde{Z}$ , we can find the corresponding hydrodynamic fields for density, velocity and temperature. We can then compare how they match with the outer solution. In Fig. (2.3), we show this comparison and find that the  $\xi \rightarrow 0$  limit of the outer solution has the same asymptotic as the  $\xi \rightarrow \infty$  of the inner solution. Thus we verify the rule of asymptotic matching.

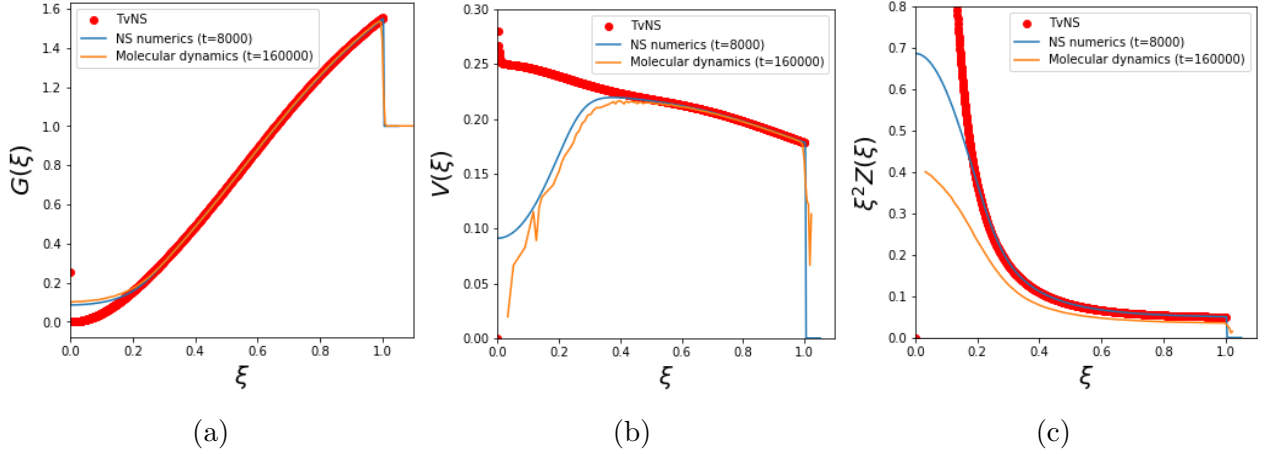


Figure 2.4: **2D hard discs**: Comparison of the NS solution and TvNS with MD simulations. We see that the MD data matches with both the NS or TvNS solution in the bulk region.

Finally in Fig. (2.4), we compare MD data of [39] (with the same value of  $E_0$ ) with NS solution and TvNS solution. We see that NS and TvNS solutions agree with MD data. The only discrepancies are in the near core behavior for the scaling functions.

## 2.4 Blast in 2D ideal gas

In this section, we consider the hydrodynamics of a toy model of a 2D gas, where we ignore the virial corrections in the equation of state, and take it to be that of an ideal gas. This amounts to considering point particles which in two dimensions would mean a non-interacting gas. So naively we would not expect any evolution. However, one can work in the Boltzmann-Grad limit, that is,  $a \rightarrow 0$  and  $\rho \rightarrow \infty$  keeping  $\rho a$  finite (in 2D). In this situation, one expects finite transport coefficients predicted by kinetic theory, while still preserving the ideal gas equation of state (since the volume fraction  $\pi \rho a^2/4 \rightarrow 0$ ). This system would be very difficult to simulate but we can still analyze the NS equations. One advantage of this toy model is that we can find an exact TvNS solution.

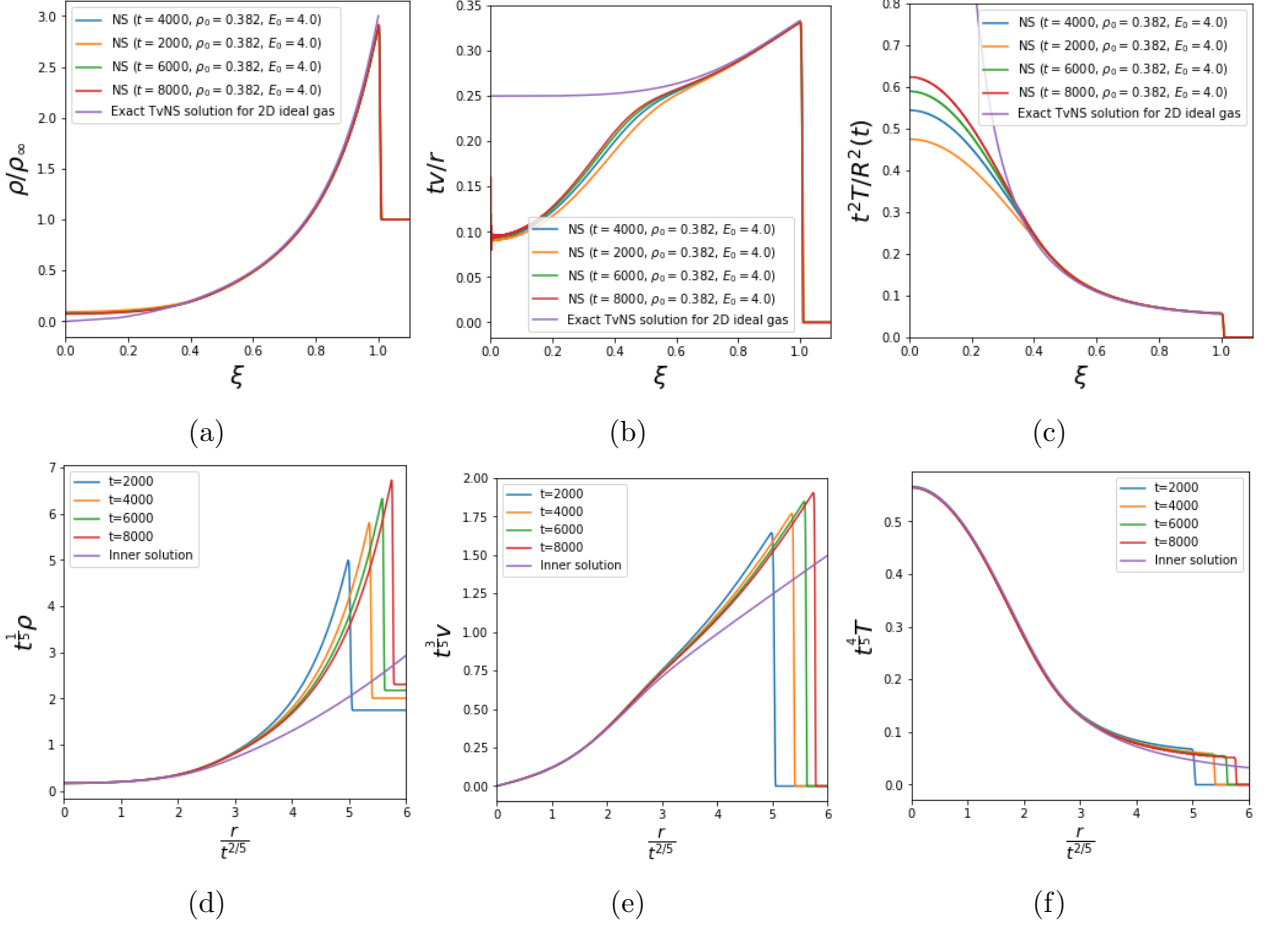


Figure 2.5: **NS solution for 2D hard point gas:** The three hydrodynamic fields, obtained from numerical solution of NS equations in Eq. (2.17) with ideal gas equation of state, are plotted in (a,b,c) according to the expected TvNS scaling form in Eqs. (2.33) and in (d,e,f) according to the expected core scaling form [Eqs. (2.20)]. We can see that in (a,b,c) there is a very good collapse of data everywhere except near the core. On the other hand in (d,e,f) we see excellent data collapse near the core. Thus the NS solutions exhibit the expected core and bulk scaling forms. In (a,b,c) we also see a good fit of the scaled data to the TvNS scaling functions ( $G, V, Z$ ), obtained from the exact solution [ Eqs. (2.35),(2.37)]. In (d,e,f) we see a reasonable fit in the core region to the core scaling functions  $\tilde{G}, \tilde{V}, \tilde{Z}$ , obtained from a numerical solution of Eqs. (2.22) with boundary conditions obtained from the solution of the hard point NS equations (PDEs). The parameter values were taken as  $E_0 = 4.0$ ,  $\rho_\infty = 0.382$ .

### 2.4.1 TvNS solution

For this toy model, our first aim is to find the TvNS solution. To this end we take the following scaling ansatz for the form of the hydrodynamic fields at long times:

$$\rho = \rho_\infty G(\xi), \quad (2.33a)$$

$$v = \frac{r}{t} V(\xi), \quad (2.33b)$$

$$T = \frac{r^2}{t^2} Z(\xi), \quad (2.33c)$$

where  $\xi = r/R$ ,  $R(t) = (E_0 t^2 / (A_2 \rho_\infty))^{1/4}$  and  $A_2$  is some dimensionless constant that we will determine later. Using these scaling ansatz, the Euler equations can be reduced to the following equations

$$\left(V - \frac{1}{2}\right) G \xi \frac{dV}{d\xi} + \xi \frac{d}{d\xi} (ZG) - GV + GV^2 + 2GZ = 0, \quad (2.34a)$$

$$\left(V - \frac{1}{2}\right) \xi \frac{dG}{d\xi} + \xi G \frac{dV}{d\xi} + 2GV = 0, \quad (2.34b)$$

$$- \left(V - \frac{1}{2}\right) \frac{\xi}{G} \frac{dG}{d\xi} + \left(V - \frac{1}{2}\right) \frac{\xi}{Z} \frac{dZ}{d\xi} + 2(V - 1) = 0. \quad (2.34c)$$

As a result of the scaling form we see that the total energy in the region  $0 < r < \xi R(t)$  is conserved. This leads to the following integral of motion (see also Ref. [17] for an alternate derivation):

$$Z = \frac{V^2(1 - 2V)}{2(4V - 1)}. \quad (2.35)$$

The Rankine-Hugoniot boundary conditions give us

$$G(1) = 3, \quad V(1) = \frac{1}{3}, \quad Z(1) = \frac{1}{18}. \quad (2.36a)$$

These equations can be solved to give

$$\xi^4 = \frac{|4V - 1|}{108V^2 \left(V - \frac{1}{2}\right)^2}, \quad (2.37a)$$

$$G = \frac{3\sqrt{3}\sqrt{|4V - 1|}e^{-\frac{1}{2V-1}}}{e^3}. \quad (2.37b)$$

Together with Eq. (2.35), these provide a complete solution of Eqs. (2.34), except that the value of the constant  $A_2$  is still undetermined. This can be found easily by using the

conservation of energy, exactly as it was done in [30, 31] for the case of 1D ideal gas:

$$A_2 = 2\pi \int_0^1 G(\xi) \left( \frac{V^2(\xi)}{2} + Z(\xi) \right) \xi^3 d\xi. \quad (2.38)$$

Plugging the exact solution for  $G$ ,  $V$ ,  $Z$ , we will obtain an expression for  $A_2$  as an integral which cannot be evaluated exactly, but can be evaluated numerically. After doing the full calculation we obtain  $A_2 = 0.3519359068$ .

Using the exact solution, one finds that the following  $\xi \rightarrow 0$  behaviour of the various scaling functions:

$$V - \frac{1}{4} \sim \xi^4, \quad G \sim \xi^2, \quad Z \sim \xi^{-4}. \quad (2.39)$$

## 2.4.2 Core scaling solution

Just like we observe a new scaling in the core region for hard discs, we expect a similar new scaling in the core region for our toy model. Following the same argument as in Sec. (2.3.2), and using the fact that the  $\xi \rightarrow 0$  behaviour of the TvNS solution, Eq. (2.39), remains the same as for hard discs, we see immediately that again the size of the dissipative core grows with time as  $t^{2/5}$ . It is clear also that the core scaling form will again be exactly as in Eq. (2.20). Finally, we note that the higher order terms, in the virial expansion for pressure in the hard-disc gas, do not appear in the equations for the scaling functions  $\tilde{G}(\eta)$ ,  $\tilde{V}(\eta)$ ,  $\tilde{Z}(\eta)$  in Eq. (2.22). Hence we have the same ODE equations in the core as for our 2D point particle gas. As before we need two boundary conditions to be determined either from NS data, or from the asymptotic matching condition, which is given by Eqs. (2.23). The boundary conditions are different for the hard point gas and will lead to a different solution for the scaling functions.

## 2.4.3 Numerical results

In Fig. (2.5), we compare results from NS solutions with the predicted TvNS and core scaling forms. In Fig. (2.5)(a,b,c), we see that the NS shock front matches with the TvNS prediction. We also see a clear TvNS scaling in the bulk region but significant departures in the core. Plotting the exact TvNS scaling functions, we notice that they agree with the bulk NS results. In Fig. (2.5)(d,e,f), we verify that the NS solutions satisfy the core scaling. The comparison between the numerical solution of the core scaling ODEs in Eqs. (2.22) and that of the full NS equations is also good in the collapsed region. For the

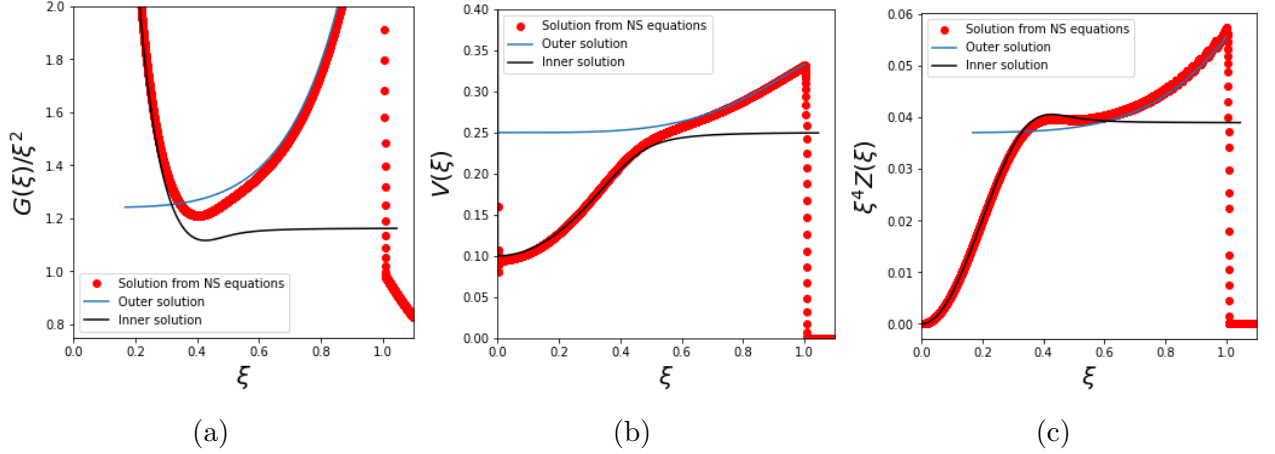


Figure 2.6: **2D hard point gas**: In this figure, the inner core scaling solution, the exact TvNS solution and the solution obtained from the full NS equations are plotted together. The boundary values for finding the inner solution were taken from the full solution of the NS equations. We see that the near core asymptotics of outer solution matches with the far core asymptotics of inner solution, which is nothing but the rule of asymptotic matching.

solution of Eqs. (2.22), we took the boundary conditions from the full solution of the NS equations.

In Fig. (2.6) we plot the exact TvNS solution, the core scaling functions and the solution from the full NS equations. We see a very good verification of the rules of asymptotic matching.

## 2.5 Blast in the hard-rod gas

In this section, we consider the blast problem in the 1D hard-rod gas, and compare the predictions of MD simulations with those of NS equations and TvNS solution.

We consider a gas of hard rods of length  $a$ . If all the hard rods are of equal masses, the particles simply exchange velocities during collisions, hence the system would be integrable and never reach local equilibrium. Thus, as in [30, 31], we consider the alternate mass hard-rod gas where successive rods on the line have masses  $m$  and  $M > m$  with mean mass  $\bar{m} = (m + M)/2 = 1$ . In units where  $k_B = 1$ , the equation of state for this hard-rod gas is given by:

$$P = \frac{\rho T}{1 - \rho a}. \quad (2.40)$$

### 2.5.1 TvNS solution

The shock front in 1D grows with time as  $R(t) = \left(\frac{E_0 t^2}{A_1 \rho_\infty}\right)^{\frac{1}{3}}$ , where  $\rho_\infty$  is the background density. As usual, we choose this growing length scale to define the TvNS scaling variable  $\xi = x/R(t)$  and the following scaling forms for the hydrodynamic fields:

$$\rho = \rho_\infty G(\xi), \quad v = \frac{x}{t} V(\xi), \quad T = \frac{x^2}{t^2} Z(\xi). \quad (2.41)$$

Plugging these into the Euler equations, we get the following ODEs for the scaling functions:

$$-\frac{2}{3}\xi G' + \xi(GV)' + GV = 0, \quad (2.42a)$$

$$-V + V^2 - \frac{2\xi V'}{3} + \xi VV' + \frac{\xi ZG'}{G(1-\phi G)^2} + \frac{2Z}{1-\phi G} + \frac{\xi Z'}{1-\phi G} = 0, \quad (2.42b)$$

$$-2Z - \frac{2\xi Z'}{3} + 2ZV + \xi VZ' + \frac{2ZV}{1-\phi G} + \frac{2\xi ZV'}{1-\phi G} = 0, \quad (2.42c)$$

where  $\phi = \rho_\infty a$  is the background packing fraction. As a result of the scaling form we see that the total energy in the region  $0 < r < \xi R(t)$  is conserved. This leads to the following integral of motion [17]:

$$Z = \frac{V^2(1 - 3V/2)}{3V/2 + 3V(1 - \phi G)^{-1} - 1}. \quad (2.43)$$

The Rankine-Hugoniot conditions give the following boundary values needed to solve Eqs. (2.42):

$$G(1) = \frac{2}{1+\phi}, \quad V(1) = \frac{1-\phi}{3}, \quad Z(1) = \frac{(1-\phi)^2}{9}. \quad (2.44)$$

These equations have to be solved along with the equation which specifies the total energy, which will fix the constant  $A_1$ . For point particles, Eq. (2.43) makes it possible to solve the TvNS equations in any dimensions. However, for the case of hard rods we have not been able to find a closed form solution. We have verified numerically that the numerical solution of the ODEs above have the same behaviour near the core as the TvNS solution of ideal gas obtained in [30, 31], i.e.,

$$G(\xi) \sim |\xi|^{1/2}, \quad V(\xi) = 2/9, \quad Z(\xi) \sim |\xi|^{-5/2}, \quad (2.45)$$

for small  $\xi$ . This is expected as the small  $\xi$  region is a region of low density making the virial corrections almost negligible and the gas ideal.

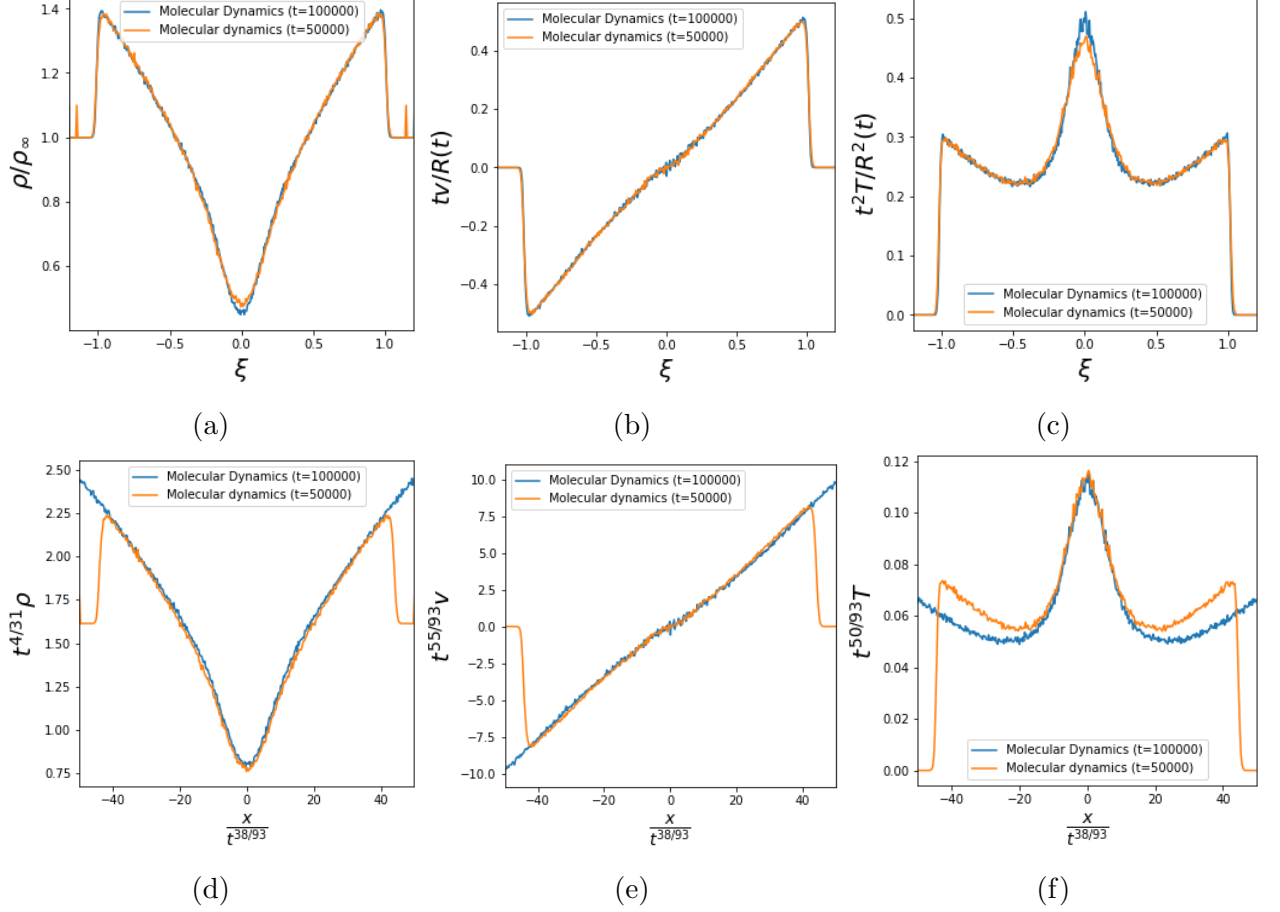


Figure 2.7: **Hard rods**: Plot checking the TvNS scaling in (a,b,c) and the new scaling in the core (obtained by including the dissipative effects) in (d,e,f) from the results of MD simulation. We can see that there is a nice collapse of data at two different times in the bulk region in (a,b,c) and in the core region in (d,e,f). We have taken  $\rho_\infty = 0.4$ ,  $E_0 = 0.4$ .

## 2.5.2 Core scaling solution

Following Refs. [30, 31], we take for the heat conductivity in NS to be of the form  $\kappa = D_\kappa \rho^{1/3} T^{1/2}$ . An analysis similar to the one we did in Sec. (2.3.2) leads us then to a core growing as  $X(t) \sim t^{38/93}$  and the following forms for the scaling near the core:

$$\rho = t^{-\frac{4}{31}} \tilde{G}(\eta), \quad (2.46a)$$

$$v = t^{-\frac{55}{93}} \tilde{V}(\eta), \quad (2.46b)$$

$$T = t^{-\frac{50}{93}} \tilde{Z}(\eta), \quad (2.46c)$$

where  $\eta = xt^{-38/93}$ .

We can solve for the core scaling functions similar to the way we did it for hard discs. Since the virial corrections to the equation of state are negligible in the core and the gas



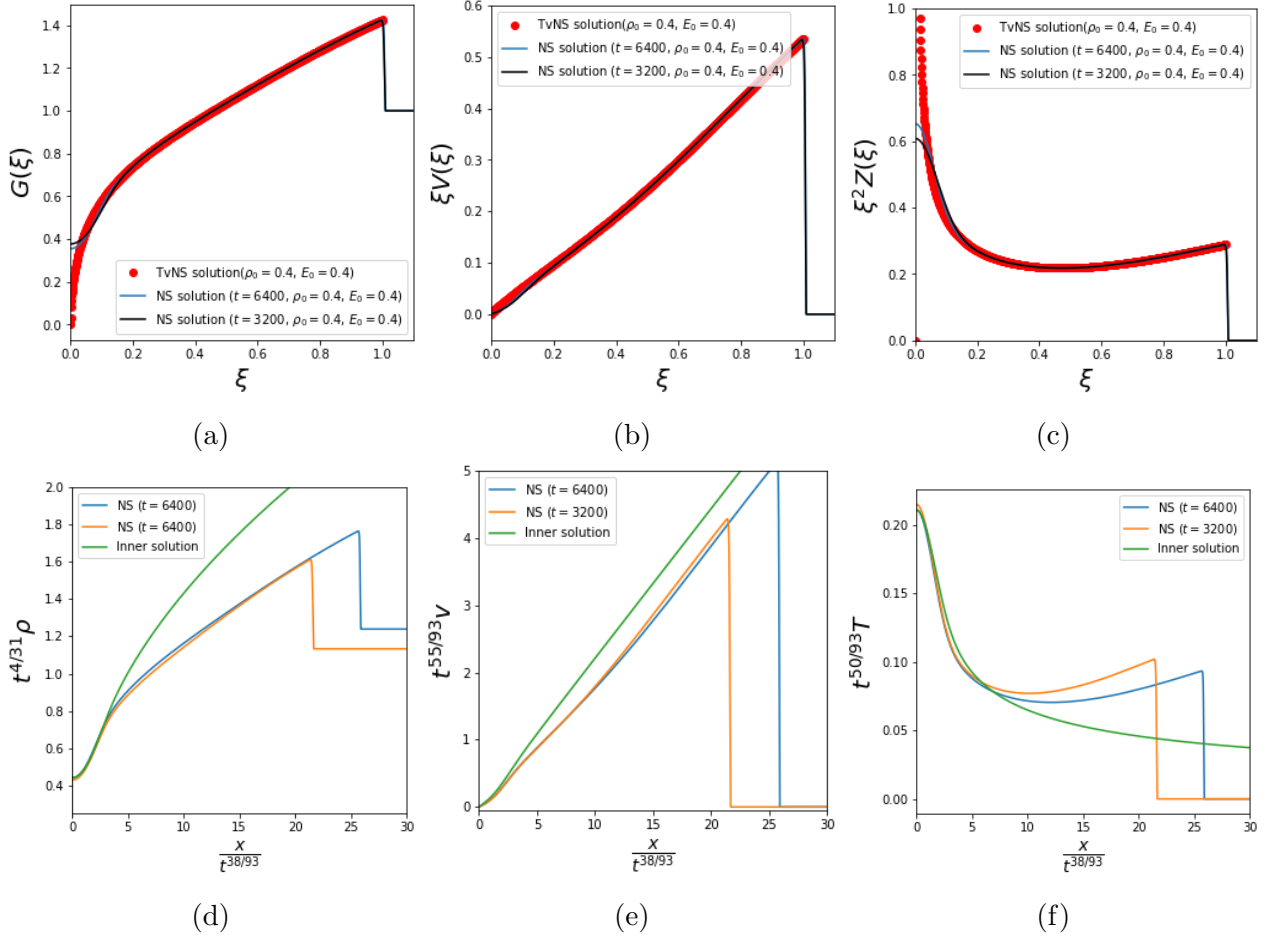


Figure 2.8: **Hard rods**: Plot checking the TvNS scaling in (a,b,c) and the new scaling in the core (obtained by including the dissipative effects) in (d,e,f) from numerical solution of the NS equations. Also shown are the outer solution in (a,b,c) and the inner solution in (d,e,f). We can see that there is a nice collapse of data at two different times in the bulk region in (a,b,c) and in the core region in (d,e,f). We can also see that the outer solution matches with the NS data in the bulk region in (a,b,c) and the inner solution matches with the NS data in the core region in (d,e,f). We have taken  $\rho_\infty = 0.4$ ,  $E_0 = 0.4$ .

is almost ideal, we directly take the equations for the core scaling functions from [31]:

$$-\frac{4}{31}\tilde{G} - \frac{38}{93}\eta\tilde{G}' + (\tilde{G}\tilde{V})' = 0, \quad (2.47a)$$

$$(\tilde{G}\tilde{Z})' = 0, \quad (2.47b)$$

$$-\frac{25}{93}\tilde{G}\tilde{Z} - \frac{19}{93}\eta\tilde{G}\tilde{Z}' + \frac{\tilde{G}\tilde{V}\tilde{Z}'}{2} + \tilde{G}\tilde{Z}\tilde{V}' = (\tilde{G}^{1/3}\tilde{Z}^{1/2}\tilde{Z}')'. \quad (2.47c)$$

As for the 2D case in Eqs. (2.22) we observe again that the change in the equation of state does not affect these equations and only the thermal conductivity term makes an appearance in the core scaling equations.

### 2.5.3 Numerical results

In our simulations, we have taken  $m = 4/5$  and  $M = 6/5$ . We verify the core scaling and bulk scaling from MD data in Figs. (2.7).

We solved the TvNS ODEs numerically, and we solved the NS equations following the method of [30, 31]. The plots comparing the two solutions are shown in Figs. (2.8a, 2.8b, 2.8c). We can see that the shock fronts predicted by the two solutions matches. Also there is a nice data collapse in the bulk for the NS solutions at two different times.

We solve Eqs. (2.47) (with boundary conditions taken from the NS data) and compare the resulting solution with the full numerical solution of the NS equations in Figs. (2.8d, 2.8e, 2.8f). We see that there is agreement in the core, and that there is data collapse in the core of the NS solutions at two different times.

While solving the NS equations, we take (following [30, 31]) heat conductivity  $\kappa = D_\kappa \rho^{1/3} T^{1/2}$ , with  $D_\kappa = 1$  and also a finite bulk viscosity  $\zeta = D_\zeta T^{1/2}$ , with  $D_\zeta = 1$  (setting this to zero does not change any of our conclusions). We also compared our NS numerical solution and TvNS solution with MD simulations (Fig. (2.9)) and find that the shock front position agrees quite well with that obtained from MD simulations. Near the core, there are some discrepancies, possibly due to anomalous heat conduction in 1D, or due to large deviations from local equilibrium (also observed for the case for point particles in [30, 31]).

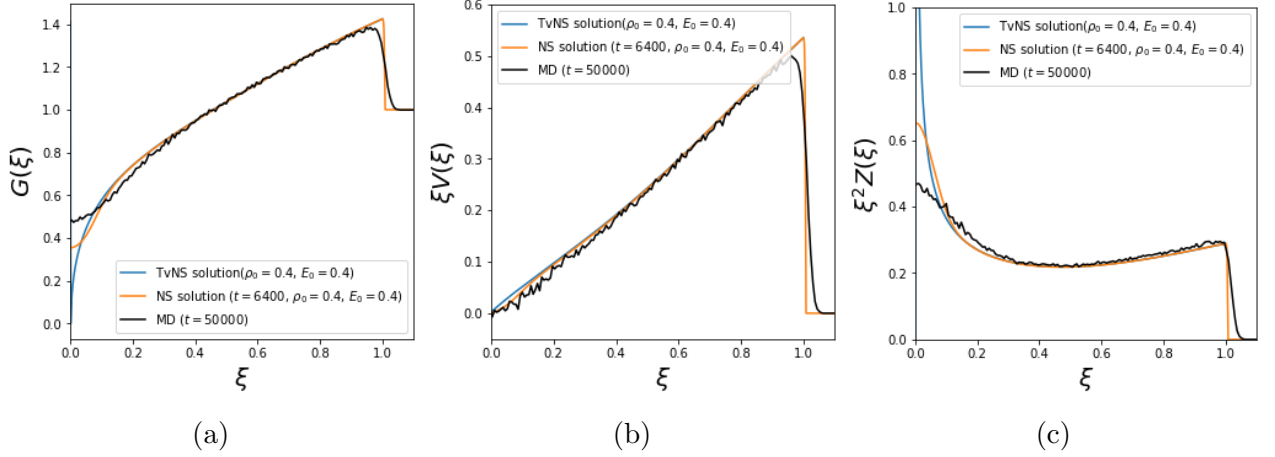


Figure 2.9: **Hard rods** Plot comparing the NS solution and TvNS solution with the MD simulations. We see that the shock front matches. We have taken  $\rho_\infty = 0.4$ ,  $E_0 = 0.4$ .

## 2.6 Hard point gas in $d$ –dimensions: Inner and outer solutions

In this section, we briefly discuss some features of the inner and outer solutions for the point particle gas in arbitrary dimensions. As in Sec. (3.4), we consider the limit of  $\rho_\infty \rightarrow \infty$  and  $a \rightarrow 0$  such that one has an ideal gas with finite transport coefficients. We first discuss the outer solution given by the TvNS-type analysis of the Euler equations. Then we discuss the inner solution where one has to write the full NS equations including dissipation terms.

### 2.6.1 Outer solution

#### Euler equations in $d$ –dimensions

From dimensional analysis we have in this case the shock front position  $R(t) = \left( \frac{E_0 t^2}{A_d \rho_\infty} \right)^{\frac{1}{d+2}}$ . Behind the shock,  $0 \leq r < R(t)$ , the radial velocity  $v(r, t)$ , density  $\rho(r, t)$  and pressure  $P(r, t)$  satisfy the Euler equations

$$\partial_t \rho + \partial_r(\rho v) + \frac{d-1}{r} \rho v = 0, \quad (2.48a)$$

$$(\partial_t + v \partial_r) \ln \frac{P}{\rho^\gamma} = 0, \quad (2.48b)$$

$$\rho(\partial_t + v \partial_r) v + \partial_r P = 0, \quad (2.48c)$$

where  $\gamma$  is the adiabatic index.

The velocity of the shock wave is

$$U = \frac{dR}{dt} = \delta \frac{R}{t}, \quad \delta \equiv \frac{2}{d+2}. \quad (2.49)$$

The Rankine-Hugoniot conditions [17] describing the jump of the hydrodynamic variables on both sides of the shock wave read

$$\frac{P(R)}{\rho_\infty U^2} = \frac{2}{\gamma+1}, \quad \frac{\rho(R)}{\rho_\infty} = \frac{\gamma+1}{\gamma-1}, \quad \frac{v(R)}{U} = \frac{2}{\gamma+1}, \quad (2.50)$$

in the case of the infinitely strong blast.

### Self-similar solution

Dimensional analysis assures that the hydrodynamic variables acquire a self-similar form

$$v = \delta \frac{r}{t} V, \quad \rho = \rho_\infty G, \quad c^2 = \delta^2 \frac{r^2}{t^2} Z. \quad (2.51)$$

Here  $c^2 = \gamma P/\rho = \gamma T$  is the square of the speed of sound and we have introduced constant factors of  $\delta$  and  $\delta^2$  in the definition of the scaling functions to simplify subsequent computations. The dimensionless quantities  $V, G, Z$  depend on the single variable

$$\xi = \frac{r}{R}. \quad (2.52)$$

One seeks the behavior of  $V(\xi), G(\xi)$  and  $Z(\xi)$  behind the shock wave,  $0 \leq \xi \leq 1$ . The Rankine-Hugoniot conditions Eqs. (2.50) become

$$V(1) = \frac{2}{\gamma+1}, \quad (2.53a)$$

$$G(1) = \frac{\gamma+1}{\gamma-1}, \quad (2.53b)$$

$$Z(1) = \frac{2\gamma(\gamma-1)}{(\gamma+1)^2}. \quad (2.53c)$$

Using energy conservation, one expresses  $Z$  through the scaled velocity  $V$  to give [17]:

$$Z = \frac{\gamma(\gamma-1)(1-V)V^2}{2(\gamma V-1)}. \quad (2.54)$$

Plugging the ansatz Eqs. (2.51-2.52) into Eq. (2.48a) gives

$$\frac{dV}{d\ell} + (V - 1) \frac{d \ln G}{d\ell} = -dV, \quad (2.55a)$$

where  $\ell = \ln \xi$ . Similarly we transform Eq. (2.48b) into

$$\frac{d \ln(Z/G^{\gamma-1})}{d\ell} = \frac{d + 2 - 2V}{V - 1}. \quad (2.55b)$$

Equations (2.55a-2.55b) can be solved for arbitrary  $d$  and  $\gamma > 1$ . Having solved the problem, one can compute the energy

$$\begin{aligned} E &= \int_0^R dr \, \Omega_d r^{d-1} \rho \left[ \frac{v^2}{2} + \frac{c^2}{\gamma(\gamma-1)} \right] \\ &= n_\infty \Omega_d \delta^2 \frac{R^{d+2-a}}{t^2} \int_0^1 d\xi \, \xi^{d+1} \frac{(\gamma-1)V^3}{2(\gamma V-1)} G. \end{aligned}$$

Here  $\Omega_d = 2\pi^{d/2}/\Gamma(d/2)$  is the surface area of the unit sphere and we have used Eq. (2.54). Substituting Eq. (2.1) into the above expression for the energy we fix the dimensionless constant  $A_d$ :

$$A_d(\gamma) = \Omega_d \delta^2 \frac{\gamma-1}{2} \int_0^1 d\xi \, \xi^{d+1} \frac{V^3}{\gamma V-1} G. \quad (2.56)$$

In the following we limit ourselves to a monoatomic gas where  $\gamma = 1 + 2/d$ . The adiabatic index generally depends only on the spatial dimension and independent of the interaction between particles [49, 50]. The monoatomic gases are relevant in astrophysics where even diatomic molecules are extremely rare. For the monoatomic gas, the Rankine-Hugoniot conditions Eqs. (2.53a-2.53c) become

$$V(1) = \frac{d}{d+1}, \quad G(1) = d+1, \quad Z(1) = \frac{d+2}{(d+1)^2}, \quad (2.57)$$

and Eq. (2.54) reduces to

$$Z = \frac{(1+2/d)(1-V)V^2}{(d+2)V-d}. \quad (2.58)$$

Using Eq. (2.55a) and Eq. (2.55b) with  $\gamma = 1 + 2/d$  and  $Z$  given by Eq. (2.58) we express  $dV/d\ell$  and  $d(\ln G)/d\ell$  through the scaled velocity  $V$ :

$$\frac{dV}{d\ell} = V \frac{X}{2D}, \quad (2.59a)$$

$$\frac{d \ln G}{d\ell} = \frac{V}{V-1} \frac{Y}{2D}, \quad (2.59b)$$

where we write in short

$$\begin{aligned} X &= [(d+2)V - d](d+2 - 4V), \\ D &= d - 2(d+1)V + (d+1)(1 + 2/d)V^2, \\ Y &= (2-d)d + (d-2)(2+3d)V + 2(d+2)(1-d)V^2. \end{aligned}$$

Integrating Eq. (2.59a) yields an implicit solution for the scaled velocity

$$\xi = c_d [(d+2)V - d]^{\frac{2}{d^2+4}} V^{-\frac{2}{d+2}} (d+2 - 4V)^{-\lambda_d}, \quad (2.60)$$

with

$$\begin{aligned} c_d &= \left( \frac{d}{d+1} \right)^{\frac{2}{d+2} - \frac{2}{d^2+4}} \left( \frac{d^2 - d + 2}{d+1} \right)^{\lambda_d}, \\ \lambda_d &= \frac{8 + 4d + 10d^2 - d^3 + d^4}{2d(2+d)(4+d^2)}. \end{aligned} \quad (2.61)$$

We then divide Eq. (2.59b) by Eq. (2.59a) and integrate in  $V$  to give

$$G = C_d [(d+2)V - d]^{\frac{d^2}{d^2+4}} (1-V)^{-\frac{2d}{d-2}} (d+2 - 4V)^{\Lambda_d}, \quad (2.62)$$

with

$$\begin{aligned} C_d &= (d+1)^{\frac{d^2}{d^2+4} - \frac{2d}{d-2}} d^{-\frac{d^2}{d^2+4}} \left( \frac{d^2 - d + 2}{d+1} \right)^{-\Lambda_d}, \\ \Lambda_d &= \frac{8 + 4d + 10d^2 - d^3 + d^4}{2(d-2)(4+d^2)}. \end{aligned} \quad (2.63)$$

Finally,  $Z = Z(V)$  is given by Eq. (2.58).

### Singular behavior

Using Eq. (2.60) and Eq. (2.62), one extracts the asymptotic behaviors near the center of the explosion ( $\xi \ll 1$ ):

$$G \sim \xi^{\frac{d^2}{2}}, \quad Z^{-1} \sim V - \frac{d}{d+2} \sim \xi^{\frac{d^2+4}{2}}. \quad (2.64)$$

In terms of the original coordinates

$$\rho \sim r^{\frac{d^2}{2}} t^{-\frac{d^2}{d+2}}, \quad T \sim r^{-\frac{d^2}{2}} t^{\frac{d(d-2)}{d+2}}. \quad (2.65)$$

This physically dubious behavior (the density vanishes, while the temperature diverges at  $r = 0$ ) indicates that the framework we have employed so far becomes incomplete near the center of the explosion. We rectify it by including dissipation.

## 2.6.2 Inner solution

### Navier-Stokes equations

Here we are considering the hard-point gas in the Boltzmann-Grad limit. Notice however that, even if we were to take the model of hard sphere gas to ensure that there are collisions, our core analysis would not change. This would mean virial corrections in the equation of state and corrections to the transport coefficients. However, since the core is a region of low density, these corrections are negligible, and the core equations would be the same as that of an ideal gas.

The continuity equation is not affected by dissipative processes [17]. Thus for our radial flow Eq. (2.48a) remains valid. The momentum equation is generally affected by viscosity—adding an extra term  $\nabla \cdot \boldsymbol{\sigma}$  to the Euler equation yields the Navier-Stokes equation. The viscous stress tensor is given by

$$\boldsymbol{\sigma} = \mu [\nabla \mathbf{v} + (\nabla \mathbf{v})^T - \frac{2}{d}(\nabla \cdot \mathbf{v})\mathbf{I}] + \zeta(\nabla \cdot \mathbf{v})\mathbf{I},$$

where  $\mathbf{I}$  is the unit tensor and the coefficients of shear and bulk viscosity are denoted by  $\mu$  and  $\zeta$ . Little is known about bulk viscosity. Fortunately, for dilute monoatomic gases the coefficient of bulk viscosity vanishes [49]. Thus for the dilute hard sphere (HS) gas

$$\boldsymbol{\sigma} = \mu [\nabla \mathbf{v} + (\nabla \mathbf{v})^T - \frac{2}{d}(\nabla \cdot \mathbf{v})\mathbf{I}]. \quad (2.66)$$

According to kinetic theory [49, 50], transport coefficients exhibit similar behavior. For the dilute HS gas, these coefficients are proportional to  $\sqrt{T}$ . This is the classical prediction of kinetic theory. More precisely, the coefficient of shear viscosity for the dilute hard sphere (HS) gas reads

$$\mu = M_d a^{-(d-1)} \sqrt{mT}, \quad (2.67)$$

where  $m$  and  $a$  denote spheres' masses and radii. The dimensionless amplitude  $M_3$  is known only approximately [49, 50]. The coefficient of thermal conductivity for the dilute HS gas is given by a similar formula

$$\kappa = K_d a^{-(d-1)} \sqrt{mT}, \quad (2.68)$$

which differs from the expression Eq. (2.67) only by the dimensionless amplitude,  $K_d$  instead of  $M_d$ .

The entropy equation is affected by heat conduction and viscous dissipation. To estimate the size of the core region where dissipative effects matter it suffices to keep heat conduction and ignore viscous dissipation. In this situation Eq. (2.48b) is replaced by equation

$$\rho T (\partial_t + v \partial_r) s = r^{-(d-1)} \partial_r (r^{d-1} \kappa \partial_r T), \quad (2.69)$$

for the entropy per unit mass

$$s = \frac{d}{2} \ln \left( \frac{T}{\rho^{2/d}} \right). \quad (2.70)$$

Using Eqs. (2.70)-(2.68) we recast Eq. (2.69) into

$$\rho^{1+2/d} (\partial_t + v \partial_r) \frac{T}{\rho^{2/d}} = \frac{1}{r^{d-1}} \partial_r (r^{d-1} T^{1/2} \partial_r T). \quad (2.71)$$

We have set  $K_d a^{-(d-1)} \sqrt{m} = 1$  in Eq. (2.71) to avoid cluttering the formulas; this factor can be always restored in the final results on dimensional grounds.

## Heuristic analysis for core scaling

Using (2.71) we deduce an estimate

$$\rho \frac{T}{t} \sim \frac{T^{3/2}}{r^2}, \quad (2.72)$$

which is combined with (2.65) to give an estimate of the growth of the radius  $X$  of the core where the heat transfer plays significant role

$$X \propto R^{h_d}, \quad h_d = \frac{4 + 3d^2}{8 + 3d^2}. \quad (2.73)$$

According to Eq. (2.65), the density vanishes and the temperature diverges at the center of the explosion. Heat conduction rectifies these predictions. Indeed, instead of using Eq. (2.65) at  $r = 0$ , one should substitute  $r = X$  into Eq. (2.65). This allows us to estimate the density, temperature and pressure in the core region including the center of the explosion

$$\rho^* \propto R^{-\nu_d}, \quad T^* \propto R^{-(d-\nu_d)}, \quad p^* \propto R^{-d}, \quad (2.74)$$

with  $\nu_d = 2d^2/(8 + 3d^2)$ .



## 2.7 Discussion

In this chapter, we presented the results of numerical solutions of the Navier-Stokes (NS) equations of dissipative hydrodynamics for a 2D hard-disc gas, a 2D hard point gas, and a 1D hard-rod gas. We revealed that the long-time solution has a double scaling form — it consists of an outer solution described by the well-known TvNS scaling form, and an inner solution described by different scaling functions. For the 2D gas, the inner solution is valid in the region  $0 < r \lesssim t^{2/5}$  while the outer solution is valid in the region  $t^{2/5} \lesssim r < R(t)$ , with  $R(t) \sim t^{1/2}$  known quite precisely. The inner solution arises due to the dominance of dissipative terms (namely, the viscosity and thermal conductivity terms in the NS equations) in the core of the blast.

We also pointed out that molecular dynamics (MD) simulation data for both the 1D and 2D gases agree with the results from the solution of NS equations, except in the core. The MD data does satisfy the scaling forms corresponding to the inner and outer scaling solutions, however, the scaling functions differ. This mismatch in the core occurs also for 1D point particles [30, 31] and a possible reason could be that transport coefficients are anomalous in low dimensional systems.

In the alternating mass point-particle gas studied in [31], the equation of state is that of an ideal gas, whereas in the alternating mass hard-rod gas it departs from the ideal-gas law. In contrast to hard spheres in two and three dimensions—where only virial expansions of the equation of state are known—the equation of state for hard rods in one dimension can be written down exactly. Another important difference is that for the point-particle gas one can obtain an exact solution of the Euler equations for the blast problem; this is not possible for the hard-rod gas because its equation of state is non-ideal.

Note that the ratio of the size of the core to the size of the blast  $X(t)/R(t)$  in 1D ( $t^{38/93}/t^{2/3} \sim t^{-24/93}$  [30, 31]) is much smaller than in 2D ( $t^{2/5}/t^{1/2} \sim t^{-1/10}$ ). This ratio is even larger in 3D ( $t^{62/175}/t^{2/5}$ ). Despite the ratio being larger in 2D than in 1D, we find that dissipative corrections in the core do not affect the position of the shock front in 2D. In general  $d$ -dimensions ( $d \geq 2$ ), the shock front position,  $R(t)$ , and the core size,  $X(t)$ , grow as [see Sec. (2.6) for the details of the derivation]:

$$R(t) \sim t^{\frac{2}{(d+2)}}, \quad X(t) \sim t^{\frac{2(4+3d^2)}{(d+2)(8+3d^2)}}. \quad (2.75)$$

We present below a table showing the size of the shock front and the core, the hydrodynamic fields in the core and the ratio of the core energy ( $E^*$ ) to the total energy in 2D

and 3D [the details of the derivation are given in Sec. (2.6)].

$d$	$R$	$X$	$\rho^*$	$T^*$	$p^*$	$v^*$	$E^*/E_0$
2	$t^{1/2}$	$t^{2/5}$	$t^{-1/5}$	$t^{-4/5}$	$t^{-1}$	$t^{-3/5}$	$t^{-1/5}$
3	$t^{2/5}$	$t^{62/175}$	$t^{-36/175}$	$t^{-174/175}$	$t^{-6/5}$	$t^{-113/175}$	$t^{-24/175}$

The core is the region where deviations from local equilibrium are large (see also [39]), and treating the deviation as a first order approximation (which is what is done in the NS framework) may not suffice. Apart from this, there is the issue of long time tails of correlation functions and the divergence of transport coefficients in dimensions  $d \leq 2$  [51, 43, 34, 52]. This can be also be a reason for the mismatch between hydrodynamics and microscopic simulations observed in the core. Finally, another reason for the failure of hydrodynamics in the core could be the fact that the Knudsen number (which is the ratio of the mean free path to the length scale of variation of the hydrodynamic fields) in the core for the 2D case has a very slow decay than that in the bulk. In the core, the Knudsen number is  $\sim \rho^{*-1} t^{-2/5} \sim t^{-1/5}$ , while that in the bulk is  $\sim \rho_\infty^{-1} t^{-1/2} \sim t^{-1/2}$ . This reason is connected to the reason mentioned before, as the Knudsen number is a measure of the deviation from local equilibrium and how well the hydrodynamic limit is reached.

Interesting open problems would be to resolve the observed disagreement between hydrodynamics and microscopic dynamics in the core for the blast problem, and to see if this disagreement disappears in higher dimensions.

# Chapter 3

## Interacting Integrable system

*"The miracle of the appropriateness of the language of mathematics for the formulation of the laws of physics is a wonderful gift which we neither understand nor deserve."*

**-Eugene Wigner**

A classical Hamiltonian many-body system will generally thermalize at long times in the sense that macroscopic observables can be described by the Gibbs Ensemble (GE). However, there may exist systems that do not thermalize to GE, because of the existence of macroscopic number of extra conservation laws which restrict their motion in the phase space. Such systems are often known as integrable many-body systems, which are believed to thermalize to the Generalized Gibbs Ensemble (GGE) [53, 54, 55, 56]. They have been realized experimentally in one-dimensional trapped atoms [57, 58]. Their non-equilibrium dynamics close to local GGE is described by generalised hydrodynamics (GHD) [9, 59, 60, 4, 10]. Integrable systems are very fine-tuned systems in the sense that the smallest of perturbations (which are always present in any experimental setup) can break integrability. However, in the presence of integrability breaking perturbations, it is expected that the system will still remain integrable for short times [57, 58, 61, 62], and so integrable dynamics may still play an important role. Integrable systems are also important from the point of view of studying exact dynamics of systems far from equilibrium. Since they rekindle the hope of obtaining exact solutions to many-body systems out of equilibrium, it is possible to use them to study far from equilibrium states, which cannot be treated using hydrodynamics (for non-integrable case) or generalised hydrodynamics (for integrable case) because hydrodynamics (HD) can only handle states near local equilibrium (or local GGE).

It is useful to make a distinction between interacting and non-interacting integrable systems [63]. In non-interacting integrable systems, the quasiparticles move in straight

lines at constant velocity. For example, in one dimensional hard point particle gas, the collisions happen at a point and two particles simply exchange velocity after colliding, and thus the system can be mapped to non-interacting one by interchanging the labels of the two colliding particles after the collision. In the mapped non-interacting problem, the new particles moving with a fixed velocity are called quasi-particles, and they move in straight lines at constant velocities, like in a non-interacting gas. This is not the case for interacting integrable systems. In the hard rod case, a quasiparticle will have a straight line motion interrupted by sudden jumps (of the size of rod length) owing to the collisions. This effectively leads to dissipation in the hydrodynamics of the hard-rod gas, which can get manifested by the spreading of a tagged quasiparticle. On the other hand, for the point particle case, the system has no dissipation term in its hydrodynamics and consequently no spreading in the position of a tagged quasiparticle. Such spreading was studied, from microscopic calculations, by Lebowitz, Percus and Sykes [64] and demonstrated the effect of dissipation. Such dissipation terms appearing as Navier-Stokes (NS) corrections to the HD equation of hard rods was later established by Spohn [65], Boldrighini and Suhov [8] and recently discussed by Doyon and Spohn [66] and Ferrari and Olla [67]. Due to the presence of the dissipation term, one generally expects that the hard-rod gas would approach to a GGE state starting from a non-equilibrium initial condition.

The question of approach to the GGE state in integrable systems has been widely discussed in the quantum context [53, 68, 69, 70] and the effect of dissipation was demonstrated in the context of evolution of a domain wall in the quantum Heisenberg spin chain [71]. However, to the best of our knowledge, this has not been observed for classically integrable systems. Neither has the effect of the Navier-Stokes correction to the Euler GHD solutions been demonstrated in any study. In the context of the classical system of hard rods, the questions on evolution and effect of dissipation were addressed in [66] for the specific case of domain wall initial condition. This study demonstrated that the evolution from such initial condition can be very well accurately described by the solution of the Euler GHD equations. Although the corrections from the Navier-Stokes terms were discussed in [66], this could not be unambiguously established from the numerics. The aims of this work are: (i) to study the evolution of non-equilibrium initial states and see if they approach GGE at large times; (ii) to demonstrate the effect of dissipation in such an evolution.

This chapter is organized as follows. In Sec. (3.1) we define the model and the different initial conditions used in the study, and summarize the main results in Sec. (3.2). In Sec. (3.3), we define hydrodynamics of the hard-rod gas and explain how the Euler equation can be solved. We investigate the equilibration and the effect of dissipation in Sec. (3.4) by comparing the predictions of hydrodynamics with those of MD simulations

for different initial conditions. In Sec. (3.5) we provide discussions of our results and conclude. Some details of the calculations are provided in the appendix.

### 3.1 Model, observables and initial conditions

We consider a system of  $N$  hard rods each of length  $a$  and unit mass, moving inside a one dimensional box of size  $L$ . The rods move with constant velocity in between collisions. Two rods exchange their velocities at collisions with each other whereas at collisions with the walls at  $x = 0$  and  $x = L$  the rods flip their velocities. This implies reflecting boundary conditions at  $x = 0$  and  $x = L$ . This model with  $a \neq 0$  is an example of an interacting integrable system, while for  $a = 0$ , it becomes non-interacting integrable system.

The microscopic dynamics of hard rods can be mapped to that of hard point particles as follows [6, 5, 64]: Let  $x_i$ ,  $i = 1, 2, \dots, N$  denote the ordered positions ( $x_i < x_{i+1} - a$  with  $x_1 > a/2$  and  $x_N < L - a/2$ ) and  $v_i$ ,  $i = 1, 2, \dots, N$  denote velocities of the rods. For each microscopic configuration  $\{x_i, v_i\}$  of hard rods, one can construct a configuration  $\{x'_i, v'_i\}$  of hard point particles by removing the inaccessible spaces between rods and, between rods and the walls. More precisely the mapping can be written as

$$x'_i = x_i - (i - 1/2)a, \quad v'_i = v_i \quad i = 1, 2, \dots, N, \quad (3.1)$$

and consequently one has a set of hard point particles moving inside a box of length  $L' = L - Na$ . The dynamics of hard point particles can be further mapped to non-interacting point particles by the Jepsen mapping [72]. This mapping has earlier been used to find several analytical results, such as quasiparticle distribution [64], free expansion problem [5] and sound and shock propagation [6]. This mapping also allows one to simulate the hard rod dynamics efficiently and accurately. Throughout this paper, we represent configurations of the point particles by primed variables ( $\{x'_i, v'_i\}$ ) and those of the rods by un-primed variables ( $\{x_i, v_i\}$ ).

In this paper we study the evolution of the single particle phase space distribution,  $f(x, v, t)$ , of the hard rods defined as

$$f(x, v, t) = \left\langle \sum_{i=1}^N \delta(x - x_i) \delta(v - v_i) \right\rangle, \quad (3.2)$$

where  $\langle \dots \rangle$  denotes an average over the ensemble of initial conditions corresponding to fixed forms of the initial density profile and single particle velocity distribution. We

investigate the possible approach to GGE and the effect of NS terms, for the following three different initial conditions:

- A The particles on each of the two halves,  $(0, L/2)$  and  $(L/2, L)$ , are separately distributed uniformly at a finite density  $\rho_0 = N/L$ . We assign all particles on the left half  $[x \in (0, L/2)]$  with velocity  $v_0 (= 1)$ , while the velocities of all particles on the right half  $[x \in (L/2, L)]$  are chosen from a Maxwell distribution with temperature  $T = 1$

$$h(v) = \frac{1}{\sqrt{2\pi}} \exp\left(-\frac{v^2}{2}\right), \quad \text{for } -\infty \leq v \leq \infty. \quad (3.3)$$

In this initial condition, one has two components of the gas – for the first component, each particle has velocity  $v_0 = 1$ , while in the second (which we call the background particles), the particles have velocity distributed according to  $h(v)$ .

- B Next we consider an initial condition where we first place a particle with a given velocity  $v_0 (= 1)$  at the origin. The rest of the box is then filled with particles distributed uniformly in space with a density  $\rho_0 = N/L$ . These background particles have velocities chosen from the Maxwell velocity distribution  $h(v)$ . This case is more analytically tractable than the previous case in (A) and was first studied by Lebowitz, Percus, Sykes (LPS) in [64]. In this case, the initial single particle phase space distribution has the form  $f(x, v, t = 0) = \delta(x)\delta(v - v_0) + \rho_0 h(v)$ .

- C Finally we consider the set-up of free expansion from a half filled box. In this case the rods are uniformly distributed in the left half of the box at a constant density,  $2\rho_0$ , and the velocities are again chosen from the Maxwell distribution,  $h(v)$ . The right half of the box is empty. This problem of free expansion was previously investigated in [5], where the evolution of various hydrodynamic variables was computed using a microscopic approach and with certain approximations that effectively amount to solving the Euler equations. For both the classical and quantum cases, the free expansion problem for point particles has recently been studied in the context of entropy growth [30, 73, 74].

For the three initial conditions mentioned above, we study the evolution of the density profile,  $\rho(x, t)$ , and the velocity profile,  $u(x, t)$  (or equivalently, the momentum density

profile  $p(x, t) = \rho(x, t)u(x, t)$ , defined as

$$\rho(x, t) = \int f(x, v, t)dv, \quad (3.4a)$$

$$u(x, t) = \frac{1}{\rho} \int v f(x, v, t)dv. \quad (3.4b)$$

We investigate the effect of dissipation by comparing the profiles obtained from simulation with those predicted from the solution of Euler GHD. We also check if the system reaches GGE at long times. A simple test for GGE would be to check if the density and velocity profiles become time stationary, *i.e.*, independent of time and uniform in space. Note that the velocity distribution is invariant under the integrable dynamics and specifies the GGE.

## 3.2 Results

We summarize here our main results:

- For initial condition (A), we find that the predictions for the evolution of the densities, from the solution of the Euler GHD, describe the profiles obtained from numerical simulations quite well almost everywhere except at the locations of the shocks where we observe clear discrepancies. These discrepancies appear due to the effect of dissipation described by the NS term. This leads to the width  $w(t)$  of the shock growing as  $w(t) \sim \sqrt{t}$  at early times, and saturating to a value  $w(t \rightarrow \infty) \sim \sqrt{N}$  at large times. Thus the initial density of either of the components ( $v_0 = 1$  and the thermal ones) never become homogeneous over the full system and each of the two components move inside the box with a constant effective speed  $v_{\text{eff}}$  (see Eq. (3.38)) at large times. Hence the system never reaches GGE.
- This spreading is more prominent in the case of initial condition (B). For this case we provide an analytical understanding of the spreading based on the solution of the NS equation. In this case also the system never reaches GGE.
- For the case (C) of free expansion we find that the evolution of the density and momentum density profiles is completely described by Euler GHD and, since the discontinuity in the initial density profile disappears already at very early times, any effects of the NS corrections are too small to be observed. In this case, the system at long times evolves to a state consistent with GGE.

### 3.3 Hydrodynamic equations for hard rods and solution of the Euler equation

The hydrodynamic equation for the single particle phase space distribution  $f(x, v, t)$  for the hard-rod gas is given by [66]:

$$\partial_t f(x, v, t) + \partial_x (v_{\text{eff}}(x, v, t) f(x, v, t)) = \partial_x \mathcal{N}(x, v, t), \quad \text{where} \quad (3.5a)$$

$$v_{\text{eff}}(x, v, t) = \frac{v - a\rho(x, t)u(x, t)}{1 - a\rho(x, t)}, \quad (3.5b)$$

$$\mathcal{N}(x, v, t) = \frac{a^2}{2(1 - a\rho(x, t))} \int dw |v - w| (f(x, w, t) \partial_x f(x, v, t) - f(x, v, t) \partial_x f(x, w, t)) \quad (3.5c)$$

and  $\rho(x, t)$ ,  $u(x, t)$  are given in Eq. (3.4a) and (3.4b). The term  $\partial_x \mathcal{N}$  represents the NS correction to the Euler equations [66, 8].

We now discuss the solution of the Euler equation

$$\partial_t f + \partial_x (v_{\text{eff}} f) = 0, \quad (3.6)$$

for general initial condition. As shown previously [5, 6], the Euler equation for hard rods can be solved exactly for general initial conditions by mapping it to a non-interacting point particle problem. For completeness, we show below how the mapping to the non-interacting Euler equation can be obtained using the GHD approach. For this one defines a new function,

$$f^0(x', v, t) = \frac{f(x, v, t)}{1 - a\rho(x, t)}, \quad (3.7)$$

where

$$x' = x - aF(x, t), \quad F(x, t) = \int_B^x \rho(y, t) dy, \quad (3.8)$$

and  $B$  is the position of the left end of the container in which the hard rod fluid is contained. Note that  $F(x, t)$  is the cumulative density corresponding to  $\rho(x, t)$ . We observe that

$$f^0(x', v, t) dx' dv = f(x, v, t) dx dv, \quad (3.9)$$

which implies that  $f^0(x', v, t)$  is also a phase space distribution function. We now show that  $f^0(x', v, t)$  satisfies the Liouville equation of free ballistic particles and hence describes the single particle phase space distribution of the point particles. The first step



towards this demonstration [4] is to define the function

$$f_n(x, v, t) = \frac{f(x, v, t)}{1 - a\rho(x, t)}. \quad (3.10)$$

Using Eq. (3.6) and the relation  $\partial_t \rho = -\partial_x(\rho u)$  [for the fields defined in Eqs. (3.4a, 3.4b)], it readily follows that

$$\partial_t f_n + v_{\text{eff}} \partial_x f_n = 0. \quad (3.11)$$

Now, from Eq. (3.7), we have

$$f_n(x, v, t) = f^0(x - aF(x, t), v, t). \quad (3.12)$$

Taking the time derivative with respect to  $t$  on both sides of Eq. (3.12) and using  $\partial_t F(x, t) + \rho u = 0$  one finds

$$\partial_t f_n(x, v, t) = \partial_t f^0(x', v, t) + a\rho(x, t)u(x, t)\partial_{x'} f^0(x', v, t). \quad (3.13)$$

On the other hand taking derivative with respect to  $x$  on both sides of Eq. (3.12) one has

$$\partial_x f_n(x, v, t) = (1 - a\rho)\partial_{x'} f^0(x', v, t). \quad (3.14)$$

Inserting the forms from Eq. (3.13) and Eq. (3.14) in Eq. (3.11), one finds that the phase space distribution function  $f^0(x', v, t)$  satisfies the Liouville equation for the non-interacting particles

$$\partial_t f^0 + v\partial_{x'} f^0 = 0. \quad (3.15)$$

This equation can be easily solved for arbitrary time and any initial condition  $f^0(x', v, 0)$ . For example on the infinite line one has  $f^0(x', v, t) = f^0(x' - vt, v, 0)$  while in the box one has to solve the single particle problem with repeated collisions with the walls [5, 30]. From  $f^0(x', v, t)$  one can find the solution for the phase space distribution  $f(x, v, t)$  of hard rods. To get the solution explicitly, we first note from Eq. (3.7) that

$$\rho(x, t) = \frac{\rho^0(x', t)}{1 + a\rho^0(x', t)}, \quad \text{where } \rho^0(x', t) = \int dv f^0(x', v, t). \quad (3.16)$$

Hence inverting Eq. (3.7) and using Eq. (3.16), one finds

$$f(x, v, t) = \frac{f^0(x', v, t)}{1 + a\rho^0(x', t)}. \quad (3.17)$$

The variable transformation  $x \rightarrow x'$  can be inverted as

$$x = x' + aF^0(x', t), \quad (3.18)$$

using  $F(x, t) = F^0(x', t)$  which can be shown easily from Eq. (3.9).

While, as demonstrated above, the Euler equation can be solved exactly, it is difficult to solve the NS equation (3.5b) for arbitrary initial conditions. We expect that the difference between the solutions of the Euler and the NS equations are large at places where the spatial derivative of the Euler solution is large.

## 3.4 Results from numerical simulations for the three initial conditions

### 3.4.1 Initial condition A

In this case the initial condition can be written explicitly as

$$f(x, v, 0) = g(x, 0)\delta(v - 1) + f_b(x, v, 0), \quad \text{with} \quad f_b(x, v, 0) = \rho_b(x, 0)h(v), \quad \text{for} \quad \frac{a}{2} \leq x \leq L - \frac{a}{2}, \quad (3.19)$$

where  $h(v)$  is given in Eq. (3.3) and

$$g(x, 0) = \rho_0 \Theta(x - a/2)\Theta(L/2 - x) \quad (3.20)$$

$$\rho_b(x, 0) = \rho_0 \Theta(x - L/2)\Theta(L - a/2 - x), \quad (3.21)$$

with  $\rho_0 = \frac{N}{L-a}$  and  $\Theta(x)$  being Heaviside theta function. Note that we will be working in the thermodynamic limit  $N \rightarrow \infty$   $L \rightarrow \infty$  such that  $N/L \rightarrow \rho_0$ .

As discussed in the previous section, solution to the Euler equation can be obtained by mapping to point particles. It is easy to show that initial phase space density  $f^0(x', v, 0)$  also has two components, the special component with velocity  $v = 1$  and the background particles having velocity distributed according to Maxwell distribution. It is given explicitly as

$$f^0(x', v, 0) = g^0(x', 0)\delta(v - 1) + f_b^0(x, v, 0), \quad \text{with} \quad f_b^0(x, v, 0) = \rho_b^0(x, 0)h(v), \quad \text{for} \quad 0 \leq x' \leq L', \quad (3.22)$$

where  $L' = L - Na$  and

$$g^0(x', 0) = \frac{\rho_0}{1 - a\rho_0} \Theta(x')\Theta(L'/2 - x') \quad (3.23)$$

$$\rho_b^0(x', 0) = \frac{\rho_0}{1 - a\rho_0} \Theta(x' - L'/2)\Theta(L' - x'). \quad (3.24)$$

The evolution of  $f^0$  for any arbitrary initial distribution  $f^0(x', v, 0) = \varrho(x')p(v)$  is given by [see Appendix A of [\[30\]](#)]

$$f^0(x', v, t) = \int_0^{L'} dy \varrho(y) \int_{-\infty}^{\infty} du p(u) \sum_{n=-\infty}^{\infty} [\delta(x' - y - ut + 2nL')\delta(v - u) + \delta(x' + y + ut - 2nL')\delta(v + u)], \quad (3.25)$$

Since the Euler Equation [\(3.15\)](#) for point particles is linear, the distribution  $f^0(x', v, t)$  at time  $t$  still can be written as a sum of two components as

$$f^0(x', v, t) = g^0(x', t)\delta(v - 1) + f_b^0(x', v, t). \quad (3.26)$$

The first term in this expression can be obtained by putting  $\varrho(y) = g^0(y, 0)$  and  $p(u) = \delta(u - 1)$  and performing the integration over  $v$ , yielding

$$g^0(x', t) = \frac{\rho_0}{1 - a\rho_0} \sum_{n=-\infty}^{\infty} (\Theta(x' - t + 2nL') - \Theta(x' - t + 2nL' - L'/2) + \Theta(-x' - t + 2nL') - \Theta(-x' - t + 2nL' - L'/2)), \quad (3.27)$$

where, recall  $L' = L - Na$ . For the background component we set  $\varrho(y) = \rho_b^0(y, 0)$  and  $p(u) = h(u)$  to get:

$$\begin{aligned} \rho_b^0(x', t) &= \int_{-\infty}^{\infty} dv f_b^0(x', v, t), \\ &= \frac{\rho_0}{1 - a\rho_0} \frac{1}{\sqrt{2\pi T}} \sum_{n=-\infty}^{\infty} \int_{L'/2}^{L'} dy \int_{-\infty}^{\infty} dv e^{-v^2/2T} [\delta(x - y - vt + 2nL) + \delta(x + y - vt - 2nL)], \\ &= \frac{\rho_0}{1 - a\rho_0} \frac{1}{\sqrt{2\pi T}} \sum_{n=-\infty}^{\infty} \int_{L'/2}^{L'} dy \frac{1}{t} \left[ \exp \left\{ \frac{-(2nL' + x - y)^2}{2Tt^2} \right\} + \exp \left\{ \frac{-(2nL' - x - y)^2}{2Tt^2} \right\} \right], \\ &= \frac{\rho_0}{2(1 - a\rho_0)} \sum_{n=-\infty}^{\infty} \left[ \operatorname{erf} \left( \frac{x + L'/2 + (2n - 1)L'}{\sqrt{2T}t} \right) - \operatorname{erf} \left( \frac{x - L'/2 + (2n - 1)L'}{\sqrt{2T}t} \right) \right]. \end{aligned} \quad (3.28)$$

$$= \frac{\rho_0}{2(1 - a\rho_0)} \sum_{n=-\infty}^{\infty} \left[ \operatorname{erf} \left( \frac{x - L'/2 + 2nL'}{\sqrt{2T}t} \right) - \operatorname{erf} \left( \frac{x + L'/2 + 2nL'}{\sqrt{2T}t} \right) \right]. \quad (3.29)$$

Using the Poisson resummation formula, this can be rewritten in the alternative series

form:

$$\rho_b^0(x', t) = \frac{\rho_0}{2(1 - a\rho_0)} + \frac{2\rho_0}{(1 - a\rho_0)} \sum_{k=1}^{\infty} \frac{1}{\pi k} \cos\left(\frac{k\pi(L' - x)}{L'}\right) \sin \frac{k\pi}{2} e^{-\frac{\pi^2 k^2 t^2}{2L'^2}}. \quad (3.30)$$

Note that shifting the origin to  $L'/2$  (i.e.,  $x' \rightarrow z' = x' - L'/2$ ) and taking  $L' \rightarrow \infty$ , one obtains the solution of Euler GHD on the infinite line as

$$\begin{aligned} g^0(z', t) &= \frac{\rho_0}{1 - a\rho_0} \Theta(z' - t), \\ \rho_b^0(z', t) &= \frac{\rho_0}{2(1 - a\rho_0)} \left[ 1 + \operatorname{erf}\left(\frac{z'}{\sqrt{2Tt}}\right) \right], \end{aligned} \quad (3.31)$$

where  $T = 1$ . The corresponding densities of the hard rods for the two components, respectively  $g(x, t)$  and  $\rho_b(x, t)$ , can be obtained using the inverse mapping Eq. 3.16 and Eq. 3.18 along with  $\rho^0(x', t) = g^0(x', t) + \rho_b^0(x', t)$ . We show in Fig. 3.1 the evolution of  $g(x, t)$  and  $\rho_b(x, t)$  obtained from the solutions of the Euler GHD equation as well as the results from direct MD simulations.

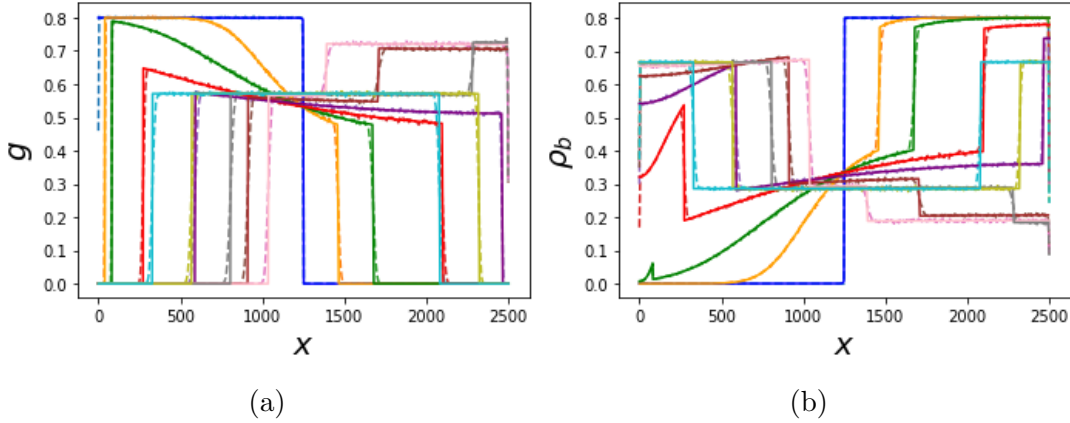


**Figure 3.1: Comparing solution of Euler equation with MD simulation for initial condition A:** Plot comparing the solution of the Euler equation with those of molecular dynamics for (a) the density of  $v = 1$  particles, denoted by  $g(x)$  and (b) the density of background particles, denoted by  $\rho_b(x)$ . Dashed lines are MD simulations and solid lines are solutions of Euler equation. We have taken times  $t = 0$  (dark blue),  $t = 40$  (orange),  $t = 80$  (green),  $t = 160$  (red),  $t = 240$  (violet),  $t = 320$  (brown),  $t = 400$  (pink),  $t = 480$  (grey),  $t = 560$  (mud green) and  $t = 640$  (cyan). We see that even for very long time like  $t = 640$ , the profile obtained from MD does not relax to GGE, i.e., it does not become uniform. We also see that there is a discrepancy between MD and Euler solutions at the shock front due to dissipative effects. We have taken length of the box  $L = 2500$ , total number of particles  $N = 2000$  and length of rod  $a = 1.0$ . We have performed ensemble averaging over 5000 realizations while doing MD.

For the solutions of the Euler GHD, we make the following observations:

- a. There is always a shock at the front of the density profiles for both the components. On the infinite line, the shocks for the two components move in opposite directions. Note that the density profiles  $g^0(x', t)$  and  $\rho^0(x', t)$  in the point particle gas evolve independently of each other. Consequently,  $g^0(x', t)$  will move with constant speed  $v_0 = 1$  keeping the initial shape unchanged, *i.e.*, with two discontinuities at  $L/2$  separation. Hence the total density,  $\rho^0(x', t) = g^0(x', t) + \rho_b^0(x', t)$  will also have discontinuities. Consequently, the density profiles  $g(x, t)$  and  $\rho(x, t)$  of the hard rods, obtained through the transformation in Eq. (3.16) also exhibits discontinuities, *i.e.*, shocks.
- b. At early times the evolution of these density profiles correspond to that on an infinite line and can be described by  $g(x, t)$  and  $\rho_b(x, t)$  obtained after transforming the solutions given in Eqs. (3.31) for the Euler equation of the point particles.
- c. At later times, each component of the gas gets reflected from the walls of the box which are described, in the point particle picture, by various terms in the series in Eq. (3.27) and Eq. (3.29).
- d. At the longest times both density profiles  $g(x, t)$  and  $\rho_b(x, t)$  stop broadening further and settle to piece-wise flat profiles which move between the walls with some constant effective velocity  $v_{\text{eff}}$  (see Fig. 3.2). The details of this solution will be discussed below. Since the density profile does not become time stationary even at the largest times, this indicates that for initial condition A, the hard rod system will never reach a GGE state ( which should be time stationary).

While we see a very good overall agreement between Euler solution and MD simulations, there are clear differences. If we zoom near the shocks in Figs. 3.1a and 3.1b, we notice that the simulation data for the hard rod density profile  $g(x, t)$  (dashed lines) shows a slight discrepancy with the Euler prediction. One observes similar discrepancy for  $\rho_b(x, t)$  also. The simulated profiles display spreading at the locations of the shock in the Euler solutions. This is demonstrated in Figs. (3.3(a), 3.4), where the density profiles are zoomed near the shock location after shifting appropriately so that the shock positions coincide. This spreading is a signature of the dissipation characterised by the Navier-Stokes term in Eq. (3.5). We observe that the width of the shock increases with time and scales as  $\sqrt{t}$  as can be seen from Fig. 3.3(a) where profiles for different times collapse under the scaling of  $x$  by  $\sqrt{t}$ . Microscopically the spreading originates from the fluctuations in the number of the background rods (having Maxwell velocity distribution) that a shock, of the Euler solution for  $g(x, t)$ , encounters till time  $t$ . This fluctuations arise from the fluctuations in the initial conditions. For a given initial configuration of the positions and velocities of the rods, the shock remains sharp and does not widen.

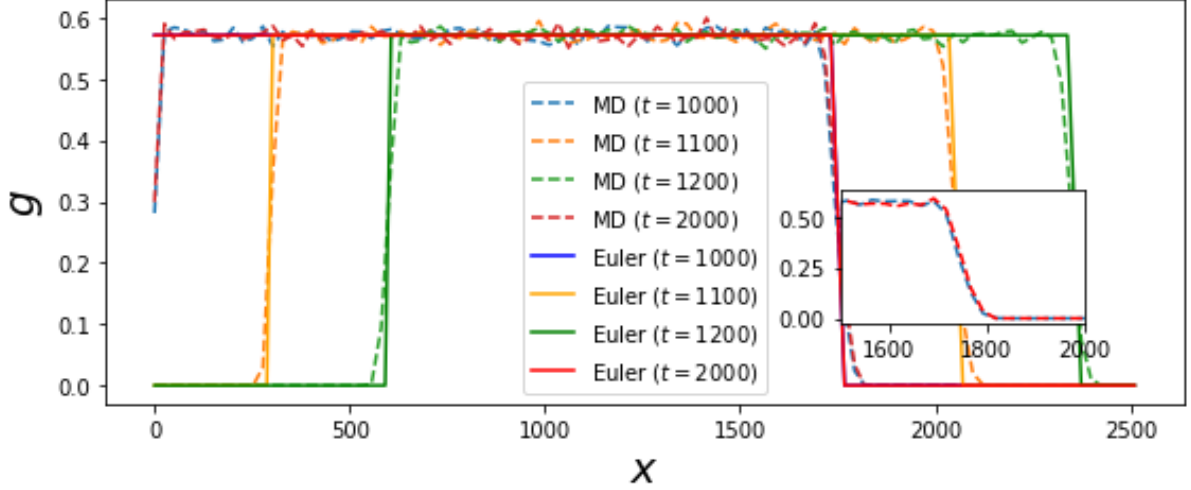


Figure 3.2: **Lack of thermalization to GGE:** Plot of  $g(x, t)$  vs.  $x$  at different (late) times. The dashed lines are obtained from molecular dynamics and the solid lines represents the solutions of the Euler equations. We observe that the profiles at  $t = 1000$ ,  $1100$  and  $t = 1200$  have moved by a displacement  $\Delta x \approx 300$ , implying  $v_{\text{eff}} \approx 3$ , in agreement with Eq. (3.38). The width of the pulse at the times  $t = 1000, 2000$  are the same, thus indicating that it saturates and the whole profile does not become uniform, i.e., it does not relax to a GGE form. The inset shows a zoom of the shock at the two times  $t = 1000$  and  $t = 2000$ , where we see that its width has saturated. We chose  $t = 1000$  and  $t = 2000$  as times for which the profiles coincided for the particular parameter values (i.e.,  $a, N, L$ ). Here  $N = 2000$ ,  $L = 2500$ ,  $a = 1$  and ensemble averaging over 100 realizations were performed while doing MD. The values of  $g_1, \rho_b, \bar{\rho}_b$  and  $v_{\text{eff}}$  agree with the predictions in Sec. 3.4).

However, the place at which the shock appears at a given time fluctuates from one initial microstate to another (see Fig. 3.3(b)). This happens because the number of background rods that the special rods encounters is different for different initial microscopic configurations. Hence, on an average the shock widens. At small times, these fluctuations are independent as the rods have not realised the presence of boundaries of the box. The  $\sqrt{t}$  growth at small times can be explained by considering the evolution of the density profile starting from initial condition A on an infinite line which is done in Appendix A.

The early time growth of the width of the shock stops after some time and saturates to a  $O(\sqrt{N})$  value as demonstrated in Fig. 3.4. As time progresses the rods move back and forth inside the box and consequently, the fluctuations in the number of background rods inside the region of the special rods (having velocity  $v_0$ ) do not remain independent and get correlated. Consequently, the spreading of the shock cannot continue to grow as  $\sqrt{t}$  and saturates to the observed  $O(\sqrt{N})$  value. Thus even in the thermodynamic limit the pulse  $g(x, t)$  does not spread to the full extent of the system and remains in the shape of a rectangular pulse that keeps on moving back and forth inside the box. Consequently, the total density profile of the rods does not become homogeneous and

stationary as one would expect in a GGE state. This implies that the a hard rod system inside a box, starting from initial condition A, does not reach the GGE state even in the thermodynamic limit.

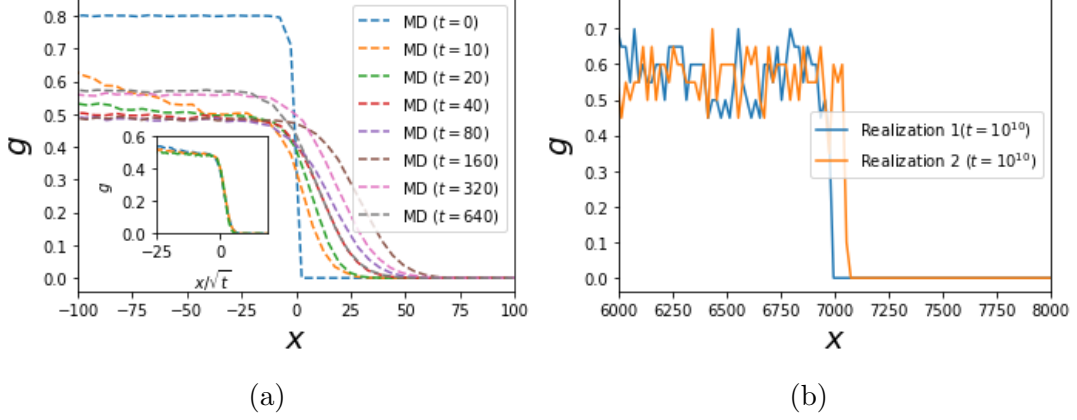


Figure 3.3: **(a) Time dependence of the width and (b) the fluctuation in the location of the shock:** (a) This shows the structure of the shock for the initial condition A at different times for a given system size ( $N = 2000$ ,  $L = 2500$ ). The curves have been shifted so that the shock fronts for all the curves coincide. While doing MD, ensemble averaging over 5000 initial microstates were performed. We see that there is trend of increasing width with time while in the inset (which shows curves for  $t = 20, 40, 80$ ), we see that there is a scaling collapse in the variable  $x/\sqrt{t}$  for short times when the  $v = 1$  pulse does not know about the boundaries of the system and hence behaves like it is in an infinite system. We explain this  $\sqrt{t}$  dependence in Appendix A. (b) This shows plot of  $g(x, t)$  for two different realizations (microstates) for initial condition A. We see that in a single realization the shock remains sharp, while the positions of the shock front in two realizations are different. Consequently, ensemble averaging will lead to smearing of the shock and thus is necessary to observe dissipation. Here we have chosen  $N = 8000$ ,  $L = 10000$ .

**Euler solution in  $t \rightarrow \infty$  limit:** We now find the solution of the Euler equation in the  $t \rightarrow \infty$  limit. Recall that in the initial condition A, the rods are uniformly distributed in each half with density  $\rho_0$ . The rods on the left half have velocity  $v = 1$  and those on the right half have velocities distributed according to Eq. (3.3). Using Eq. 3.16, one maps this hard rod system to a point particle gas with uniform density  $\rho^0(x, 0) = \frac{\rho_0}{1 - a\rho_0}$  inside a smaller box of size  $L' = L - Na$ . The velocity distribution remains unchanged as in the hard-rod gas, *i.e.*,  $\delta(v - 1)$  in the left half and  $h(v)$  in the right half. In the point particle gas the component with velocity  $v = 1$  moves without changing its shape whereas the particles on the right half (called the background particles) perform free expansion, ignorant of the  $v = 1$  particles since the gas is non-interacting. At long times, the background point particles will expand into the full box of length  $L'$  and become uniform with density half of their initial density, *i.e.*,  $\rho^0(x, t \rightarrow \infty) = \frac{\rho^0(x, 0)}{2} = \frac{\rho_0}{2(1 - a\rho_0)}$ . Thus at

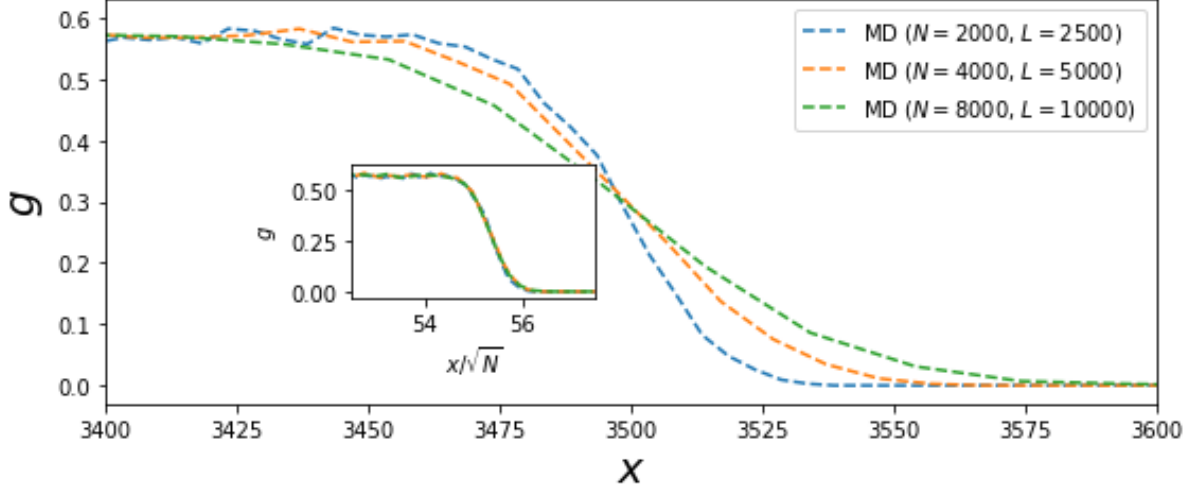


Figure 3.4: **System size dependence of the shock width for initial condition A:** This shows the structure of the shock at late times (when the width saturates) for the initial condition A for different system sizes. For all the curves we have chosen  $t = 10000$  which is much longer than the time at which the width of the pulse  $g(x, t)$  and that of the shock saturates. Even after this long time, the curve  $g(x, t)$  does not become uniform, i.e., it does not relaxes to GGE. The curve has been shifted so that the shock fronts for all the three curves coincide. We see that the shock broadens with system size, while in the inset, we see that there is a scaling collapse in the variable  $x/\sqrt{N}$ , thus showing that the shock broadens with the system size as  $\sqrt{N}$ . In this case ensemble averaging over 500 realizations was performed.

long times, one would observe the initial density pulse of the special point particles with velocity  $v = 1$  moving in the uniform background of thermal particles (with Maxwell velocity distribution). Hence, at any instant, the total density profile has two regions: a uniform high density region where the  $v = 1$  pulse is present (we call it the pulse region) and a uniform low density region in the remaining part of the box. Thus, the total density profile in the long time limit becomes piece-wise uniform which we now proceed to compute.

Let us denote the value of the density of the  $v = 1$  particles inside the pulse by  $g'_1$ , in the point particle picture, and by  $g_1$  in the hard rod picture. Similarly, we denote the density of the background particles inside the pulse region by  $\rho'_b$  and  $\rho_b$ , respectively, in the point particle and hard rod pictures. We also denote the density of background particles outside the pulse region by  $\bar{\rho}'_b$  and  $\bar{\rho}_b$ , once again, in the point particle and hard rod pictures, respectively. The total density of point particles in the pulse region is  $g'_1 + \rho'_b$  where  $g'_1 = \frac{\rho_0}{1-a\rho_0}$  and  $\rho'_b = \frac{\rho_0}{2(1-a\rho_0)}$ . Hence the total density there is  $\frac{3\rho_0}{2(1-a\rho_0)}$ . The density outside the pulse region is given by  $\bar{\rho}'_b = \frac{\rho_0}{2(1-a\rho_0)}$ . Now using the inverse mapping in Eq. (3.16) along with Eq. (3.18), one gets the late time densities in the hard rod picture.



The density outside the pulse region is given by

$$\bar{\rho}_b = \frac{\rho_0}{2 - a\rho_0}, \quad (3.32)$$

and the total density inside the pulse region is given by

$$g_1 + \rho_b = \frac{3\rho_0}{2 + a\rho_0}. \quad (3.33)$$

To find individual values of  $g_1$  and  $\rho_b$  we use the conservation of the number of background particles

$$\rho_b \times L_1 + \bar{\rho}_b \times (L - L_1) = \frac{N}{2}, \quad (3.34)$$

where  $L_1$  is the length of the pulse region at late times and  $L - L_1$  is the length of the region outside the pulse. It is easy to see that  $L_1 = \frac{N}{2g_1}$ . Dividing both sides of Eq. (3.34) by  $N$ , we get

$$\frac{\rho_b}{2g_1} + \bar{\rho}_b \left( \frac{1}{\rho_0} - \frac{1}{2g_1} \right) = \frac{1}{2}. \quad (3.35)$$

Solving Eq. (3.33) and Eq. (3.35), we finally get

$$g_1 = \frac{2\rho_0}{2 + a\rho_0}, \quad (3.36)$$

$$\rho_b = \frac{\rho_0}{2 + a\rho_0}. \quad (3.37)$$

The effective velocity with which the quasiparticles with  $v = 1$  move at late times can be computed easily. The total density at late times in the pulse region is  $\rho = g_1 + \rho_b = \frac{3\rho_0}{2 + a\rho_0}$ . The velocity field  $u$  in the pulse region at late times is given by  $u = \frac{g_1}{g_1 + \rho_b} = \frac{2}{3}$ . The effective velocity is thus:

$$v_{\text{eff}} = \frac{v_0 - a\rho u}{1 - a\rho} = \frac{2 - a\rho_0}{2 - 2a\rho_0}. \quad (3.38)$$

In our MD simulations in Figs. (3.1, 3.2), we have taken  $\rho_0 = 4/5$ ,  $a = 1$ . Plugging these values into the expressions above, we get  $\bar{\rho}_b = \frac{2}{3}$ ,  $\rho_b = \frac{2}{7}$ ,  $g_1 = \frac{4}{7}$  and  $v_{\text{eff}} = 3$ . We have verified that these values match with our MD results at long times in Fig. 3.2. Note that  $v_{\text{eff}}$  is the late-time speed of quasiparticles with bare velocity  $v = 1$ .

### 3.4.2 Initial condition B

In this case there is a special rod at the origin (middle of the box) with a fixed velocity  $v_0 = 1$  and the two halves of the box on either side of the special particle are initially filled uniformly by hard rods. The velocities of all rods, except the special one, are

distributed according to the Maxwell distribution  $h(v)$  given in Eq. (3.3). This initial condition was studied by Lebowitz, Percus and Sykes (LPS) in [64]. The initial single particle phase space density is  $f(x, v, t = 0) = \delta(v - v_0)\delta(x) + \rho_0 h(v)$ . Since the initial distribution of the background rods are already in equilibrium, it does not change with time. However, the phase space distribution of the special rod (of velocity  $v_0 = 1$ ) will change with time. At the Euler level the special rod moves ballistically with an effective velocity  $v_{\text{eff}} = \frac{v_0}{1 - a\rho_0}$ . Hence the Euler solution (for an infinite box) is given by  $f(x, v = v_0, t) = \delta(v - v_0)\delta(x - v_{\text{eff}}t)$ . However, by obtaining the exact microscopic solution of the problem in the thermodynamic limit and by performing an ensemble average, LPS showed that  $f(x, v_0, t)$  spreads diffusively, along with a drift with velocity  $v_{\text{eff}}$  [64], i.e, at long times one has the form  $f(x, v_0, t) = \delta(v - v_0)\delta\rho(x, t)$ . They also obtained an explicit expression of the diffusion constant. The results of LPS were used in [66] to compute the current-current correlation and thus the Navier-Stokes (NS) term using the Green-Kubo formula. In Fig. 3.5a we present simulation results for  $\delta\rho(x, t)$  which displays the spreading predicted by LPS. We observe that the spreading of the distribution increases with  $t$  and the data for different time collapse into a single function under scaling of space by  $\sqrt{t}$ , as shown in Fig. 3.5b. This implies that the spreading grows with time as  $\sqrt{t}$  [at late times it saturates in a finite box, due to the same reason for saturation in case (A)].

The origin of the growth of the width of the distribution at early times can be understood heuristically from a microscopic computation of the fluctuations of particle number as follows. Let  $\mathcal{N}_t$  be the number of particles in the interval  $[0, x_t]$ , where  $x_t$  is the position of the quasiparticle (special rod) with  $v = v_0 = 1$  at time  $t$ . In the corresponding point particle picture the special particle, with velocity  $v = v_0 = 1$ , would move by a distance  $v_0 t$  in time  $t$ . Hence, the position of the rod with velocity  $v = v_0 = 1$  is

$$x_t = v_0 t + a\mathcal{N}_t. \quad (3.39)$$

where  $\mathcal{N}_t$ , in the point particle picture, is the number of point particles that the special particle has crossed during its evolution, starting from the origin to the position  $v_0 t$  at time  $t$ . The number  $\mathcal{N}_t$  fluctuates from one realisation to another in an ensemble of initial conditions, and the fluctuation is proportional to  $\sqrt{\langle \mathcal{N}_t \rangle}$ . The spread in  $f(x, v_0, t)$  will also be proportional to the fluctuations, i.e., to  $\sqrt{\langle \mathcal{N}_t \rangle}$ . On an infinite line with uniform background of thermal particles,  $\langle \mathcal{N}_t \rangle$  grows linearly as  $t$  which thus leads to the  $\sqrt{t}$  growth of the width in the distribution function. In a finite box,  $\langle \mathcal{N}_t \rangle$  cannot grow without bound, because the number of particles in the box is finite. On the hydrodynamic scale, the  $\sqrt{t}$  spreading arises due to the Navier-Stokes terms in Eq. (3.5b) and we will now demonstrate this by obtaining a analytic solution of the Navier-Stokes equation (3.5b)

on the infinite line. For this we make the ansatz:

$$f(x, v, t) = \delta(v - v_0)\delta\rho(x, t) + \rho_0 h(v), \quad (3.40)$$

where  $h(v)$  is given in Eq. (3.3). This ansatz is motivated by the fact that the number of particles with a given velocity is conserved, and that the distribution of the background rods does not change with time. Plugging the ansatz into the Navier-Stokes equation, we get the following drift-diffusion equation for  $\delta\rho(x, t)$  after ignoring the non linear terms proportional to  $(\delta\rho)^2$ :

$$\partial_t(\delta\rho) + v_{\text{eff}}\partial_x(\delta\rho) = \frac{n\mu(v_0)a^2}{2}\partial_x^2(\delta\rho), \quad (3.41)$$

where  $v_{\text{eff}} = \frac{v_0}{1-a\rho_0}$ ,  $n = \frac{\rho_0}{1-a\rho_0}$ ,  $\mu(v_0) = \int dv |v - v_0| h(v)$ . The solution of this for the LPS-like initial condition is given by:

$$\delta\rho(x, t) = \frac{1}{\sqrt{2\pi na^2\mu(v_0)t}} e^{-\frac{(x-v_{\text{eff}}t)^2}{2a^2n\mu(v_0)t}}, \quad (3.42)$$

which is exactly the solution that was obtained by LPS from a completely microscopic analysis [64]. In Fig. 3.5b, we verify that the expression in Eq. (3.42) agrees with the MD simulation results. Our numerical results thus provide a direct demonstration of an observable effect of the NS terms in the hydrodynamic equations.

### Why diffusion is not anomalous?

It was shown in [75], using fluctuating hydrodynamics and renormalization group (RG) arguments, that in conventional one-dimensional momentum conserving system, diffusion is anomalous. However, for the one-dimensional system of hard rods (which is also a momentum conserving system), we have found normal diffusion. The reason for this is that for conventional fluids considered in [75], there is no well defined quasiparticle description and thus the noise  $\eta(x, t)$  is uncorrelated in space:

$$\langle \eta(x, t)\eta(x', t') \rangle \propto \delta(x - x')\delta(t - t'), \quad (3.43)$$

which forces the non-linear advective term to become relevant under the RG flow and thus give rise to anomalous diffusion. However, for the one-dimensional system of hard rods, the noise term is correlated in space because of the existence of well defined quasiparticles with no  $x - x'$  dependence in the form of the two-point correlation [67]:

$$\langle \eta(x, t)\eta(x', t') \rangle \propto \delta(t - t'). \quad (3.44)$$

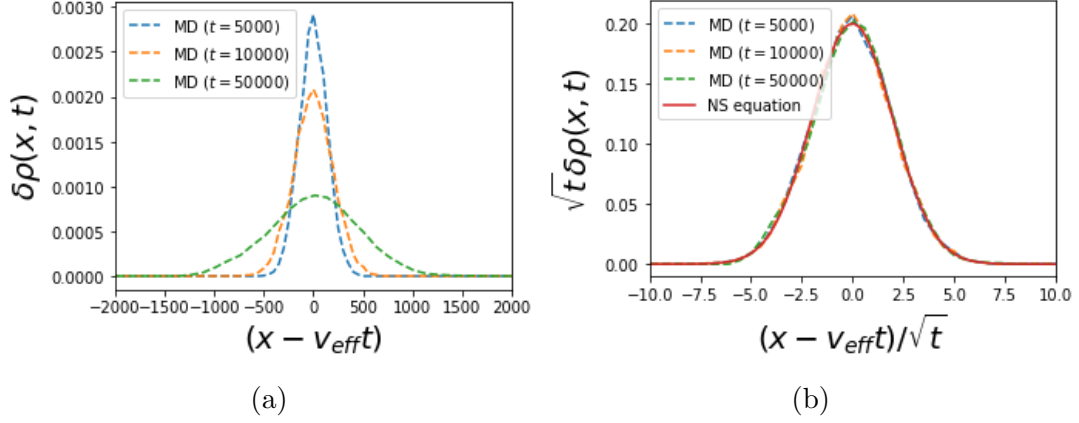


Figure 3.5: **Verifying NS equation for LPS-like initial condition:** (a) This figure compares the results from MD simulation for the evolution of the density profile with those obtained from the solution of the NS equation, for the LPS-like initial condition. (b) We show the plot in terms of the scaling variables. We see that there is a good scaling collapse, and a nice agreement with the solution of NS equation. We have taken,  $N = 2 \times 10^6$ ,  $L = 2.5 \times 10^6$ ,  $a = 1.0$ ,  $v_0 = 1.0$  (and so  $\mu(v_0) \approx 1.0$ ). For MD, ensemble averaging has been done over 10000 realizations. The times considered are much before the pulse hits the boundary of the box, hence the system is effectively infinite.

Thus the non-linear term does not become relevant in this case and the diffusion is normal.

### 3.4.3 Euler vs MD for initial condition C

Finally we consider the free expansion set up in which the  $N$  hard rods are initially confined to the left half of the box of size  $L$  and distributed uniformly in space with density  $\rho_0 = N/L$ . The velocities of the rods are drawn from the Maxwell distribution  $h(v)$  in Eq. (3.3). As in the previous cases, we have hard reflecting walls at  $x = 0$  and  $x = L$ . We now follow the same approach outlined in Sec. (3.4), to obtain a solution of the Euler equation for this initial condition, via the mapping to hard point gas. The solution in the point particle picture is similar to that obtained in [30], with the density given by:

$$\rho^0(x', t) = \frac{\rho_0}{1 - a\rho_0} + \frac{4\rho_0}{1 - 2a\rho_0} \sum_{k=1}^{\infty} \frac{1}{\pi k} \cos\left(\frac{k\pi x'}{L - Na}\right) \sin\left(\frac{\pi k(L - 2Na)}{2(L - Na)}\right) \exp\left\{\left(\frac{-\pi^2 k^2 T t^2}{2(L - Na)^2}\right)\right\}, \quad (3.45)$$

where  $\rho_0 = N/L$  and  $T = 1$ . In the  $a \rightarrow 0$  limit, the above expression of the density profile  $\rho^0(x, t)$  matches with those obtained in [30]. Using the inverse mapping in Eq. (3.16), the density profile  $\rho(x, t)$  of the rods can be found, where recall  $x = x' + aF^0(x', t)$  and the cumulative density profile,  $F^0(x', t)$ , can be computed from  $\rho^0(x', t)$ . In Fig. 3.6(a), we

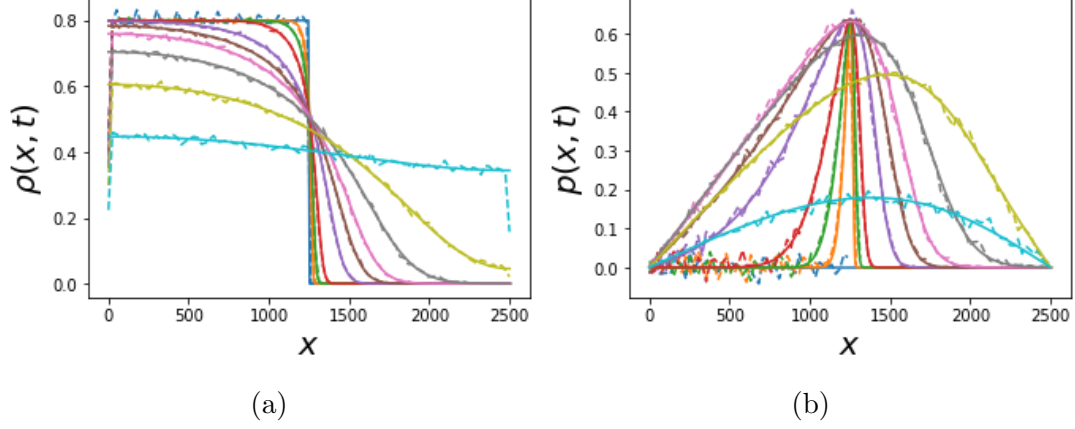


Figure 3.6: **Comparing solution of Euler equation with MD simulation for initial condition C:** Plots of the density and momentum profiles and comparison of the exact solution of Euler equation (solid lines) and the profiles obtained from MD (dashed lines) for the free expansion problem. We have shown for times  $t = 0$  (dark blue),  $t = 10$  (orange),  $t = 20$  (green),  $t = 40$  (red),  $t = 100$  (violet),  $t = 150$  (brown), 200 (pink),  $t = 300$  (grey),  $t = 500$  (muddy) and  $t = 1000$  (light blue). We have taken  $N = 1000$ ,  $L = 2500$  and averaged over 100 realizations.

compare the theoretically computed profiles of the rods at different times with the density profiles obtained from MD simulation, and we observe excellent agreement. From this plot, we observe that with increasing time the density profile of the rods spreads to the right half of the box in a monotonic fashion and finally approaches a time-independent spatially uniform profile which is consistent with a GGE state.

In a similar way, the exact Euler expression for the momentum density field  $p(x, t)$  can be obtained. First we compute the momentum field  $p^0(x', t)$  in the point particle picture and then transform to the momentum field for the hard rods using

$$p(x, t) = \frac{p^0(x', t)}{1 + a\rho^0(x', t)}. \quad (3.46)$$

We find

$$p^0(x', t) = \frac{4tT\rho_0}{(1 - a\rho_0)(1 - 2a\rho_0)} \frac{1}{L} \sum_{k=1}^{\infty} \exp\left\{-\frac{k^2\pi^2Tt^2}{2L^2(1 - a\rho_0)^2}\right\} \sin\left(\frac{k\pi(1 - 2a\rho_0)}{2(1 - a\rho_0)}\right) \sin\left(\frac{k\pi x'}{L(1 - a\rho_0)}\right), \quad (3.47)$$

where  $T = 1$ . In Fig. 3.6(b) we compare this with the results obtained from the MD simulations and we again see very good agreement. Here We observe that initially the momentum profile was zero everywhere. Once the gas is released, the rods with positive velocities near the middle of the box start moving to the right half. Thus the gas creates a positive momentum profile near the centre of the box. As time progresses, more particles move to the right half and consequently the momentum profile spreads on both halves of

the box. After some time, of the order  $L/\sqrt{T}$ , finite size effects start showing, and some rods get reflected from the right walls. As a result, the motion of these rods start reducing the momentum field. At very late times, each rod has undergone several collisions with both the walls and the gas equilibrates. The time scale of equilibration is also of the order  $L/\sqrt{T}$ . At this stage, one has rods of opposite velocities with equal probabilities at any point of the box which leads again to a zero momentum profile everywhere.

Note that shifting the origin to  $L/2 - Na$  (i.e.,  $x' \rightarrow z' = x' - L/2 + Na$ ) in the point particle problem, and taking  $L, N \rightarrow \infty$  with  $N/L = \rho_0$ , one obtains the solution of Euler GHD on the infinite line for times  $t \ll \frac{L}{\sqrt{T}}$  as:

$$\begin{aligned}\rho^0(z', t) &= \frac{2\rho_0}{2(1 - 2a\rho_0)} \operatorname{erfc}\left(\frac{z'}{\sqrt{2T}t}\right), \\ p^0(z', t) &= \frac{2\rho_0\sqrt{T}}{(1 - 2a\rho_0)\sqrt{2\pi}} \exp\left(-\frac{z'^2}{2t^2T}\right),\end{aligned}\tag{3.48}$$

where  $T = 1$  and  $\frac{2\rho_0}{1-2a\rho_0}$  is the initial density for  $z' \in (-\infty, 0)$ . The early time plots (for  $t < 300$ ) in Fig. (3.6) can be obtained by transforming the above simpler functions to  $\rho(x, t)$  and  $p(x, t)$  using transformations in Eq. (3.16), (3.46) and Eq. (3.18). The distortions of the densities of the point particles are appearing due to the non-linear transformations.

**Domain line for initial condition C:** For the point particle case,  $f^0(x', v, t)$  has a discontinuity in  $x$  space (for a given  $v$ ) for the free expansion problem. Since there is a mapping between the point particle Euler equation and the hard rod Euler equation, we expect that the Euler equation for hard rods will admit a similar discontinuity. We call the line of discontinuity of  $f(x, v, t)$  in the single-particle phase space as the "domain line". For the free expansion problem, the domain line can be found implicitly in the following manner. For times before the particles hit the right end of the container, the domain line for the point particle problem is given by  $x' = vt + \frac{L}{2} - Na$ . For general times (including times after the particles hit the right end of the container), we can do an analysis similar to [30] to show that the single particle phase space distribution for the point particle problem for general times is given by:

$$\begin{aligned}f^0(x', v, t) &= \frac{2\rho_0}{1 - 2a\rho_0} \frac{e^{-v^2/2T}}{\sqrt{2\pi T}} \sum_{n=-\infty}^{\infty} \left[ \Theta\left(x' - vt - 2n(L - Na) + \frac{L}{2} - Na\right) \right. \\ &\quad \left. - \Theta\left(x' - vt + 2n(L - Na) - \frac{L}{2} + Na\right) \right].\end{aligned}\tag{3.49}$$

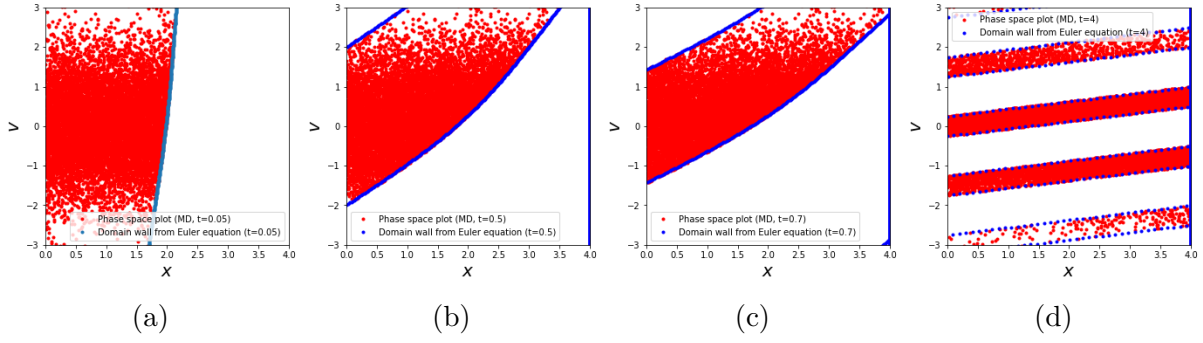


Figure 3.7: **Evolution of the domain lines for initial condition C:** Plot of the phase space distribution of the rods (red dots) for the free expansion problem at times (a)  $t = 0.05$  (b)  $t = 0.5$ , (c)  $t = 0.7$  and (d)  $t = 4$ . Solid blue lines represent the domain lines obtained from the exact solution of the Euler equation. We see that the blue lines lie at the edges of the red region and are curved in contrast to the straight lines for the point particle [see [30]]. At late times, the distribution wraps around the allowed region multiple times and thus creates fine structures. Here,  $N = 10000$ ,  $L = 4$ ,  $a = 0.0001$

where  $n$  is an integer. From this, the domain line for the point particle problem can be computed as zeros of the argument of the theta functions appearing in the equation above. We know how  $x'$  maps to  $x$  ( $x = x' + aF^0(x', t)$ ) within the framework of the Euler equation. Thus we can compute the domain line for the hard rod problem as predicted by the Euler equation. We computed the domain line for the hard rod problem as predicted by the Euler equation, and plotted it (blue line) along with the phase space plot for the hard rods (red dots) predicted by the MD simulation. The plots are shown in Fig. 3.7. We see that the blue line lies at the edge of the region occupied by the red dots. Thus the domain line predicted by Euler equation agrees with that predicted by MD simulation. We observe some key differences between hard rods (interacting integrable), alternate mass point-particle gas (non-integrable) and equal mass point particle gas (non-interacting integrable). In the hard-rod gas, we see a sharp domain line which is not a straight line at early times (Fig. 3.7). In equal mass point particle gas discussed in [30], a sharp and straight domain line was observed. However, in the alternate mass point particle gas, no sharp domain line was observed [73].

### 3.5 Conclusion

In this chapter, we studied the macroscopic evolution of a collection of hard-rods in one dimension starting from three different initial conditions: (A) A uniformly filled box with an inhomogeneous velocity distribution — half of the box is in thermal equilibrium and the other half has particles with a fixed velocity  $v = 1$ , (B) One special particle with fixed velocity  $v_0$  at the origin in the presence of a spatially uniform background of other



particles having thermal velocity distribution and (C) Free expansion from half of the box filled uniformly with thermal velocity distribution. For initial conditions (A) and (C) we find that the molecular dynamics results agree very well with the solutions of the Euler equations. However, for (A) we observe shocks at all times and find discrepancies from the Euler solutions at the location of the shocks which can be attributed to the Navier-Stokes corrections to the Euler equations. For initial condition (B), the effect of the Navier-Stokes terms is more dramatic and here we show that the effect can be understood from the analytic solution of the Navier-Stokes equation.

Our second important finding is the absence of GGE for initial conditions (A) and (B), whereas for initial condition (C) the system at late time approaches to a GGE state. The absence of GGE in the initial conditions (A) and (B) are manifested by the fact the density profile remains time dependent at all times.

We find that the effect of the Navier-Stokes terms is very weak and to observe its effect one requires to have singular velocity distributions in the initial conditions such that a shock in the density profile survives for macroscopic time scale. At the location of the shock the large density gradient makes the contribution from the Navier-Stokes terms significant and consequently the solution near the shock (in Euler solution) becomes different from the Euler solutions. This is also what is observed in non-integrable systems [76, 77, 78].

Since the effect of dissipation is most noticeable near a shock, it is worth asking the question that for which initial conditions are shocks formed. It is easy to see there will be a shock only if the mapped point particle problem has a shock. This can be seen in the following way. Let  $\delta x_0$  be the length scale over which the density is varying in the point particle problem. Then, using Percus' microscopic mapping,  $\delta x = \delta x_0 + a\delta N$ , where  $\delta x$  is the corresponding length scale in the hard rod problem, and  $\delta N$  is the number of point particles in the length scale  $\delta x_0$ . If the point particle problem has a shock, then  $\delta x_0$  will be small and  $\delta N \sim O(1)$ . Thus  $\delta x$  will be of the order of few rod lengths, and there will be a shock in the hard rod problem also. If there is no shock in the point particle problem, then both  $\delta x_0$  and  $\delta N$  will be large, and hence  $\delta x$  will also be large. Thus there will not then be any shock in the hard rod problem. We find that shocks in density profile of the point particles (and hence of the hard rods) persists with time if they start with singular velocity distributions [such as initial conditions (A) and (B)]. On the other hand if the rods have smooth velocity distribution to start with, then even if there are discontinuities in the density profile initially, the profiles at later times becomes smooth [such as initial condition (C)].

For initial condition A, one may be curious what will happen if one chooses a Maxwellian



distribution centered at  $v = 1$  instead of a  $\delta$ -function distribution  $[h(v) = \delta(v - 1)]$  that we have chosen for the left half of the particles. If one does that, then the corresponding point particle problem will not have any shocks as both the halves will perform free expansion independently and we do not observe shocks in free expansion. If the spread of the Maxwellian is small enough, then one may observe a weak shock at small times, however the shock will weaken with time and eventually give rise to a smooth density profile. The time scale over which the shock will weaken will be inversely proportional to the spread of the Maxwellian, hence the shock for our initial condition A is infinitely long lived on the Euler level.

Observing the effect of the Navier-Stokes terms through the evolution of the density profile is difficult. However, it should get strongly manifested in the evolution of Boltzmann's entropy [30, 73, 74], since the Euler solutions do not contribute to entropy production. It would be interesting to study the entropy production for these initial conditions. However, identifying the contribution of the Navier-Stokes terms in the entropy production is still difficult because it involves taking appropriate combination of the limits of the coarse graining scale and the thermodynamic limit. This remains an interesting and challenging open problem.

# Chapter 4

## Summary and outlook

In this thesis, we have aimed to bridge the gap between microscopic dynamics and hydrodynamics of classical many-particle systems by following two complementary pathways: first, by exploring non-integrable systems—using hard-rod and hard-disc gases as paradigms to study blast-wave propagation—and second, by examining interacting integrable systems where additional conservation laws and memory effects alter conventional thermalization. These studies address key questions regarding the validity of classical phenomenological theories such as thermodynamics, hydrodynamics and statistical mechanics, and expose the subtle role of dissipation.

In doing so, we have faced the foundational assumption in conventional hydrodynamics—that of scale separation, where microscopic details average out and decouple from macroscopic dynamics. However, many physical, biological, and socioeconomic systems exhibit strong coupling across multiple scales, forcing us to use alternative frameworks. In this chapter, we view our findings in the light of broader theoretical tools, namely the renormalization group (RG) and effective field theory (EFT), to discuss both the promise and the limitations of conventional theories when applied to strongly coupled systems.

### 4.1 Synthesis of Key Findings

#### 4.1.1 Insights from Non-integrable Systems

In the outer regions of a blast wave, our microscopic simulations and analytical treatments confirm that the classical TvNS solution remains robust. Dimensional analysis gives us

the following scaling forms for the density, velocity, and temperature fields:

$$\rho \sim \rho_\infty G(\xi), \quad v \sim \frac{r}{t} V(\xi), \quad T \sim \frac{r^2}{t^2} Z(\xi), \quad (4.1)$$

where the self-similar variable is defined as  $\xi = r/R(t)$  and the shock radius scales as

$$R(t) \sim t^{2/(d+2)}. \quad (4.2)$$

Near the blast core, however, the large gradients predicted by the Euler equations lead to divergent behavior (e.g.,  $Z(\xi) \sim \xi^{-4}$ ), and so the Euler equations in the core are not self-consistent as they have been derived under the assumption of small gradients. Here, dissipative effects become important. By introducing a new core length scale

$$X(t) \sim t^{2/5} \quad (\text{in 2D}), \quad (4.3)$$

we derive modified scaling relations:

$$\rho \sim t^{-1/5} \tilde{G}(\eta), \quad v \sim t^{-3/5} \tilde{V}(\eta), \quad T \sim t^{-4/5} \tilde{Z}(\eta), \quad (4.4)$$

with  $\eta = r/t^{2/5}$ . These inner solutions reconcile the discrepancy between scaling of molecular dynamics (MD) simulations and the predictions of inviscid theories in the core region.

Our MD and NS simulations show excellent agreement in the bulk region, while in the core region, the scaling exponent matches but there is a mismatch in the scaling functions as we do not know the exact values of the transport coefficients. The two different scaling regions are connected by the rules of asymptotic matching. These results show that classical hydrodynamics (via the Euler equations) applies when gradients are mild, and dissipation must be explicitly modeled in regions with strong spatial variations. Even though the shock front itself is a region of extremely strong gradients, the Euler equations do successfully describe the bulk flow on either side of this discontinuity through the Rankine-Hugoniot jump conditions. These conditions are derived from the conservative form of the Euler equations and dictate the magnitude of the jump (e.g., density compression ratio) without needing to know the internal structure of the shock.

### 4.1.2 Insights from Integrable Systems

For one-dimensional integrable systems (e.g., hard-rod gases), the derivation of hydrodynamic equations cannot rely on the molecular chaos assumptions because of their

integrable structure. Instead, a completely different method is needed to derive their hydrodynamics. For the hard-rod gas, the hydrodynamics can be derived rigorously from microscopic dynamics, owing to the simple nature of their dynamics. However, for other integrable systems with more complex interactions (such as the Toda model), some phenomenological assumptions must be incorporated to derive their hydrodynamics.

We found that some initial conditions in the hard-rod gas do not relax toward a GGE. This finding challenges the universality of conventional thermalization. An open question is whether a similar failure of thermalization also occurs in other integrable systems which have complicated dynamics, like the Toda model.

However, we found the predictions of hydrodynamics matches quite well with the microscopic simulations for the hard-rod gas.

## 4.2 Connecting Hydrodynamics with the Renormalization Group and Effective Field Theory

The renormalization group provides a systematic methodology for understanding how microscopic interactions give rise to macroscopic behavior by iteratively integrating out short-scale degrees of freedom. In classical RG treatments of critical phenomena, many microscopic details become irrelevant near a fixed point, leading to universal scaling laws.

In hydrodynamics, the underlying assumption is that scales are well separated: the fast (microscopic) scales can be averaged out, yielding effective equations (such as the Euler or NS equations) that govern the slow, large-scale behavior. However, in places such as fully developed turbulence or in the blast core, the spatial gradients become so large that microscopic (or dissipative) scales strongly couple with the macroscopic flow. This is similar, though not exactly identical, to critical phenomena, where fluctuations across many scales interact strongly. RG-based analyses in turbulence (e.g., Yakhot and Orszag [79]) show that such coupling leads to anomalous scaling corrections not captured by classical theories.

RG methods can be adapted to derive effective hydrodynamic equations that include the influence of small-scale fluctuations without assuming a strict decoupling. In this view, the “coarse-graining” process of RG is analogous to the averaging in effective field theory (EFT), where non-renormalizable terms (representing microscopic details) are suppressed but may still provide crucial corrections when scale separation is weak [80].

### 4.2.1 Effective Field Theory (EFT) and Multiscale Coupling

EFT provides a powerful framework for constructing models that are valid over a particular range of scales. By explicitly incorporating an energy (or length) cutoff, EFT captures the essential physics at a given scale while systematically accounting for corrections from higher-energy processes. In the context of hydrodynamics, conventional hydrodynamics can be seen as an EFT valid when the wavelength of perturbations is much larger than the mean free path. However, when this condition is violated—for example, in regions of strong gradients—the hydrodynamic description must be augmented by additional (often non-local) terms arising from integrating out short-scale fluctuations.

When multiple scales are strongly coupled (as in turbulence, neural dynamics, or financial markets), the standard EFT approach may fail. Here, modern multiscale methods such as universal differential equations (UDEs) provide alternative strategies that do not strictly assume scale separation and can dynamically learn the interplay between scales [81].

## 4.3 Limitations

Several limitations of the study in this thesis warrant discussion:

- **Approximation of Dissipative Processes:** Our treatment of dissipation in the blast core is based on first-order corrections. In systems with large gradients, non-local or higher-order dissipative effects may be significant. Incorporating these effects requires extending current RG and EFT methods.
- **Numerical Challenges:** The application of RG-inspired methods and multiscale numerical techniques is computationally intensive. Developing efficient algorithms that accurately integrate contributions from all scales remains an active area of research.
- **Other Integrable models:** The lack of thermalization to GGE in the hard-rod gas for certain initial conditions forces us to ask whether similar lack of thermalization is also present in other integrable systems which cannot be directly treated analytically using microscopic dynamics (such as the Toda model).

# Appendix A

## $\sqrt{t}$ Behaviour of the Shock for Initial Condition (A)

In this appendix, we explain the  $\sqrt{t}$  broadening of the shock found in Fig. 3.3(a) for short times for initial condition A. For sufficiently short times, the evolution of the density profile is effectively the same as in an infinite box. We thus consider a box  $\left[-\frac{L}{2}, \frac{L}{2}\right]$  with large  $L$  and  $N$  with  $\rho_0 = N/L$  fixed. The hard rods are arranged in initial condition A. This maps to a point particle problem in a box  $\left[-\frac{L}{2}, \frac{L}{2} - Na\right]$  with the left half having velocity  $v = 1$  and the right half having Maxwellian velocity distribution with unit temperature. Following the approach described in Sec. (3.4), it can be shown that for short times:

$$g'(x', t) = \frac{\rho_0}{1 - a\rho_0} \Theta\left(-x' - \frac{Na}{2} + v_0 t\right), \quad (\text{A.1})$$

$$\rho'_b(x', t) = \frac{\rho_0}{2(1 - a\rho_0)} \text{erfc}\left[\frac{-x' - \frac{Na}{2}}{t\sqrt{2}}\right]. \quad (\text{A.2})$$

where  $\rho_0 = N/L$  and  $v_0 = 1$ . Following the same argument as in the Sec. 3.4.2, the width of the shock  $\xi(t)$  is proportional to the fluctuation of number of background particles to the left of the shock. Thus:

$$\xi^2(t) \propto \lim_{N, L \rightarrow \infty} \frac{a\rho_0}{2(1 - a\rho_0)} \int_{-L/2}^{v_0 t - Na/2} \text{erfc}\left[\frac{-x' - \frac{Na}{2}}{t\sqrt{2}}\right] dx' \quad (\text{A.3})$$

$$= \lim_{N, L \rightarrow \infty} \frac{a\rho_0}{2(1 - a\rho_0)} \int_{-L/2 + Na/2}^{v_0 t} \text{erfc}\left[\frac{-u}{t\sqrt{2}}\right] du \quad (\text{A.4})$$

$$= \frac{a\rho_0}{2(1 - a\rho_0)} \int_{-\infty}^{v_0 t} \text{erfc}\left[\frac{-u}{t\sqrt{2}}\right] du \quad (\text{A.5})$$

$$= \frac{a\rho_0 t}{2(1 - a\rho_0)} \int_{-v_0}^{\infty} \text{erfc}\left[\frac{y}{\sqrt{2}}\right] dy. \quad (\text{A.6})$$

where in going from second last line to last line, we have made a change of variable  $y = -u/t$ . The integral term in the last line is just some constant number. Thus  $\xi(t) \propto \sqrt{t}$ .

# Bibliography

- [1] Sahil Kumar Singh, Subhadip Chakraborti, Abhishek Dhar, and P. L. Krapivsky. Blast waves in the zero temperature hard sphere gas: Double scaling structure. *Journal of Statistical Physics*, 190(7):118, Jul 2023.
- [2] Sahil Kumar Singh, Abhishek Dhar, Herbert Spohn, and Anupam Kundu. Thermalization and hydrodynamics in an interacting integrable system: The case of hard rods. *Journal of Statistical Physics*, 191(6):66, May 2024.
- [3] E. M. Lifshitz and L. P. Pitaevskii. *Physical Kinetics. Course of Theoretical Physics, Vol. 10*. Butterworth-Heinemann, 1981.
- [4] Benjamin Doyon. Lecture notes on Generalised Hydrodynamics. *SciPost Phys. Lect. Notes*, page 18, 2020.
- [5] M. Bernstein and J. K. Percus. Expansion into a vacuum: A one-dimensional model. *Phys. Rev. A*, 37:1642–1653, Mar 1988.
- [6] J. K. Percus. Exact solution of kinetics of a model classical fluid. *The Physics of Fluids*, 12(8):1560–1563, 1969.
- [7] R. L. Dobrushin C. Boldrighini and Yu. M. Sukhov . One-dimensional hard rod caricature of hydrodynamics. *Journal of Statistical Physics*, 1983(31):577–616, June 1983.
- [8] C. Boldrighini and Y.M. Suhov . One-dimensional hard-rod caricature of hydrodynamics: “navier–stokes correction” for local equilibrium initial states. *Communications in Mathematical Physics*, 1997(189):577–590, November 1997.
- [9] Olalla A. Castro-Alvaredo, Benjamin Doyon, and Takato Yoshimura. Emergent hydrodynamics in integrable quantum systems out of equilibrium. *Phys. Rev. X*, 6:041065, Dec 2016.
- [10] Benjamin Doyon. Generalized hydrodynamics of the classical toda system. *Journal of Mathematical Physics*, 60(7):073302, 2019.



- [11] Jeremiah P. Ostriker and Christopher F. McKee. Astrophysical blastwaves. *Rev. Mod. Phys.*, 60:1–68, Jan 1988.
- [12] Jeremy Goodman. Convective instability of hollow sedov-taylor blast waves. *Astrophys. J.*, 358:214, jul 1990.
- [13] A. Gal-Yam, D. B. Fox, P. A. Price, E. O. Ofek, M. R. Davis, D. C. Leonard, A. M. Soderberg, B. P. Schmidt, K. M. Lewis, B. A. Peterson, S. R. Kulkarni, E. Berger, S. B. Cenko, R. Sari, K. Sharon, D. Frail, D. S. Moon, P. J. Brown, A. Cucchiara, F. Harrison, T. Piran, S. E. Persson, P. J. McCarthy, B. E. Penprase, R. A. Chevalier, and A. I. MacFadyen. A novel explosive process is required for the  $\gamma$ -ray burst GRB 060614. *Nature*, 444(7122):1053–1055, 2006.
- [14] Xiaping Tang and Roger A. Chevalier. Shock evolution in non-radiative supernova remnants. *Monthly Notices of the Royal Astronomical Society*, 465(4):3793–3802, 11 2016.
- [15] Adam Burrows. Colloquium: Perspectives on core-collapse supernova theory. *Rev. Mod. Phys.*, 85:245–261, Feb 2013.
- [16] L. I. Sedov. *Similarity and dimensional methods in mechanics*. Academic Press, New York, 1959.
- [17] L. D. Landau and E. M. Lifshitz. *Fluid Mechanics*. Pergamon Press, New York, 1987.
- [18] G. I. Taylor. The formation of a blast wave by a very intense explosion I. Theoretical discussion. *Proc. R. Soc. A*, 201(1065):159–174, 1950.
- [19] Geoffrey Ingram Taylor. The formation of a blast wave by a very intense explosion.-ii. the atomic explosion of 1945. *Proceedings of the Royal Society of London. Series A. Mathematical and Physical Sciences*, 201(1065):175–186, 1950.
- [20] J. von Neumann. *Collected Works*. Pergamon Press,Oxford, 1963.
- [21] Leonid Ivanovich Sedov. Propagation of strong shock waves. *Journal of Applied Mathematics and Mechanics*, 10:241–250, January 1946.
- [22] H A Bethe, K Fuchs, J von Neuman, R Peierls, W G Penney, and notes written by J.O. Hirschfelder. Shock hydrodynamics and blast waves. 10 1944.
- [23] J. von Neumann. *Physics of shock waves and high-temperature hydrodynamic phenomena, Vol. 1-2*. Academic Press, New York, 1966-67.

- [24] A. F. Ghoniem, M. M. Kamel, S. A. Berger, and A. K. Oppenheim. Effects of internal heat transfer on the structure of self-similar blast waves. *Journal of Fluid Mechanics*, 117:473–491, 1982.
- [25] H. Steiner and W. Gretler. The propagation of spherical and cylindrical shock waves in real gases. *Physics of Fluids*, 6(6):2154–2164, 1994.
- [26] J. VonNeumann and R. D. Richtmyer. A method for the numerical calculation of hydrodynamic shocks. *Journal of Applied Physics*, 21(3):232–237, 1950.
- [27] Harold L. Brode. Numerical solutions of spherical blast waves. *Journal of Applied Physics*, 26(6):766–775, 1955.
- [28] Richard Latter. Similarity solution for a spherical shock wave. *Journal of Applied Physics*, 26(8):954–960, 1955.
- [29] Myron N. Plooster. Shock waves from line sources. numerical solutions and experimental measurements. *The Physics of Fluids*, 13(11):2665–2675, 1970.
- [30] Subhadip Chakraborti, Abhishek Dhar, Sheldon Goldstein, Anupam Kundu, and Joel L Lebowitz. Entropy growth during free expansion of an ideal gas. *Journal of Physics A: Mathematical and Theoretical*, 55(39):394002, sep 2022.
- [31] Santhosh Ganapa, Subhadip Chakraborti, P. L. Krapivsky, and Abhishek Dhar. Blast in the one-dimensional cold gas: Comparison of microscopic simulations with hydrodynamic predictions. *Physics of Fluids*, 33:087113, 2021.
- [32] Subhadip Chakraborti, Abhishek Dhar, and Paul Krapivsky. A splash in a one-dimensional cold gas. *SciPost Physics*, 13(3):074, 2022.
- [33] Stefano Lepri, Roberto Livi, and Antonio Politi. Thermal conduction in classical low-dimensional lattices. *Physics reports*, 377(1):1–80, 2003.
- [34] Abhishek Dhar. Heat transport in low-dimensional systems. *Advances in Physics*, 57(5):457–537, 2008.
- [35] Aritra Kundu, Cédric Bernardin, Keji Saito, Anupam Kundu, and Abhishek Dhar. Fractional equation description of an open anomalous heat conduction set-up. *Journal of Statistical Mechanics: Theory and Experiment*, 2019(1):013205, jan 2019.
- [36] Abhishek Dhar, Anupam Kundu, and Aritra Kundu. Anomalous heat transport in one dimensional systems: A description using non-local fractional-type diffusion equation. *Frontiers in Physics*, 7, 2019.

- [37] Pablo I. Hurtado. Breakdown of hydrodynamics in a simple one-dimensional fluid. *Phys. Rev. Lett.*, 96:010601, Jan 2006.
- [38] M. Barbier, D. Villamaina, and E. Trizac. Microscopic origin of self-similarity in granular blast waves. *Physics of Fluids*, 28:083302, 2016.
- [39] Jilmy P. Joy and R. Rajesh. Shock Propagation in the Hard Sphere Gas in Two Dimensions: Comparison Between Simulations and Hydrodynamics. *Journal of Statistical Physics*, 184(1):3, July 2021.
- [40] Jilmy P. Joy, Sudhir N. Pathak, and R. Rajesh. Shock Propagation Following an Intense Explosion: Comparison Between Hydrodynamics and Simulations. *Journal of Statistical Physics*, 182(2):34, February 2021.
- [41] A. Kumar and R. Rajesh. Blast waves in two and three dimensions: Euler versus navier–stokes equations. *Journal of Statistical Physics*, 188(2), jun 2022.
- [42] A. Kumar. Private communication.
- [43] J. R. Dorfman, Henk van Beijeren, and T. R. Kirkpatrick. *Contemporary Kinetic Theory of Matter*. Cambridge University Press, 2021.
- [44] Alain Barrat and Emmanuel Trizac. Molecular dynamics simulations of vibrated granular gases. *Phys. Rev. E*, 66:051303, Nov 2002.
- [45] R. W. MacCormack. A numerical method for solving the equations of compressible viscous flow. *AIAA Journal*, 20(9):1275–1281, 1982.
- [46] David M Gass. Enskog theory for a rigid disk fluid. *The Journal of Chemical Physics*, 54(5):1898–1902, 1971.
- [47] Ramón García-Rojo, Stefan Luding, and J Javier Brey. Transport coefficients for dense hard-disk systems. *Physical Review E*, 74(6):061305, 2006.
- [48] Gilberto M Kremer. *An introduction to the Boltzmann equation and transport processes in gases*. Springer Science & Business Media, 2010.
- [49] P. Resibois and M. De Leener. *Classical Kinetic Theory of Fluids*. Wiley, New York, 1977.
- [50] C. Cercignani. *The Boltzmann equation and its applications*. Springer, New York, 1988.
- [51] BJ Alder and TE Wainwright. Decay of the velocity autocorrelation function. *Physical review A*, 1(1):18, 1970.

- [52] Stefano Lepri. *Thermal transport in low dimensions: from statistical physics to nanoscale heat transfer*, volume 921. Springer, 2016.
- [53] Marcos Rigol, Vanja Dunjko, Vladimir Yurovsky, and Maxim Olshanii. Relaxation in a completely integrable many-body quantum system: An ab initio study of the dynamics of the highly excited states of 1d lattice hard-core bosons. *Phys. Rev. Lett.*, 98:050405, Feb 2007.
- [54] Balázs Pozsgay. The generalized gibbs ensemble for heisenberg spin chains. *Journal of Statistical Mechanics: Theory and Experiment*, 2013(07):P07003, jul 2013.
- [55] Tim Langen, Sebastian Erne, Remi Geiger, Bernhard Rauer, Thomas Schweigler, Maximilian Kuhnert, Wolfgang Rohringer, Igor E. Mazets, Thomas Gasenzer, and Jörg Schmiedmayer. Experimental observation of a generalized gibbs ensemble. *Science*, 348(6231):207–211, 2015.
- [56] Lev Vidmar and Marcos Rigol. Generalized gibbs ensemble in integrable lattice models. *Journal of Statistical Mechanics: Theory and Experiment*, 2016(6):064007, jun 2016.
- [57] Trevor Wenger Toshiya Kinoshita and David S. Weiss . A quantum newton’s cradle. *Nature*, 2006(440):900–903, April 2006.
- [58] Neel Malvania, Yicheng Zhang, Yuan Le, Jerome Dubail, Marcos Rigol, and David S. Weiss. Generalized hydrodynamics in strongly interacting 1d bose gases. *Science*, 373(6559):1129–1133, 2021.
- [59] Bruno Bertini, Mario Collura, Jacopo De Nardis, and Maurizio Fagotti. Transport in out-of-equilibrium  $xxz$  chains: Exact profiles of charges and currents. *Phys. Rev. Lett.*, 117:207201, Nov 2016.
- [60] Vincenzo Alba, Bruno Bertini, Maurizio Fagotti, Lorenzo Piroli, and Paola Ruggerio. Generalized-hydrodynamic approach to inhomogeneous quenches: correlations, entanglement and quantum effects. *Journal of Statistical Mechanics: Theory and Experiment*, 2021(11):114004, nov 2021.
- [61] Alvis Bastianello, Andrea De Luca, and Romain Vasseur. Hydrodynamics of weak integrability breaking. *Journal of Statistical Mechanics: Theory and Experiment*, 2021(11):114003, nov 2021.
- [62] Alvis Bastianello, Bruno Bertini, Benjamin Doyon, and Romain Vasseur. Introduction to the special issue on emergent hydrodynamics in integrable many-body systems. *Journal of Statistical Mechanics: Theory and Experiment*, 2022(1):014001, jan 2022.

- [63] Herbert Spohn. Interacting and noninteracting integrable systems. *Journal of Mathematical Physics*, 59(9), 06 2018. 091402.
- [64] J. L. Lebowitz, J. K. Percus, and J. Sykes. Time evolution of the total distribution function of a one-dimensional system of hard rods. *Phys. Rev.*, 171:224–235, Jul 1968.
- [65] Herbert Spohn. *Large Scale Dynamics of Interacting Particles*. Springer Berlin, Heidelberg, December 2012.
- [66] Benjamin Doyon and Herbert Spohn. Dynamics of hard rods with initial domain wall state. *Journal of Statistical Mechanics: Theory and Experiment*, 2017(7):073210, jul 2017.
- [67] Pablo A Ferrari and Stefano Olla. Macroscopic diffusive fluctuations for generalized hard rods dynamics. *arXiv preprint arXiv:2305.13037*, 2023.
- [68] Amy C. Cassidy, Charles W. Clark, and Marcos Rigol. Generalized thermalization in an integrable lattice system. *Phys. Rev. Lett.*, 106:140405, Apr 2011.
- [69] Pasquale Calabrese, Fabian H. L. Essler, and Maurizio Fagotti. Quantum quench in the transverse-field ising chain. *Phys. Rev. Lett.*, 106:227203, Jun 2011.
- [70] J. Eisert. Entangling power and quantum circuit complexity. *Phys. Rev. Lett.*, 127:020501, Jul 2021.
- [71] Jacopo De Nardis, Denis Bernard, and Benjamin Doyon. Hydrodynamic diffusion in integrable systems. *Physical review letters*, 121(16):160603, 2018.
- [72] D. W. Jepsen. Dynamics of a simple many-body system of hard rods. *Journal of Mathematical Physics*, 6(3):405–413, 1965.
- [73] Subhadip Chakraborti, Abhishek Dhar, and Anupam Kundu. Boltzmann’s Entropy During Free Expansion of an Interacting Gas. *Journal of Statistical Physics*, 190(74), 03 2023.
- [74] Saurav Pandey, Junaid Majeed Bhat, Abhishek Dhar, Sheldon Goldstein, David A. Huse, Manas Kulkarni, Anupam Kundu, and Joel L. Lebowitz. Boltzmann entropy of a freely expanding quantum ideal gas, 2023.
- [75] Onuttom Narayan and Sriram Ramaswamy. Anomalous heat conduction in one-dimensional momentum-conserving systems. *Phys. Rev. Lett.*, 89:200601, Oct 2002.
- [76] Jilmy P. Joy, Sudhir N. Pathak, and R. Rajesh. Shock propagation following an intense explosion: Comparison between hydrodynamics and simulations. *Journal of Statistical Physics*, 182, Feb 2021.

- [77] Subhadip Chakraborti, Santhosh Ganapa, P. L. Krapivsky, and Abhishek Dhar. Blast in a one-dimensional cold gas: From newtonian dynamics to hydrodynamics. *Phys. Rev. Lett.*, 126:244503, Jun 2021.
- [78] Sahil Kumar Singh, Subhadip Chakraborti, Abhishek Dhar, and P. L. Krapivsky. Blast waves in the zero temperature hard sphere gas: Double scaling structure. *Journal of Statistical Physics*, 190, Jul 2023.
- [79] Victor Yakhot and Steven A. Orszag. Renormalization-group analysis of turbulence. *Phys. Rev. Lett.*, 57:1722–1724, Oct 1986.
- [80] C. P. Burgess. *Introduction to Effective Field Theory*. Cambridge University Press, 2020.
- [81] Christopher Rackauckas, Yingbo Ma, Julius Martensen, Collin Warner, Kirill Zubov, Rohit Supekar, Dominic Skinner, Ali Ramadhan, and Alan Edelman. Universal differential equations for scientific machine learning, 2021.